Doctoral Dissertation
Doctoral Program in Aerospace Engineering (33th cycle)

Design and testing methodologies for UAVs under extreme environmental conditions

Matteo Scanavino

* * * * *

Supervisors
Prof. Giorgio Guglieri, Supervisor
Andrea Vilardi PhD, Co-supervisor

Doctoral Examination Committee:
Prof. G.Quaranta, Referee, Politecnico di Milano, Italy
Prof. A.Talamelli, Referee, Università di Bologna, Italy
Prof. P.Capone, Zurich University of Applied Science, Switzerland
Prof. L.Niccolai, Università di Pisa, Italy
Prof. M.Romano, Naval Postgraduate School, USA

Politecnico di Torino
2021

I hereby declare that, the contents and organisation of this dissertation constitute my own original work and does not compromise in any way the rights of third parties, including those relating to the security of personal data.

. . . .

Matteo Scanavino

Turin, 2021

Summary

Unmanned Aircraft Systems (UAS) are state of the art in aerospace industry for both commercial and military applications. In particular, small scale multicopters have gained momentum owing to their simple design, vertical take-off and landing as well as hover capabilities.

In the past years efforts were made to improve autopilot performance developing advanced Guidance, Navigation and Control (GNC) algorithms. Limited research studies focused on experimental characterization of small scale UAS and a way to assess and improve their design. However, the integration of unmanned aircraft with manned aviation within the context of Unmanned Aircraft System Traffic Management (UTM) requires a step forward to fully understand UAS potential even when unconventional weather conditions occur. Hence, detailed experimental data have a major role and provide an important basis to improve simulation tools required to predict vehicle performance. However, experimental testing has an important economical impact and requires a lot of time to collect high quality data. When extreme environmental conditions are considered, challenges on sensing device as a result of low temperatures and/or high altitudes arise; moreover, a systematic test approach is essential. The lack of experimental data as well as accurate prediction models to evaluate propeller coefficients over the UAS flight envelope are two major limitations in UAS science.

The aim of the following PhD thesis is the design and implementation of testing methodologies to assess performance of UAS. Among all type of unmanned systems, the attention is given to small scale multicopters and their propulsion systems. The PhD dissertation focuses on the experimental activity performed in terraXcube laboratory. Compared to other facility such as wind tunnels, this laboratory allowed to investigate desired atmospheric conditions combining different temperatures and altitudes (pressures).The main contribution of this thesis is related to the design of an experimental setup to collect thrust, torque, motor speed and electrical data of multicopters and propeller propulsion systems. Low temperature and high altitude effects were highlighted on performance: the corresponding air densities simulated inside the lab were exploited to characterize mechanical and electrical quantities with a systematic approach.

In the following PhD thesis attention was also given to simulation tools to predict propeller performance. Small scale thrust, torque and power data were simulated based on the Blade Element Momentum Theory combining both geometrical and aerodynamic

data for the propeller leveraged during the experimental tests. Results showed numerical and experimental data are overlapped when standard temperature and altitude conditions were considered. As soon as very low Reynolds numbers (below 100,000) were set, numerical prediction tools were not able to properly describe experimental data as a result of *laminar separation bubble* condition, responsible for performance degradation.

Experimental testing still remains a valuable instrument for the development of new UAS technologies, especially when unconventional flight conditions are considered. At the same time, improvements of simulation models are needed to describe unconventional flight conditions. These considerations lead to future works. Firstly, the investigation of other test cases such cold temperature effect on batteries and propeller performance sensitivity to icing conditions. Secondly, the definition of a mathematical model for Computational Fluid Dynamics (CFD) simulations able to predict non linearities arising from low Reynolds numbers.

The ultimate objective of this study is to support manufacturers, operators and regulatory authorities with a methodology to assess UAS capabilities in order to improve the overall safety related to these vehicle operations.

Acknowledgements

Contents

List of Tables

List of Figures

Chapter 1

Foreword

In the last few years, Unmanned Aircraft Systems (UAS) have become widely popular solution for recreational and commercial applications. Low costs, high flexibility and new advanced flight modes allowed thousands of applications beyond the boundaries of conventional remote sensing scenarios. Among the various types of UAS, rotary wing aircraft, and in particular multirotor platforms, offer great potential in harsh environments. Earthquakes, avalanches, and floods are few example of applications where multi-copter UAS provide benefit and in the next future they will support and partially replace manned vehicles involved in dangerous missions. As an example, the Mars Helicopter *Ingenuity*, recently launched by NASA, is a small aircraft designed to operate autonomously in the Martian atmosphere were challenges due to temperature and pressure conditions [5] are important aspect to focus on during the designing phase of the UAS.

In the context of Smart Cities, robotic aerial platforms will be extensively leveraged to provide services to citizens, e.g. collecting data for monitoring and security purposes [88]. Vertical take off and landing as well as hover capabilities of multi-copter UAS make these vehicles extremely suitable for applications such as surveillance and delivery of small package, especially when fast intervention is a driving requirement. In this scenario, UAS provide a way to overcome natural and artificial barriers which characterize the urban environment, such as river, bridges, railways and traffic. The feasibility of UAS operation in cities requires an adequate Unmanned Traffic Management System (UTM) which can handle vehicle's trajectories without compromising safety [52]. Critical information concerning the interaction between weather conditions and UAS power consumption, motor speed and propeller thrust will be mandatory for a safe application of Unmanned Aerial Vehicles (UAVs). In the past years, some experimental activities have been carried out on small UAS and their power system.

The characterization of propellers for small unmanned aerial platforms by Brandt and Selig [11] provided a reference database to highlight thrust production and power consumption of propellers, especially when low Reynolds flow conditions occur. Another major contribute was given by Russell [99] related to experimental measurements

of UAS performance at NASA Ames wind tunnel. The author provided a complete database on overall thrust and power consumption of commercially available multicopters. However, few experimental data on UAS performance in unconventional environments are available in literature. In 2016, PrecisionHawk [86] in collaboration with the Automotive Centre of Excellence at the University of Ontario, Canada, made environmental tests on multirotor and fixed wing UAS. Unfortunately, test results are not available for research purposes. More recently, a relevant works on propeller thrust generation in dynamic ice accretion conditions were published [41, 57, 58, 59]. These experimental studies accounted for the aerodynamic performance of rotating blades in several water content and operating temperature conditions.

Another important aspect related to UAS industry is the heavily use of commercial-of-the-shelf (COTS) components to ensure low market prices. COTS usually experience higher failure rates than aeronautical products as predictable lifetime is not a driving requirements when designing low cost UAS platforms. In the analysis of one hundred drone events reported in [122], it is shown that the *equipment problem* is the third cause of UAS uncontrollability experienced by users.

To overcome the aforementioned issues, the UAS industry has recently started to provide information to end users concerning flight recommendations in unconventional environments. As an example, in the Alta 8 flight manual [32] by Freefly System, a table summarizing the maximum take-off weight as a function of temperature and altitude is provided. Data are based on predictions, real tests and user feedback beyond standard flight conditions. In a similar way, DJI has improved propeller design to allow safe operation at high altitude locations. A systematic approach on drone flight capabilities in high altitude flights and low temperature has not been carried out by the academic research community. Standard procedures for testing the propulsion system as well as the overall UAS are not defined in the industry either, resulting in unexploited vehicle capabilities. Moreover, a bias in the existing tests has been the non-reproducibility of the same climatic conditions. The experience reported by pilots when flying in specific atmospheres contribute to increase knowledge, but these efforts are not enough for a deep understanding of the phenomena.

1.1   Thesis contribution

The aim of this thesis is to study, design and test protocols for experimental measurements of UAS multirotor performance under unconventional atmosphere conditions. A dedicated climate-controlled facility is leveraged in order to carry out experimental data related to propeller and full vehicle capabilities in low temperature and high altitude environments.

The main objective of this thesis is to develop a systematic approach on small unmanned aircraft performance analysis, with particular regard to low Reynolds flow conditions and their effect on thrust generated by the propulsion system of multirotor UAS.

Test protocols are defined to collect a set of data and improve propulsion system design and modeling. The main contribution of the following study is a complete database on isolated propeller and full vehicle performance over a wide range of atmospheric conditions. Extremely low pressures (high altitudes) and temperature are considered to assess thrust and torque coefficient as well as power consumption of brushless motor used by the UAS industry.

A broader contribution of this study is the evaluation of engineering tools to predict propulsion system performance. The experimental data collected in this study provide a reference basis to highlight limitations of propeller prediction when unconventional weather conditions arise.

1.2 About this PhD thesis

This work is the result of three years Ph.D. activities in the field of *Unmanned Aircraft Systems* at the Politecnico di Torino and in collaboration with Eurac Research - terraXcube, a private research institute in Bolzano, Italy. Eurac Research has an interest in exploring unmanned aerial vehicle technologies in order to develop services for national UAS companies, with particular regard to local manufacturer based in South Tyrolean area. Eurac Research consists of eleven institutes organized into four areas: autonomy, mountains, technology and health. terraXcube is part of Eurac Research facilities and aims to safely study the effects of different climactic conditions on human physiology, alpine ecology and industrial products. Its activities address the needs of mountaineers, rescue operators, farmers and other entrepreneurs working in the Alps, or on the high-altitude mountain peaks elsewhere in the world. The research fields covered by terraXcube are mountain medicine and alpine ecology. The research here presented has the goal to study and implements solutions for the characterization of Unmanned Aerial Vehicles under extreme environments with a systematic approach.

1.3 Outline

The aim of this PhD thesis is to develop a methodology for experimental testing of UAS multi-copter systems inside an environmental simulator, in order to evaluate performance of such vehicles with a systematic approach. In Chapter 2 a review of facilities for experimental testing of air vehicles, with particular regard to UAS, is presented, including wind tunnels and altitude chambers to point out their differences. terraXcube laboratory is presented and its features and potential for UAS testing are highlighted. The aerodynamics of propellers and multi-copter UAS are presented in Chapter 3, where mathematical models used to predict performance are discussed. Chapter 4 describes the experimental setup designed for the purposes presented in this research. A discussion on sensor selection, propulsion system and quadrotor used for testing is reported.

Moreover, test methodology is presented in terms of simulated atmospheres and protocols for data collection. Test results are reported in Chapter 5 for both isolated propeller and full vehicle in order to highlight atmospheric effects on thrust and power coefficients owing to the particular temperature and altitude simulated. A comparison with other experimental data available in literature is also included and secondary effects on brushless motor performance owing high altitude and low temperatures are described. All the experimental data are given in Appendix A and B for propeller and quadrotor respectively. Propulsion system simulation is reported in Chapter 6, with a particular regard to the implementation of the Blade Element Momentum Theory for the propeller used during the experimental tests. Implementation details of the simulations are in Appendix C. Details on indoor navigation systems for UAS applications are in Appendix D as UAS performance assessment inside the environmental simulator during free flight tests are of interest for future works. Conclusions are drawn in Chapter 7.

Chapter 2

Facilities for experimental testing of UAS

2.1 Introduction

The objective of the following Chapter is to describe facilities involved in experimental testing of Unmanned Aerial Systems. As stated by Russell [99], «*a research effort is needed to understand how small unmanned aircraft perform under a range of environmental conditions*». These experimental data are primarily required to safely integrate UAS vehicles with manned aircraft and allow urban operations. While innovative strategies to bring Artificial Intelligence onboard UAS are now emerging, there is still a lack of knowledge related to performance analysis on such vehicles when unconventional weather conditions are considered. In the past, testing of UAS in windy environments allowed the development of autopilot control law able to handle gust. Today, the most important question is the reliability of UAS in low temperature and high altitudes. These data are extremely useful in the context of Unmanned Traffic Management (UTM) [52] as will increase safety and efficiency usage of UAS according to their peculiarities.

This Chapter is organized as follows. In Section 2.2 the focus is given to wind tunnels as the major experimental tests in literature are performed in these facilities. Details of wind tunnel characteristics and flow qualities are presented to highlight the difference between a wind tunnel and the environmental simulator leveraged in this study. A review on UAS testing in wind tunnel is reported in Section 2.2.4 to present the state of the art on performance measurements of these vehicles. In Section 2.3 the attention is given to altitude (*hypobaric*) chambers, the particular facility to which terraXcube belongs to. Details of this environmental simulator are provided to underline the primary objective of this laboratory is related to medical research. However, as it will be explained, this innovative simulator can also be used for industrial testing. Hence, discussion of benefit and limitation of terraXcube testing are in Section 2.4.

2.2 Wind Tunnels

Experimental testing is a fundamental step when developing a new technology. Analytical and computational results require validation with real data to assess predictions based on mathematical models and their implementations. Wind tunnel testing plays a major role in aerospace engineering due to the complexity of flow fields over aeronautical vehicles.

A wind tunnel is a facility designed to create inside its test section a flow that is as near as possible to real flow conditions [8]. Based on wind tunnel measurements, engineers are able to evaluate forces, visualize complex flow conditions or improve the aerodynamics of elements under test.

A review of wind tunnels is out of the scope of the present work; however, wind tunnel characteristics are summarized for a comparison with the facility used in this study. Whether an open or closed circuit low speed wind tunnel, some essential elements are the followings. The flow is generated by a *Fan* controlled by a *Drive Motor*; *Flow Straighteners* (i.e. honeycombs and filters) are used to make the flow as uniform as possible in a dedicated *Settling Chamber*. A *Contraction Section* is used to accelerate the flow before entering in the *Test Section*, where the model is installed for testing. The Test Section has the smallest cross-sectional area resulting in the highest velocity in the tunnel. Moreover, a *Diffuser* is employed to expand and slow-down the flow before returning to the Fan (closed circuit) or exit (open circuit).

The architecture of a wind tunnel is strictly related to the purposes of the measurements to be taken during the experimental activities. Even though the development of wind tunnels is almost related to aeronautical applications, these laboratories are involved in many research fields, as summarized in Table 2.1 [8]. For the purpose of this thesis, aeronautical and automotive wind tunnels are of major interest and a short description will be provided for both of them.

2.2.1 Aeronautical Wind Tunnels

Considering aeronautical applications, the major issues are collection of aerodynamic forces data (lift and drag) as well as the dynamic response of the vehicle to commands. Detailed analysis of the aerodynamic field generated by an aircraft requires dedicated instruments (force and moment balances, airflow transducers, pressure sensors, etc.) as well as the capability to match the similarity parameters. The latter are essential to generate an aerodynamic flow representative of real conditions, as stated by the aerodynamic similarity principle [2].

One of the challenge in wind tunnel testing for aeronautical application is the capability to match high Reynolds numbers experienced by aircraft during flights. Even though model vehicles are usually employed for testing, high flow speeds are required. For this reason, in order to match the Reynolds number and leverage the aerodynamic similarity principle, in the past cooled wind tunnels were developed to increase the air

density and the corresponding Reynolds number. In other cases, pressurized wind tunnels were designed so that the air temperature decrease is exploit to reach the desired Reynolds. A major limitation is driven by fan capabilities to properly accelerate the airflow. During the designing phase of a wind tunnel, an acceptable balance between flow speed and energy consumption is also needed.

Application	Description	Reference Facility
Aeronautical Wind Tunnel	Measurements of aerodynamic forces and moments on aircraft and space vehicles	Nasa Ames Full Scale Aerodynamic Complex - California, USA
Automotive Tunnel	Experimental investigation of aerodynamic parameters that affects automobile performance, including handling qualities, engine and brake cooling	ACE Climatic Wind Tunnel - Ontario, Canada
Aeroacoustic Wind Tunnel	Experimental research on noise generated by flow and way to suppress it	Nasa Glenn Aero-Acoustic Propulsion Laboratory - Ohio, USA
Wind Engineering Tunnel	Facilities used to study problems related to natural wind, including interaction with buildings, air pollution and mass transportation	WindEEE Research Institute - Ontario, Canada
Smoke Tunnel	Flow visualization	Nasa Dryden Flow Visualization Facility - California, USA
Water Tunnel	Investigation of water flow phenomena such as underwater vehicle development, pump cavitation and flow visualization	Cavitation Laboratory Norwegian University of Science and Technology - Norway

Table 2.1: Types of Wind tunnel by applications [8]

However, considering small UAS vehicles , Low-Speed tunnel facilities are enough

as air viscosity is the primary phenomena of interest, while airflow compressibility can be neglected. During the pioneering years of UAS development, the dynamic behaviour of vehicles was investigated in Free Flight and Spin Tunnels. These are vertical wind tunnels with the air drawn upward by a propeller near the top of the tunnel. In the 1930s, NASA developed vertical tunnels to study the dynamic stability and controllability of model aircraft with a particular regard to after stall spin conditions of some fixed wing aircraft [129]. More in general, Free Flight Tunnels allow to define actions required to recovery an aircraft from dangerous flight conditions and provide insight on specific maneuvers. As an example, NASA Langley 20-ft Vertical Spin Tunnel is still in operation and was used for multicopter free flight tests [31] as described in Section 2.2.4.

Another major problem assessed in aeronautical application is ice accretion over wings, probes, engine nacelles or propeller blades. Different type of ice may be observed according to the environmental conditions, such as *hard-rime*, *milky* or *clear* ice. Icing Tunnels are conventional wind tunnels equipped with a refrigeration system able to reduce the air temperature to freezing values (i.e. -40 ℃). These facilities allow a systematic study on ice accretion and all the anti/de-ice device to prevent catastrophic flights. To this end, a water droplet generation system (nozzles) is usually involved to control the water content and droplet size, allowing to reproduce supercooled water conditions. To this end, a preliminary open circuit ice tunnel was developed in terraX-cube [4] in order to provide a qualitative understanding of ice accretion phenomenon over wings for different temperature and pressure combinations.

2.2.2 Automotive Wind Tunnels

Automotive applications require dedicated tunnel facilities to take measurements representative of real road airflows. Some important difference between aeronautic and automotive wind tunnels are highlighted.

First of all, small dimensions of ground vehicles usually allow the construction of full-scale facility so that testing at full-scale Reynolds numbers are much more feasible than the aeronautical sector. Moreover, two types of facilities are leveraged by the automotive industry. Aerodynamic wind tunnels are extensively used to investigate the airflow surrounding the vehicle and its interaction with internal flows. On the other hand, climatic wind tunnels play a major role in the automotive industry for the evaluation of onboard drive subsystem, such air-conditioning, engine performance during cold or hot start. For this reason, climatic tunnels are usually characterized by worsen airflow qualities as they are built for other testing purposes.Despite aeronautical applications, automotive testing requires relatively limited flow speed so that 20-30 m/s are enough to reach Reynolds numbers of interest [35]. Another major research topic is related to the aeroacoustic comfort onboard road vehicles. Tests are made to reduce noise levels and for this reason, dedicated sensors are essential to measure with accuracy the noise associated with flow around the vehicle and assess design improvements [8]. Slotted

walls or self-correcting open jet facilities [60] are common solution to reduce boundary interferences, such as solid blockage and horizontal buoyancy.

The major difference between automotive and aeronautic wind tunnels is ground effect simulation which is an essential element for the aerodynamics of road vehicles. In an automotive wind tunnel, the vehicle is stationary while the flow is blowing. The relative motion between the car and the road must be properly simulated to obtain a representative aerodynamic field. For this reason, automotive wind tunnels employ moving belt, distributed suction or tangential blowing to reduce the influence from floor boundary layer [60].

Despite differences between aeronautical and automotive wind tunnels, in the past years, automotive wind facility were leveraged even for experimental testing on UAS. The possibility to set low temperatures is the primary reason to exploit climatic automotive facilities to collect data on unmanned aircraft, as presented in Section 2.2.4.

2.2.3 Flow qualities

Considering a general purposes wind tunnel with an empty test section, the airflow should be parallel to the centreline, uniform and stationary in time. Moreover, no up-flow or cross-flow conditions, which means no turbulence, should be achieved. However, this is an ideal flow and real experiments inside any wind tunnel would be affected by some turbulence and noise. As reported in [8], velocity variation across the test section are quoted in the range of 0.2% - 0.3% from average, resulting in 0.4% - 0.6% change in dynamic pressure. Unwanted effects of turbulence may consists in incorrect drag, lift and velocity profile as well as shift from laminar to turbulent significantly upstream os its actual location [64]. Moreover, influence on boundary layer as well as skin friction may be possible.

As reported is [81], wind tunnel flow qualities are characterized by turbulent velocity, pressure noise and temperature fluctuations. Guidelines for wind tunnel performance assessment are given in [78]: airflow quality requirements are reported in term of turbulence, noise, pressure and temperature distribution to be satisfied inside the test section volume. To give an idea of the complexity related to a subsonic wind tunnel calibration, according to [83], the calibration process is completed when dynamic and static pressure variations as well as flow angularity, turbulence and extent of large-scale fluctuations are known. The calibration process of a low speed wind tunnel may require hundred of runs depending on how many troubles are identified and successfully eliminate. Dedicated sensor probes (i.e. turbulence sphere, yaw-meters) are needed for a complete description of the airflow inside the test section; moreover, the tunnel characterization should be accomplished considering different flow speeds, especially if variable pitch fan blades are installed [83].

2.2.4   UAS testing in Wind Tunnels

Preliminary studies related to rotor inflow and high lift device wake were carried out at NACA/NASA Langley Research Centre through 1950 and 1960 [22]. In particular, Heyson investigated wall effect influence on measurements of high lift device; in [44] the author pointed out that conventional wind tunnel correction factors, usually based on the assumption of lightly loaded model or small force coefficients, are not valid when testing rotor-craft. The reason is due to the strong wake interaction with tunnel constraints (such as floor and walls) that result in tunnel flow conditions not representative of real free-flight airflow. While test protocols for airfoils investigation in wind tunnels were developed since the dawn of aeronautical industry, rotor-craft testing requires more attention due to the complexity of the aerodynamic field as reported by the experimental study performed by Rae [93] on Vertical and/or Short Take-Off and Landing (V/STOL) aircraft. Suitable testing conditions for high lift wake device were defined by Heyson for experiments in wind tunnel facilities provided the fact there is enough distance between the rotor plane and tunnel floor, due to rotor wake impingement with the laboratory floor.

The rapid growing of commercial UAS has lead to more interest in performance analysis of these vehicles to answer open questions concerning their endurance and range capabilities. Preliminary wind tunnel measurements on small scale UAS accounted for propulsion system rather than full vehicle tests.

Low Reynolds airflow condition is a major topic for propeller design and characterization. It is important to highlight that the combinations of motor speed and propeller dimension for Micro Aerial Vehicles (MAVs) and small UAS usually result in low Reynolds number compared to those achieved in other aeronautical applications. A major contribution on this research topic was given by the University of Illinois at Urbana-Champaign (UIUC) since 2005. In this facility, Brandtl performed wind tunnel tests on 79 propellers with diameter in range $9'$ to $11'$ [12] considering different airflow speed. Results highlighted limitations of analytical methods to estimate thrust and torque when low Reynolds were achieved. A comprehensive study on propeller coefficients for small unmanned vehicle is also described in [26] by Deters. The author focused on Reynolds numbers below 100,000 to provide experimental data and overcome inaccuracies of numerical tools, not able to fully predict thrust and power in those airflow regimes. In this study, twenty-seven propellers off-the-shelf propellers with diameters ranging from $6'$ to $9'$ were investigated in the low turbulence subsonic wind tunnel at UIUC. A similar work is reported in [25], where static tests on micro propellers (diameter up to $2.25'$) were performed to focus on the aerodynamics very small Reynolds and fill the gap of limited data in literature. The experimental setup included a thrust load cell, a reaction torque sensor and an infrared tachometer for motor speed sensing.

The experimental activity performed at UIUC has been replicated by other universities with similar approaches. Many experimental researches on propellers are now

available in literature and most of them focus on static performance inside wind tunnels for different airflow speeds and ambient air temperature. Merachant et al. in [70] present wind tunnel data on propeller with larger diameter (up to 22′). Once again, the authors highlight that numerical predictions of these high-lift devices are not easy and on field testing is the most reliable way to obtain representative data. Two major difficulties arise when implementing numerical tools. Firstly, geometrical data of propellers, such as twist and chord distributions, are not always accessible; secondly, high quality aerodynamic database for airfoils at low Reynolds numbers are not available.

Other studies account for the propulsion system without considering only the aerodynamics of propellers. For example, electric current and power consumption of small scale propeller in wind tunnel tests are reported by Gamble in [34]; a similar investigation for a fixed wing propulsion system is detailed in [6].

In general, few experimental activities deal with full vehicle performance. However, since 2015 the rapid development of small commercial multirotor UAS has increased interest on performance of overall vehicles rather than the isolated propulsion system. According to [22], hobbyist level and commercially available small UAS are designed without great consideration given to aerodynamic interaction between propellers and airframe. Considering commercial applications, multicopter UAS are mostly involved in aerial photography and many efforts are made to optimize payload capabilities related to optical sensors rather than vehicle performance. However, the advent of a UAS Traffic Management platform [87] has required a comprehensive understanding of the overall vehicle performance (not limited to UAS payload) under standard as well as unconventional weather conditions.

Multicopter UAS wind tunnel test at NASA Ames

The first experimental activity on commercial and hobbyist-level multirotor UAS was carried out by the Aeromechanics Office at NASA Ames Research Center in 2016. According to Russell et al. [99], there is a need to determine if a given UAS aircraft is able to maintain stable flight under forecasted weather conditions. For this reason, the authors were involved in a comprehensive analysis on commercially available multirotors in both wind tunnel and hover conditions. In this project [99], five multicopter UAS were tested in the U.S. Army 7-by-10 wind tunnel at NASA Ames. These vehicles, including a DJI Phantom 3 (Figure 2.1), are common platforms for photographic surveillance. During the tests, all the vehicles were slightly modified to allow the installation on the sting balance used in the wind tunnel. The camera gimbals were removed and replaced with an interface plate with the sting attachment. Few other modifications were made to measure all the quantities of interest: while the brushless motors and propellers were the original components of each vehicle, the electronic speed controllers were replaced to allow measurements of motor current, voltage and manual control of the copters. Motor speeds were recorded with electric brushless motor sensors; moreover, thrusts and moments were measured using a six axes load cell. To avoid battery charge time,

a dedicated power supply was used. The rotor speeds were manually controlled by the test engineer; baseline values were defined in order to generate approximately the manufacturers' nominal flight thrust. Motor speeds were defined to sweep values in the range 80 to 120 percent of the baseline. The same motor angular rates were set for all the tests: different motor speed as well as airflow were considered within the defined test matrix. Thanks to the sting attachment, the authors were able to set a combination of flow directions with respect to the vehicles. In this way, forward flight as well as hover conditions were systematically investigated. The authors collected performance data (i.e. electrical power and current), motor speed as well as force and moments acting on each multicopter. Moreover, the effect of UAS airframe on thrust and moments were presented as aerodynamic forces owing to the vehicle bare airframe were measured. Isolated rotor test for each propulsion devices were carried out, as shown in Figure 2.1 for a 15'x5' *T-Motor* device. As geometric data of commercial propellers are usually unknown, a 3D laser scanner was used to collect a point cloud and define a three-dimensional model of each propeller. The complete test details and results are reported in [100]. According to Danis [22], *"the resulting performance data likely represents the most in-depth and professionally gathered published data for hobbyist-level multirotor vehicles"*.

(a) *DJI Phantom 3* (b) *T-Motor* 15*'x* 5*' propeller*

Figure 2.1: Multicopter UAS tunnel test at NASA Ames [99]

An additional setup was developed to measure noise level of each multirotor vehicle. As reported in [39], the U.S. Army's wind tunnel test was equipped with acoustic sensors to collect motor noise of commercial multicopter UAS. The main limitation of this setup was due to the wind tunnel is not an anechoic environment and results must be properly interpreted. The authors included a detailed investigation of the wind tunnel background noise at different flow speeds, showing a non-linear relationship between the Overall Sound Pressure Level (OASPL) and wind speed. According to [39], as the rotor speeds increase the OASPL increases as well with a non-linear trend. On the other

hand, as expected, the vehicle attitude with respect to the airflow (pitch and yaw were tested) do not affect the overall sound pressure level.

Even though further analysis should be required for a comprehensive acoustic investigation, the aforementioned are an additional step to understand unmanned aircraft system, with particular regard to their integration in urban area.

Additional wind tunnel tests on multicopter UAS

Since NASA Ames experimental research on multicopter UAS, other institutions have deal with wind tunnel testing of small unmanned vehicles with particular regard to multirotors. The DJI Phantom 3 were tested inside the 3' by 4' wind tunnel at California Polytechnic State University in 2018 by Reed Danis [22]. The test stand used to perform all the measurements was similar to those describe by Russell. One more time, a sting support was leveraged to install the multirotor in the test section of the low speed tunnel. Forces and moments were recorded using a six axes load cell; rotor speeds as well as electric current and power were also taken. The sting support was connected to a pitch axle in order to be able to modify the pitch angle with respect to airflow direction, as shown in Figure 2.2. In addition, the author performed Particle Image Velocimetry (PIV) analysis to visualize the wake generated by the rotor-craft. A side-by-side comparison with NASA Ames data was reported by Danis. The author showed test results exhibit the same trends as for NASA Ames; however, significant difference in magnitude were experienced in aerodynamic forces and power measurements even tough test procedure as well as the dynamic pressure were essentially the same as for tests performed by Russell. According to [22], discrepancies may be related to wind tunnel interference effects owing to the smaller test section compared to NASA Ames facility. To support this idea, the author performed wake visualization as well as an additional test with the UAS near the wind tunnel floor. This additional measurements confirmed the strength of tunnel interference strongly affect multirotor data collection in this laboratory.

Few other works deal with small multicopter testing in wind tunnel facilities. Baris et al. [7] investigated the dynamic behaviour of a DJI Phantom 3 in the Old Dominion University (ODU), Virginia, USA. As shown in Figure 2.3, the authors leveraged a Stewart-Gough platform. Linear actuators were driven by stepping motors in order to reach a desired attitude. The multirotor was installed over a six axes load cell; additional sensors include motor speeds and an inertial measurement unit (IMU). The side-by-side comparison performed by the authors with NASA Ames test results showed similar trend even though thrust deviation as the motor speeds were increased. The overall difference was reasonable and could be related to different sensor architecture as well as reduced wind tunnel test section dimensions.

UAS Drag coefficient estimation was taken by Mascarello [65]. The author provided a technical solution to make UAS *harmless* vehicles as most of them are designed without safety considerations. Mascarello developed a cover protection system to reduce
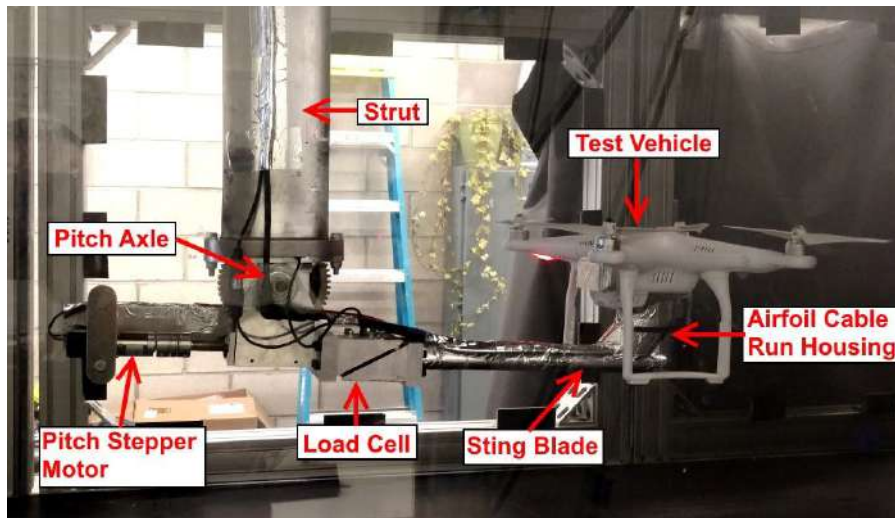
Figure 2.2: DJI Phantom 3 wind tunnel test bed at California Polytechnic State University [22]

the severity of impact in case of failure. The aerodynamic performance of a commercial UAS with a dedicated cover protection system and without it were made in a tunnel facility. According to [65], the proposed safety device allows to drastically reduce the kinetic energy despite the overall increase of drag coefficient which may compromise vehicle endurance.

In other research studies [36, 42, 48, 121], the focus is given to wind tunnel tests for fixed-wing aircraft. Compared to measurements on multirotor platforms, fixed-wing UAS require limited sensors and take advantage of conventional support and sting balances normally installed in wind tunnel facilities. The reason is that wind tunnels have been exploited for aerodynamic investigations of fixed-wing aircraft models since the beginning of the aviation industry, while multirotor platform are quite innovative. To give an idea of the complexity when testing multirotors, a dedicated test bed design is reported in [18]. The proposed Multirotor Test Bed (MTB) is intended to collect experimental data on complex rotor vehicles, with 6 or more propellers. The technical solution described by Conley allows to adjust vertical, aft as well as longitudinal placements of each rotor. Moreover, control of the pitch of each rotor and the whole assembly is possible.

An other important topic in UAS testing is the evaluation of their performance during flight. Even though wind tunnel tests provide important data on thrust coefficient as well as power consumption in both static and airflow conditions, flight tests are needed to assess autopilot control capabilities and vehicle stability. The dynamic behaviour of small commercial multirotor is reported in [31], a test project performed by NASA Langley Research Center. Free flight tests were conducted in the 12-foot Low Speed Tunnel

Figure 2.3: DJI Phantom 3 wind tunnel test bed at Old Dominion University [7]

as well as in the 20-foot Vertical Speed Tunnel. Forster et al. developed a tethered system to prevent damages in case of loss of control or during failure analysis. Despite the characterization performed by Russell, the authors investigated the dynamic response of the multicopter to pilot commands as for real flight conditions. Some important hardware modifications were required: first of all, Li-Po batteries provided the electrical power instead of the DC power supplier used by Russell. Moreover, a tethered attachment pyramid system was designed to protect tunnel facilities. The tethered solution allowed a rapid in-flight recovery and was developed to impart minimal forces to the vehicle during operations. Flight logs from the onboard autopilot (Pixhawk®) were acquired and additional brushless motor sensors were installed to collect rotor speeds. Different vehicle gross weight were considered. At the same time, forward flight capabilities were tested in the LST facility without any test stand as made by Russell. The LST test results show the higher the flow speed the greater the pitch angle of the vehicle to keep the hover position. Tests performed in the vertical wind tunnel provided insight on multirotor capabilities during ascend and descend flights. Different flow speeds were set and the average rotor speeds to keep a stable flight are reported. A major contribution provided by Forster et al. is the analysis of flying qualities in terms of pilot work load. As an example, when the vortex ring state conditions are reached, the overall pilot work load is maximum. In these conditions, the altitude controller allows to reduce pilot work load compared to the use of stabilize flight mode only. An other important topic highlighted by Forster is the vortex ring state and wake re-ingestion effects on vehicle controllability and stability. Off-nominal flight conditions, such as rotor failures were simulated and test result revealed windmill conditions are experienced suggesting

this is an important aerodynamic condition to be considered when modelling failures.
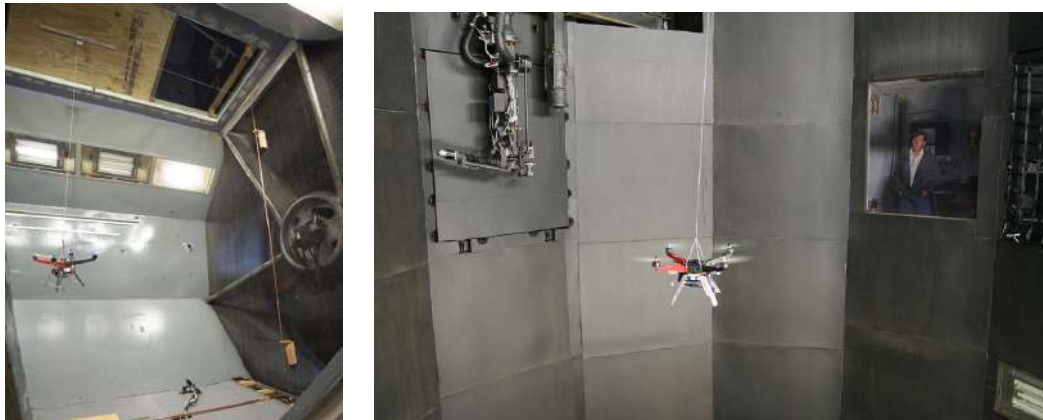
(a) *Multirotor UAS testing in the Low Speed Tunnel*

(b) *Free flight testing in the Vertical Speed Tunnel*

Figure 2.4: Multirotor free flight test at NASA Langley Research Centre [31]

Finally, in 2016 the Automotive Center of Excellence (ACE) in Ontario, Canada, performed climatic test in collaboration with PrecisionHawk [85] to investigate low temperature effects on a fixed wing UAS. Unfortunately, tests results, protocols and details on the instrumentations were not described by the researches. In a similar way, the Wind Engineering, Energy and Environment Research Institute (WindEEE) in Canada was involved in multirotor testing in strong wind Qualitative tests were performed and no quantitative results were reported to the readers for additional analysis.

A custom facility for multicopter testing

To conclude this Section, an additional facility is reported as specifically designed for multirotor vehicles. According to [49], there is a need to account for gust effects on MAV and UAVs. Indeed, in contrast to larger vehicles *"where the magnitude of gust is small when compared to the mean flow, gust magnitudes can be as large or larger than the mean flow for these small vehicles"*. This is particularly true in urban area where buildings create unstable flow conditions which affect small UAS flights [36, 121]. As described in Section 2.2.3, wind tunnels usually have flow qualities that result in low turbulence levels and steady unidirectional flows. These conditions are not representative of real airflows owing to wind gust and shear that can be experienced in cities (i.e. urban canyons).

Johnson et al. presented an innovative solution to simulate complex flow conditions with a systematic approach [49]. The setup consists of a bank of computer fans powered by a DC power supplier. As reported by the authors, the maximum flow speed is 5 m/s; moreover, the overall system proposed by Johnson suffers low fan response and uniform gust size resulting from limited dimension of each fan. More recently, Noca et

al. [76] made improvements on this initial attempt. Their technology is commercialized by a Swiss company and the first facility was installed at the California Institute of Technology. The facility consists of 1296 computer fans (Figure 2.5) and its modular design allows testing of different flow conditions such as descend, turbulent and conventional wind tunnel. A comprehensive flow analysis as reported by Johnson [49] was not performed by Noca et al. and it is difficult to assess advantages of this innovative solution compared to wind tunnel facilities.
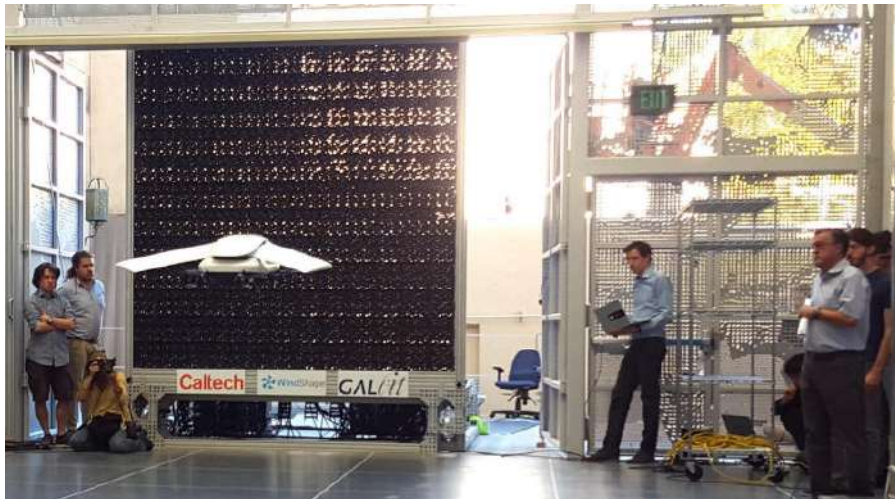
Figure 2.5: WindShape technology for UAS testing [76]

2.3   Altitude Chambers

An altitude chamber, also referred as *hypobaric* chamber, is a medical facility used to investigate high altitude effects on human bodies or to test performance of industrial products.

Medical Facilities

Experimental research on human physiology requires dedicated laboratories to simulate desired altitudes. Hypoxia and hypobaria conditions are the main research topics where altitude chambers have a relevant role. As reported in [108], hypobaric training chambers were primarily developed for military applications, and since 1960 also for civilians. Pilots and crew members are trained to familiarize with symptoms of hypoxia as they are different for each person: the systematic approach of altitude simulators allow the understanding of symptoms in a controlled safe environment for pilots and crew members.

A typical test session for hypoxia effects on human body is reported in [115] where the experience of FAA altitude chamber in Oklahoma is presented. All the training

sessions were performed for the aviation populace by the FAA Civil Aerospace Medical Institute (CAMI). Over the years (1965 to 1989), two altitude profile were used and according to [115] they both provide a safe learning environment without compromise attendants' safety. Before starting the test, all the trainers are medically screened, seated inside the chamber and taken to a target altitude (6000 or 7000 ft according to the protocol [105]). Firstly, a rapid descent is simulated to remove from the test participants suspected to suffer unsuitable physiological manifestations. Then, a rapid decompression is experienced up to a target altitude of 25,000 or 30,000 ft. During the high altitude exposure time, trainers experience symptoms of hypoxia and are asked to perform simple tasks such as mathematical calculations or logical problem. Protocols include students are involved to a maximum time of 5 minutes without supplementary oxygen to familiarize with their own symptoms. Figure 2.6 shows CAMI test section and a typical altitude profile.

(a) *Test section* (b) *Altitude profile*
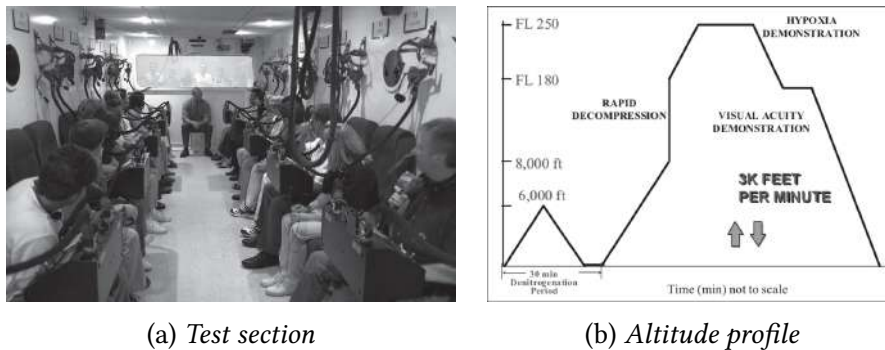
Figure 2.6: Hypoxia training session inside the FAA Civil Aerospace Medical Institute [105]

According to [125], the five most commonly reported hypoxia symptoms are dizziness, lightheaded, tingling, mental confusion as well as visual impairment. Effect on work load capacity in high altitude environment are discussed in [28], while extreme altitude effects on eye and vision perception are presented in [109]. A review on medical effects related to human body exposure to high altitudes is out of the scope of this work. However, the aforementioned studies provide an idea of altitude chambers used for aviation medicine ad well as suggest the importance of these facilities for training to recognize hypoxia effects.

Industrial Facilities

Altitude chambers are widely used also for industrial testing. Propulsion system performance during cruise is a major research topic since the development of engines. Comprehensive studies on propulsion devices were carried out by NASA Glenn Research Centre including piston engines, turbojets, turboprops and ramjets between 1944 and 1975 [73]. Today, vacuum chamber facilities are still used at Glenn Research Centre for

studies on innovative electric and chemical propulsion as well as space environments simulation.

The NASA Glenn Propulsion System Laboratory (PSL) is a facility for air-breathing propulsion system testing up to 90,000 ft and high Mach numbers. As reported in [80], the facility was used for icing engine test at different altitudes. The objective of the work was to understand crystal ice conditions and their effects on turbofan engines. The major result is a set of data that allow the definition of altitude scaling laws to assist engine manufacturers while assessing icing conditions. In a similar way, ice accretion tests were performed in the PSL facility using a NACA 0012 airfoil, as reported in [9]. Castner et al. leveraged the PSL facility to investigate the performance of a Pratt and Whitney jet engine in [14]. The aim of this experimental research is to generate a database for engine capabilities to be involved in high altitude surveillance UAV applications. A comparison between measurements and analytical models is proposed as the facility allows a real flight environments for propulsion testing, including cold air operations (down to $-45°C$). The report focuses on airflow data and low-pressure turbine performance: altitude data were collected at 45,000, 55,000 an 65,000 ft to improve numerical tool for turbine performance predictions. A similar work is reported in [120] with emphasis on unmanned vehicles operating at high altitude conditions. The NASA Glenn Research Centre includes vacuum test chambers for chemical propulsion testing as well as facilities for In-Space Propulsion (ISP). The latter allows a test section for full scale testing of the upper stage launch vehicles and rocket engines under simulated space conditions. The facility provide two operational mode: thermal vacuum simulation and altitude propulsion testing [51].

While industrial altitude chambers are mainly used for propulsion [123] and space testing as well as automotive engine performance [119], small facilities were also developed to evaluate capabilities of electronic devices. As reported in [47], low pressure operating conditions can be predicted using ideal gas law and heat convection equations. However, details on geometry as well as materials are needed to perform accurate computation and these data are rarely reported in technical data-sheets. In these cases, experimental testing is essential to have evaluate working capabilities of equipments.

2.3.1   terraXcube Extreme Environmental Simulator

terraXcube is an innovative research laboratory in Bolzano, Italy, designed for medical purposes and able to simulate extreme environmental conditions. The facility was launched in November 2018 and as reported by [74], the facility allows a systematic approach to safely study the effect of climate conditions on human physiology as well as industrial products. Alpine medicine and ecology are the main research topics carried out by Eurac researchers involved in this facility.

The facility consists of five altitude chambers organized in two units [75]. The Small Environmental Chamber (SEC) is designed for ecological research and includes

four independent climatic chambers (LxWxH 3x3x3 m each) that can be controlled individually or simultaneously. Inside the SEC, barometric pressure can be reduced up to 600 mba and temperature is controlled within the range -20 ℃ to $+50$℃; moreover, it is possible to set desired humidity, oxygen as well as carbon dioxide concentrations and simulate solar radiation and rain.

The most interesting infrastructure is the Large Environmental Chamber (LEC) which is designed for mountain emergency medicine and industrial testing. This large chamber (LxWxH 6x12x5 m each) extends the capabilities of the aforementioned variables (pressure and temperature) to ranges reported in Table 2.2. Due to its medical purpose, in addition to the test section, other functional rooms are available, including an ambulatory room and an airlock. Figure 2.7 shows the test section and control room of the large chamber facility.

Feature	Value	Precision
Maximum altitude	9000 m	±10 m
Maximum Rate of Climb	6 m/s	Not available
Minimum Rate of Climb	0.1 m/s	Not available
Temperature range	-40℃ to $+60$℃	±1℃ in time, ±2℃ in space
Temperature Rate of Change	±0.5℃/min (cooling and heating)	Not available
Relative Humidity	10% to 90%	±3 %

Table 2.2: terraXcube - Large Environmental Chamber [112]

The test engineer in the control room is in charge of the atmospheric conditions of the test section and set up the environmental variables according to the needs. The test engineer does not have a direct control of the test section pressure: the set-point altitude is defined and the control software of the facility computes the corresponding pressure exploiting the barometric equation

$$p = p_0 \left(\frac{T_0 - Kh}{T_0} \right)^{5.255},$$ (2.1)

where p_0 and T_0 are the standard pressure and temperature (respectively $p_0 = 1013.25\ hPa$ and $T_0 = 288.15\ K$), h is the set-point altitude in meters and K is the standard temperature gradient according to the International Standard Atmosphere (ISA) - $K = 0.0065\ K/m$.

(a) *Test section*   (b) *Control room*
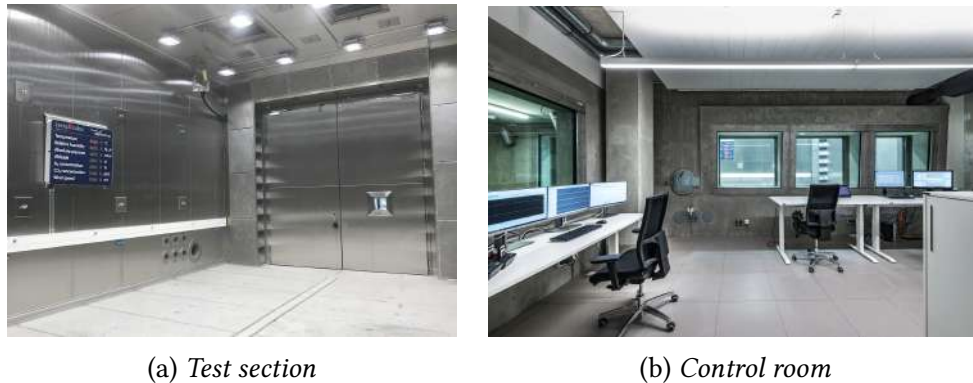
Figure 2.7: terraXcube Large Environmental Chamber (LEC)

2.4   Final considerations

In this Chapter, facilities for UAS testing were explored, including wind tunnels and altitude chambers.

Wind tunnel characteristics were presented as these facilities are mainly used for small scale unmanned vehicles. While preliminary studies focused on propulsion system, more recently full vehicle performance were investigated in wind tunnels. The best flow qualities in term of low turbulence are offered by aeronautical tunnels; moreover, they can be leveraged for full scale testing as commercial and recreational UAS usually have limited dimensions. Vertical wind tunnels important facility to investigate free flight conditions as well as stability and controllability of UAS.

The major contribution in small UAS experimental testing was given by NASA thanks to a comprehensive study on five multirotors UAS. Performance analysis at different flow speeds and attitude were performed at NASA Ames Research Centre and are fully described. These data are essential as low Reynolds effects are experienced by unmanned vehicles and numerical models are not able to predict thrust and power without detailed aerodynamic database. Another major contribution was given by NASA Langley, where researchers focused on free flight tests to evaluate autopilot capabilities, vehicle stabilities and response in failure conditions.

Altitude chamber characteristics were also presented as they offer the opportunity to perform industrial tests. Despite wind tunnels, these facilities are primarily designed for medical purposes. However, their capability to simulate low pressure conditions was leveraged to investigate propulsion devices for aviation applications. A systematic study on pressure and temperature influence on UAS performance is a relatively new research topics in UAS field. Large medical altitude chambers, such as terraXcube extreme simulator, can be leveraged to provide experimental data on UAS performance operating in unconventional weather conditions.

The objective of this thesis is to define protocols to exploit terraXcube capabilities and perform small scale UAS testing inside this environmental simulator. The main

limitation of terraXcube is that its performance are not comparable with a conventional wind tunnel facility. However, pressure and temperature control capabilities of this laboratory are leverage for a systematic study on vehicle performance, as any other research study account for the influence of these environmental parameters on UAS.

Chapter 3

Aerodynamics of Unmanned Aircraft Systems

The capability of multirotor UAS to generate thrust is strongly affected by aerodynamic performance of propellers. An optimal propeller design is required to reach desired requirements in terms of maximum thrust and power consumption. In the following Chapter important aspects related to UAS propulsion systems are summarized. While Section 3.1 focuses on the characteristics of isolated propellers, in Section 3.2 the focus is given to the overall vehicle aerodynamics.

Firstly, a review of mathematical tools used to predict thrust and power of isolated propellers is presented. Different approaches are possibles according to precision needed. In general, geometrical data of propellers are essential to perform all the computations. Details of a commercial propeller for small scale UAS are presented; while helicopter rotors are usually characterized by a constant chord and airfoil shape, it is common for propellers used for multirotor UAS have continuous varying twist, chord and airfoils. The mathematical description of propellers used by UAS is further complicated by non-linearities in the lift-drag polar owing to the *laminar separation bubble* as reported in Section 3.1.5.

Details on UAS vehicle aerodynamics are reported to highlight the importance of testing full vehicle performance as mutual rotor interaction may occur according to the relative position of the rotors. Important non linear effects such as ground, ceiling and wall interactions are recalled and the aerodynamic field in different flight conditions is summarized.

3.1 Rotor aerodynamics

Thrust and torque generated by a rotating propeller are affected by many factors, such as its geometry, flight conditions and environmental parameters. In the following paragraphs, a review of the major theories used to describe the aerodynamic behaviour of

a rotating propeller is presented.

With reference to Figure 3.1, basic definitions adopted in the next subsections are given. R is the propeller radius, used as reference length scale, while Ω is the rotor angular speed. In the more general case, considering a rotor flying forward, V is the relative velocity between air and propeller and α is the angle of attack. The rotor induced velocity, normal to the disk plane, is v. Moreover, it is possible to introduce dimensional velocity parallel and normal to the propeller plane which are the advance ratio μ and total inflow ratio λ respectively,

$$\mu = \frac{V\cos(\alpha)}{\Omega R} \tag{3.1}$$

$$\lambda = \frac{V\sin(\alpha) + v}{\Omega R} = \lambda_c + \lambda_i \tag{3.2}$$

where $\lambda_c = \mu\tan(\alpha)$ is the climb inflow ratio and λ_i is the induced inflow ratio. Moreover, thrust and torque coefficients based on air density ρ, disk area A and rotor tip speed ΩR are defined as follows [50]

$$c_T = \frac{T}{\rho A(\Omega R)^2}, \tag{3.3}$$

$$c_Q = \frac{Q}{\rho A R(\Omega R)^2}, \tag{3.4}$$

where T and Q are the rotor thrust and torque respectively. Recalling the mechanical power is $P = Q\Omega$, the power coefficient is

$$c_P = \frac{P}{\rho A(\Omega R)^3} \tag{3.5}$$

so that torque and power coefficient are essentially same, $c_Q = c_P$. As it will be discussed in Paragraph 3.1.5, while torque and power coefficients are almost constant with Reynolds number, the thrust coefficient is directly affected by airflow viscosity.

In the following sections, the analytical methods used to evaluate rotor performance are summarized considering the general case of forward flight. Advantages and limitations of the proposed mathematical representations are discussed.

3.1.1 Momentum Theory

The Momentum Theory (MT) allows to estimate rotor performance from a global point of view based on mass, momentum and energy conservation laws. The rotor disk is schematically represented as single *lifting surface*, made by infinite blades and characterized by infinitesimal thickness. The airflow is assumed ideal and no turbulent conditions occur, so that the downstream induced velocity is constant and blade tip losses are neglected.

(a) *Top view* (b) *Side view*
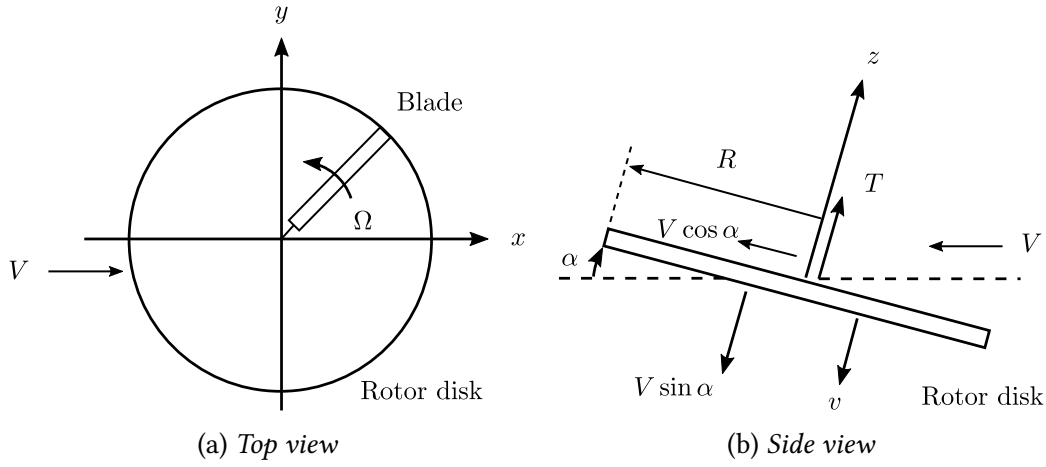
Figure 3.1: Rotor basic definitions
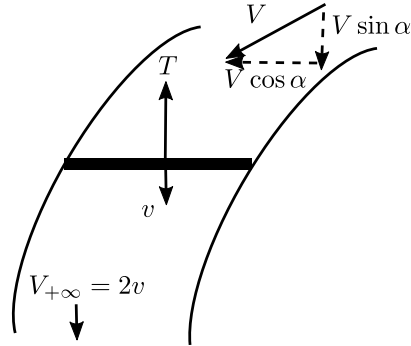
Figure 3.2: Momentum Theory flow schematization

Figure 3.2 shows a rotor in forward flight at velocity V with an angle of attack α. In the far wake, the airflow velocity is $V_{+\infty} = 2v$ [10] and is assumed to be parallel to the rotor disk. The momentum conservation gives the rotor thrust as $T = \dot{m}V_{+\infty}$; moreover, the mass flow rate is $\dot{m} = \rho A U$, where U is the resultant velocity in the rotor disk

$$U^2 = (V\cos(\alpha))^2 + (V\sin(\alpha) + v)^2 = V^2 + 2Vv\sin(\alpha) + v^2. \tag{3.6}$$

It follows,

$$T = 2\rho A U v = 2\rho A v \sqrt{V^2 + 2Vv\sin(\alpha) + v^2}. \tag{3.7}$$

Hover flight condition is obtained considering $V = 0$ so that Eq. (3.7) reduces to

$$T = 2\rho A v_h^2. \tag{3.8}$$

The Eq. 3.7 can be simplified if the forward flight velocity satisfy the condition

$V \gg v$, and the resulting approximated rotor thrust is computed as

$$T = 2\rho A v V. \tag{3.9}$$

Finally, the rotor mechanical power is given by the power conservation law

$$P = \frac{1}{2}\dot{m}(U^2 - V^2) = \tag{3.10}$$
$$= TV\sin(\alpha) + Tv.$$

The first term on the right side of Eq. (3.10) is the power required to climb and propel the rotor forward while the second term is the *induced power* needed to accelerate the airflow through the rotor disk.

To compute rotor induced velocity v, a common assumption is to consider T equal to the thrust in hover flight $T_h = 2\rho A v_h^2$ [50]. The induced velocity is obtained numerically by solving the following iterative equation

$$v = \frac{v_h}{\sqrt{V^2 + 2Vv\sin(\alpha) + v^2}}, \tag{3.11}$$

Finally, the induced inflow ratio λ_i as a function of v, λ and thrust coefficient is obtained

$$\lambda_i = \frac{c_T}{2\sqrt{\mu^2 + \lambda^2}}, \tag{3.12}$$

where the inflow coefficient λ is evaluated by a numerical iterative process given λ_i

$$\lambda = \mu\tan(\alpha) + \lambda_i. \tag{3.13}$$

While a numerical solution of the previous equations is always possible, non-physical results may be obtained owing to limitations of the Momentum Theory. Non-linearities related to turbulent-wake are responsible for unreliable thrust prediction especially for descend flight with a velocity component normal to the disk plane in the range $-2v < V\sin\alpha < 0$. This situation occurs when steep angle of attacks are experienced so that the assumption of uniform downstream induced velocity is not valid.

3.1.2 Blade Element Theory

The Blade Element Theory (BET) is used to compute rotor performance from a differential point of view applying the lifting line theory. A detailed description of BET can be found in [55] and in [104]. Figure 3.3 shows a generic rotor section (at distance r from rotor hub) and defines local quantities of interest. The local twist angle is θ and it varies according to the propeller geometry; the inflow angle is ϕ and U is the local velocity. U_p and U_t are respectively the parallel and tangential velocity component of U with respect to the disk plane.
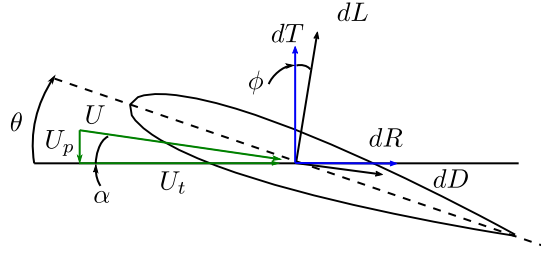
Figure 3.3: Rotor section

Local velocity and inflow angle are computed as

$$U = \sqrt{U_p^2 + U_t^2} \tag{3.14}$$

$$\phi = \arctan \frac{U_p}{U_t} \tag{3.15}$$

Moreover, the angle of attack is the difference between twist and inflow angles $\alpha = \theta - \phi$. The resulting incremental lift dL and drag dD per unit span on the blade element are

$$dL = \frac{1}{2}\rho U^2 c c_{L\alpha}\alpha \, dr, \tag{3.16}$$

$$dD = \frac{1}{2}\rho U^2 c c_D \, dr, \tag{3.17}$$

where c is the local chord, $c_{L\alpha}$ is the local slope of the lift coefficient c_L and c_D is the local drag coefficient. The incremental thrust and torque per unit span on the blade element are the following

$$dT = dL \, \cos(\phi) - dD \, \sin(\phi) \tag{3.18}$$

$$dQ = dL \, \sin(\phi) + dD \, \cos(\phi). \tag{3.19}$$

Considering the advance ratio μ and inflow parameter λ, the local velocities U_t and U_p are re-written as

$$U_t = \Omega r + \mu\Omega R \tag{3.20}$$

$$U_p = \lambda\Omega R \tag{3.21}$$

As U_p is usually smaller than U_T, it is possible to simplify previous equations (3.14), (3.15) and (3.18) as follows

$$U \approx U_t, \tag{3.22}$$

$$\phi \approx \frac{U_p}{U_t}, \tag{3.23}$$

$$dT \approx dL. \tag{3.24}$$

The incremental thrust force is

$$dT = \frac{1}{2}\rho c c_{L\alpha}(\theta U_t^2 - U_t U_p)\, dr. \tag{3.25}$$

Eq. (3.25) can be numerically integrated over the blade span. To this end, some important quantities are needed. Firstly, the number of blades N_b; secondly, propeller twist and chord distribution along the radius are essential. Furthermore, lift and drag coefficients as a function of Reynolds number and angle of attack are required for each section airfoil. While an analytical solution of Eq. 3.26 is always possible, the main limitation is that geometrical and aerodynamic data of propellers are not usually provided by manufacturers and further simplifications are made. A common assumption is to consider average values of chord, twist and uniform inflow [10] so that, given N_b blades, the total thrust is

$$T = \frac{1}{4}\rho c c_{L\alpha}\Omega^2 R^3 \left[\frac{2}{3}\theta\left(1 + \frac{3}{2}\mu^2\right) - \lambda \right]. \tag{3.26}$$

Moreover, if the solidity ratio $\sigma = \frac{N_b c}{\pi R}$ is introduced, the thrust coefficient is

$$c_T = \frac{1}{4}\sigma c_{L\alpha}\left[\frac{2}{3}\theta\left(1 + \frac{3}{2}\mu^2\right) - \lambda \right]. \tag{3.27}$$

A similar approach is used to compute the rotor torque given the incremental force dR defined as

$$dR \approx (\phi dL + dD)\, dr, \tag{3.28}$$

With the assumption of constant chord, twist and uniform inflow, the torque coefficient is

$$c_Q = \frac{1}{8}\sigma c_D(1 + 4.7\mu^2) + c_T\lambda - c_R\mu, \tag{3.29}$$

where

$$c_R = \frac{1}{4}\sigma c_{L\alpha}\left(\frac{\mu c_D}{2c_{L\alpha}} + \frac{1}{2}\mu\lambda\theta \right). \tag{3.30}$$

28

3.1.3 Blade Element Momentum Theory

The rotor aerodynamics is described with different approaches by Momentum Theory and Blade Element Theory. It is possible to leverage both methodologies in the well-known Blade Element Momentum Theory (BEMT). The fundamental idea is to combine the global perspective of MT with the differential approach of the BET based on the equivalence between circulation and momentum theories. Figure 3.4 shows an annulus dr along which BEMT is applied.
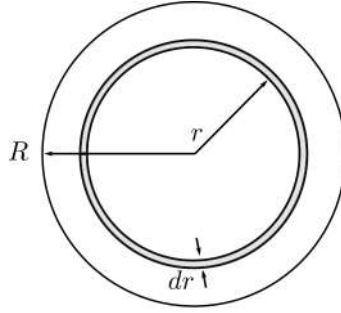
Figure 3.4: Blade Element Momentum Theory

Based on Momentum Theory, the annulus incremental thrust is

$$dT = 2v d\dot{m}, \tag{3.31}$$

at the same time, according to the Blade Element Theory the incremental thrust is

$$dT = N_b \frac{1}{2} \rho (\Omega r)^2 c c_{L\alpha} \left[\theta - \frac{U_t}{\Omega r} \right] dr . \tag{3.32}$$

The distribution of the inflow coefficient λ is obtained by imposing equality of Eq. (3.31) and Eq. (3.32). The inflow coefficient along the propeller radial direction is given by the following equation

$$\lambda^2 + \left[\frac{\sigma c_{L\alpha}}{8} \right] \lambda - \left[\frac{\sigma c_{L\alpha}}{8} \right] \theta \frac{r}{R} = 0. \tag{3.33}$$

As reported in [3], the minimum induced power is obtained with a uniform induced velocity v so that Eq. (3.33) provides a geometrical condition to reach the minimum induced power

$$\lambda(r) = const \implies \theta \frac{r}{R} = const, \tag{3.34}$$

hence a hyperbolic twist distribution along the radius should be achieved.
According to the MT, the incremental thrust coefficient dC_T is

$$dC_T = 4 \sqrt{\mu^2 + \lambda^2} \lambda_i r dr, \tag{3.35}$$

while in the BET the incremental thrust coefficient dC_T is

$$dC_T = \frac{\sigma C_{L\alpha}}{2}(\theta r^2 - \lambda r)dr. \tag{3.36}$$

By equating the expressions of dC_T for the two theories, an iterative process along the propeller radius can be applied to compute local quantities of interest. Starting from the first rotor station, a guess initial value for the inflow ratio is needed and the value of λ corresponding to hovering condition is usually employed. For each propeller station, the iterative procedure consists in the computation of angle of attack, aerodynamic coefficient and thrust increment based on current estimate of λ. Leveraging the equality of dC_T expression provided by MT and BET, a new value of the inflow coefficient is obtained and all the aerodynamic quantities are updated. When the difference between two successive estimate of λ is inside a predefined threshold, the values of α, dC_L, dC_D and dC_T for the current radial position are obtained. The next rotor station is considered and the same process is applied until the tip section is reached. Thrust and torque of the rotor are finally computed summing up all the contributions.

3.1.4 Propeller geometrical data

Propellers are usually characterized in term of radius and average twist. Based on these data, a preliminary estimate of thrust and power is possible; however, the implementation of BEMT requires additional details. As reported in Section 3.1.3, twist and chord distributions as well as airfoil aerodynamic characteristics have a major role for the estimation of propeller performance. Unfortunately, these data are not always available and a common solution is to define an average twist, chord and airfoil shape.

A comprehensive analysis on propeller geometrical data was performed by Brandt and Selig in [11] and [12]. The authors provided chord and twist distributions of 79 propellers used for small unmanned vehicles. Unfortunately, airfoil characteristics along the propeller radius were not given; moreover, the estimate of lift and drag coefficients were further complicated by low Reynolds effects due to a non-linear behaviour as described in Section 3.1.5.

(a) *Frontal view*
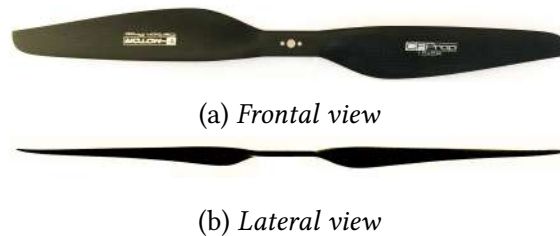
(b) *Lateral view*

Figure 3.5: T-Motor 15'x5' carbon-fibre propeller

T-Motor 15'x5' propeller

Figure 3.5 shows the frontal and lateral view of the T-Motor 15'x5'propeller, commonly used for unmanned vehicles such as the SUI Endurance multicopter. The experimental tests performed in this study are based on the T-Motor propeller as other data are available in literature [98, 99, 100]. The drawback of this propeller is its non-uniform distribution of both chord and twist along the radial direction. A 3D laser scanner reconstruction was performed by Russell in [98] and [100]. Figure 3.6 shows the geometrical distribution of chord, twist, maximum thickness and chamber based on the experimental data collected at NASA Ames. Moreover, the T-Motor propeller is characterized by a continuous varying airfoil shape (Figure 3.7). According to [98], a non-constant airfoil section is common for small scale UAS, while helicopter blades usually have one or two airfoils. The use of a continuous varying airfoil makes difficult the computation of a detailed aerodynamic database and approximations are required.

(a) *Chord and twist distribution*

(b) *Maximum camber and thickness distribution*
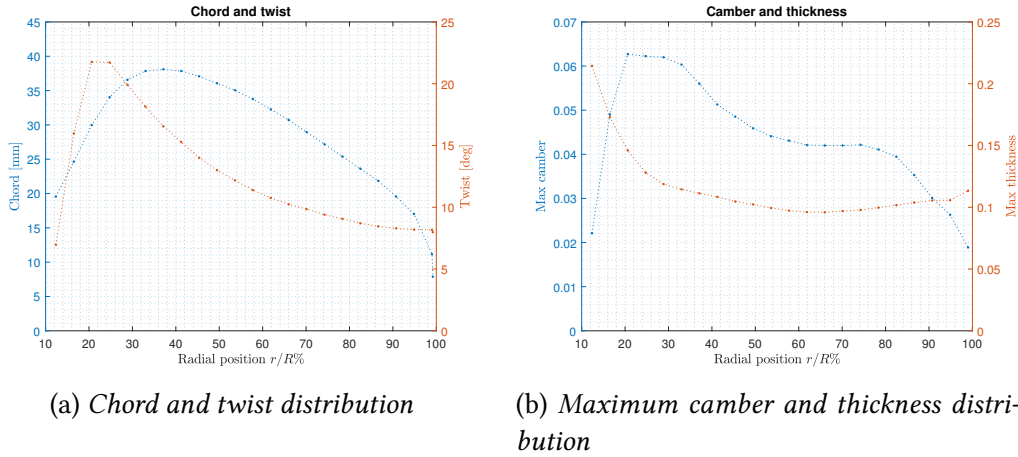
Figure 3.6: T-Motor 15'x5'geometrical distributions - chord, twist, camber and thickness

The twist angle shows a hyperbolic distribution along the radius in order to achieve a uniform inflow as suggested by Eq. (3.33) for a minimum induced drag. High twist angles are used within 25% of propeller radius, while for the remaining radial stations of the propeller a hyperbolic distribution used. The propeller hub is characterized by high thickness and small camber, the opposite for the tip station. In general, as the chord decreases, the thickness does as well [98], with the exception of the propeller tip where manufacturing limitations have a major role and the trailing edge thickness are comparable with airfoil maximum thickness.

Some important considerations on the airfoil shape along the propeller radius are possible. Firstly, with the exception of the first section, which is very close to the hub, airfoils in the range $16\% < r/R < 29\%$ look very similar in camber and get progressively thinner as the radial coordinate increase. For the mid inner sections

(30% < r/R < 49%), airfoils are reducing both thickness and camber, and the sections corresponding to 45% and 49% look practically identical. Considering the mid outer sections (49% to 74%), airfoil shapes collapse pretty well. For airfoils in the range 75% to 91%, the thickness is increasing and camber is decreasing, but the shape of the aerofoil remains similar. The trailing edge thickness also starts to increase. Finally, for the tip sections (r/R > 91%) the thickness of the trailing edge increases to maintain a minimum physical value. Moreover, the global thickness increases as well while the camber is reduced making the last section almost symmetrical. In conclusion, as a first order approximation the airfoil section located at $r/R = 0.5$ can be leveraged as most significant airfoil shape for this propeller.
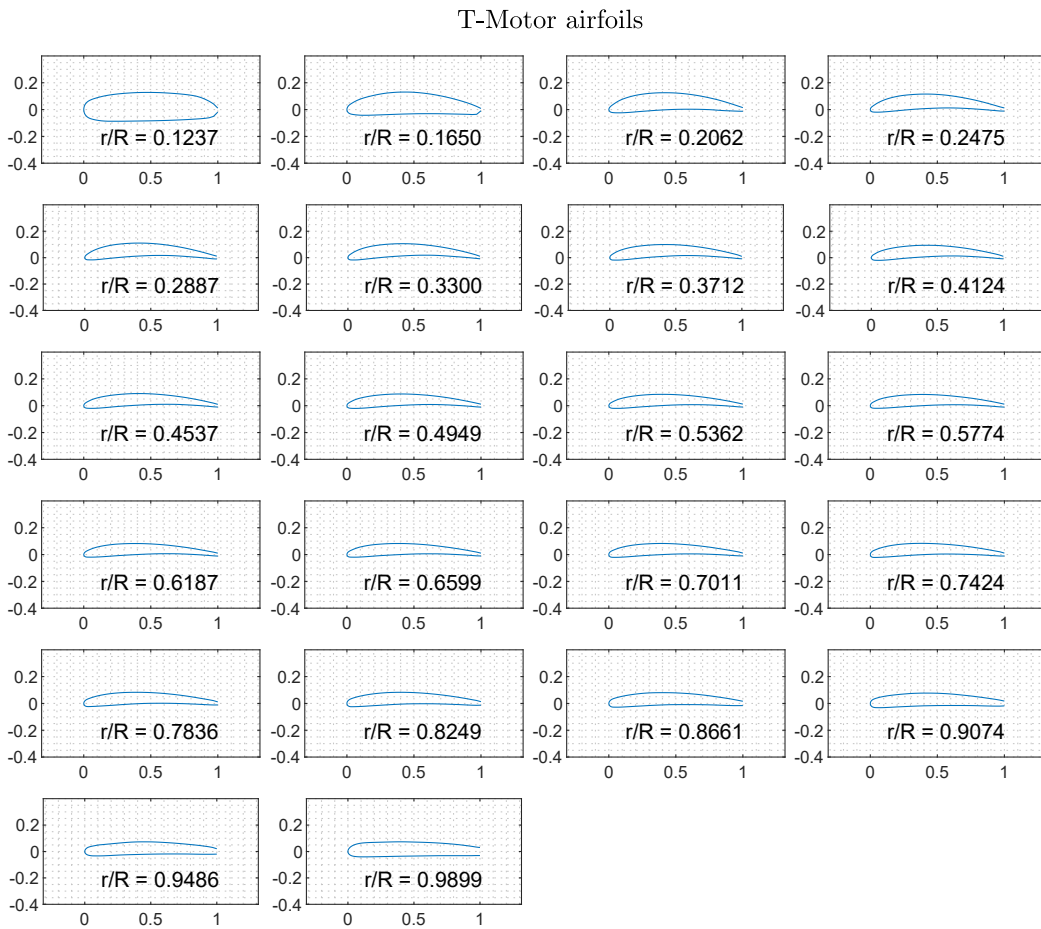
Figure 3.7: T-Motor airfoil distribution along the propeller radius

3.1.5 Low Reynolds Number Effects

BET and BEMT provide a way to evaluate propeller performance from a differential perspective compared to Momentum Theory. As reported in Eq. (3.27) and (3.29), the

blade element thrust and torque are affected by lift and drag coefficients, which in turn are functions of the angle of attack α, Reynolds and Mach numbers [2]. Moreover, if air compressibility is negligible, the sectional c_L and c_D depend only on the of angle of attack and on sectional Reynolds number defined as

$$R_e = \frac{\rho \Omega r c}{\mu},\qquad(3.37)$$

where c is the local propeller chord and μ is the air viscosity.

Small scale UAS usually cope with very low Reynolds numbers (below 100,000) so that airfoil performance and their relation to low Reynolds strongly affect the overall vehicle performance. Figure 3.9 shows lift and drag coefficients for a symmetrical airfoil (NACA 0012) based on the experimental data collected in [106]. Lift and drag trend reported in Figure shows that low Reynolds numbers are responsible for reduced maximum lift coefficient as well as early stall conditions. As a consequence, the airfoil drag coefficient increases and the overall airfoil performance are degraded.

Airfoils operating at low Reynolds numbers are be affected by *laminar separation bubble*, a region of separated flow which is responsible of airfoil performance degradation. This is a well known phenomenon occurring at Reynolds number in the range $50,000 < R_e < 200,000$ [72, 77]. The strong adverse pressure gradient is responsible for the laminar boundary layer separation from the curved airfoil surface at point S in Figure 3.8. The region bounded by the dividing streamline $S - T' - R$ and the airfoil surface is characterized by slow re-circulatory flow and forms the bubble. The flow volume between the outer edge of the boundary layer $S'' - T'' - R''$ and the dividing streamline $S - T' - R$ is subjected to turbulent transition at point T due to its high sensitivity to disturbances. The limited exchange of energy between the bubble and the outer flow results in high stability of the laminar separation bubble.
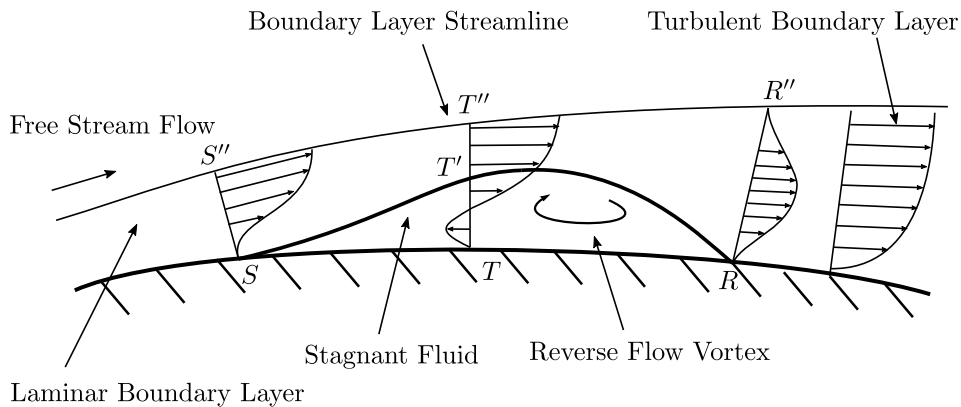
Figure 3.8: Airfoil laminar separation bubble schematization

The lower the Reynolds the higher the dimension of the bubble resulting in more deterioration of the aerodynamic performance. In particular, the Reynolds number affects

more the reattachment point compared to the separation one so that as the Reynolds decreases the bubble length increases [53].

NACA 0012 aerodynamic coefficient
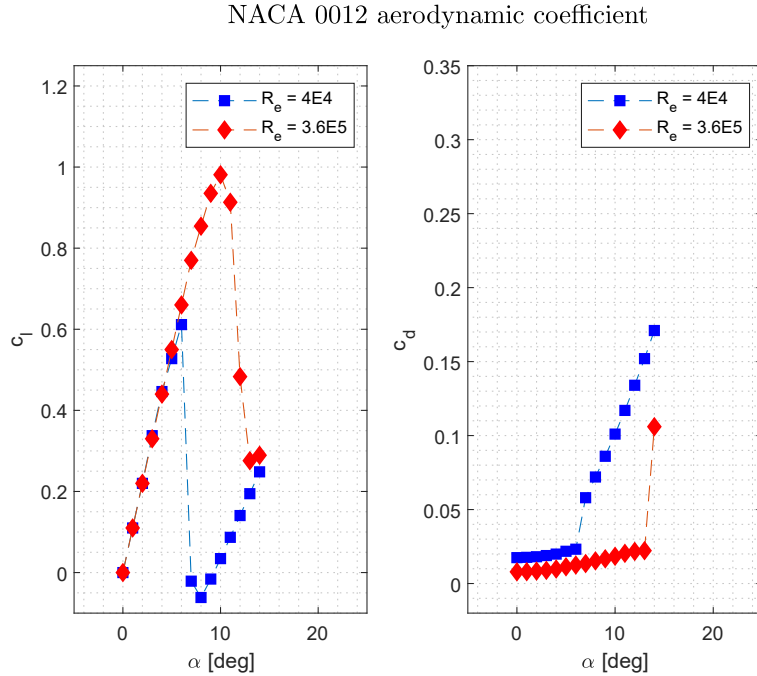
Figure 3.9: NACA 0012 lift and drag coefficients at different Reynolds numbers - data taken from [106]

The laminar separation bubble is also affected by the angle of attack and the airfoil geometry. The authors in [53] have experimentally investigated the bubble formation and highlight that as the angle of attack is increased, both separation and re-attachment point move towards the trailing edge. However, the faster moving of the separation point compared to the re-attachment causes the decrease of the bubble dimension. In addition, airfoil thickness, camber and trailing edge radius play a major role. Symmetric airfoils shows higher aerodynamic performance owing to zero camber and smaller adverse pressure gradient. Moreover, higher values of the leading edge radius are supposed to move the separation point back to the leading edge, resulting in a larger bubble.

A similar research is reported in [124], where the authors compare experimental data with Computational Fluid Dynamics (CFD) simulations. Moreover, they investigate how the airfoil geometry affects aerodynamic performance at low Reynolds. A major findings is the lower the thickness ratio, the more efficient is the airfoil. In a similar way, an increase in camber results in higher lift-to-drag ratio.

Experimental studies on propeller thrust and power coefficients were carried out by Brandt[11] and Deters [26] in order to identify the overall effect of small Reynolds numbers on propeller performance. The effect of the aerodynamic coefficients on propeller thrust and torque as can be evinced by Eq. (3.18) and (3.19). If the lift coefficient

decreases, thrust and torque will decrease; however, according to [24], the decrease in thrust will be more pronounced due to the cosine term. On the other way, if the drag coefficient increases, the propeller thrust will decrease while the torque, and hence the mechanical power, will increase resulting in degraded performance. For this reason, as the Reynolds is reduced the propeller is less efficient. The experimental measurements collected by Deters [26] in Figure 3.10 confirm the expected effect of Reynolds in thrust and power coefficients. The lower the Reynolds, the smaller the thrust coefficient owing to reduced lift decrease; furthermore, the quasi-constant power coefficient is experienced with slightly increase at lower Reynolds owing to higher values of the drag coefficient.

(a) *Thrust coefficient*   (b) *Power coefficient*
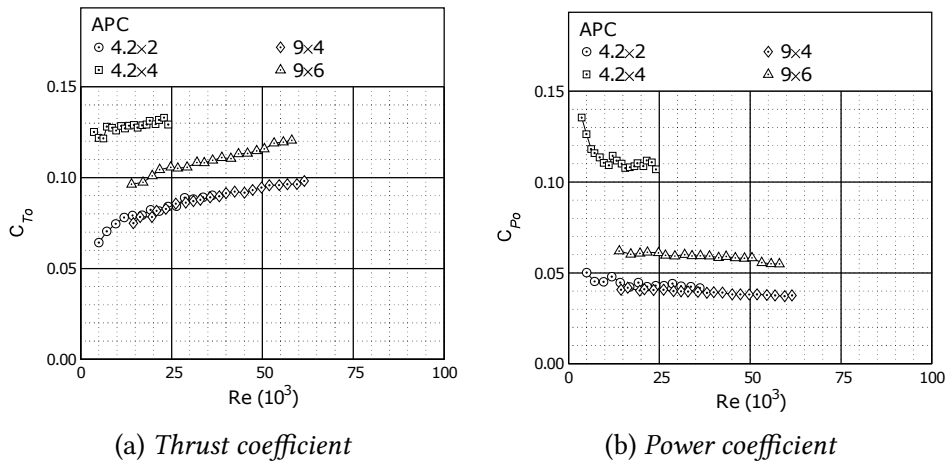
Figure 3.10: Static performance (hover) of APC propellers as a function of Reynolds number [26].

3.2   Multirotor aerodynamics

Rotor performance are the first step to evaluate the capabilities of any multicopter aircraft. However, additional considerations are required owing to the complexity of the aerodynamic field. In the case of small multirotor UAS, limited experimental studies deal with overall vehicle performance and their relation to the aerodynamics.

Zhou et al. [128] have experimentally investigated the mutual interaction between rotors for small UAS operations to highlight their effect on thrust capabilities of the vehicle. According to the authors, the relative distance between the rotor has a minor influence on the thrust coefficient c_T: as the distance between the rotor is reduced, the reduction in c_T is approximately close to 2% compared to isolated rotors. At the same time, a strongly increase in thrust fluctuations is measured as the distance between the rotor becomes smaller. Particle Image Velocimetry (PIV) analyses confirm the smaller

the distance between the rotor, the more complex the aerodynamic field resulting in thrust fluctuation increase.

The aerodynamic investigation of the full vehicle performance is important due to mutual interaction between rotors and UAS airframe, which contributes to the overall lift and drag. A comprehensive investigation on the aerodynamic performance of multirotor vehicles has been performed by NASA Ames Research Centre, as reported in Section 2.2.4. Russell et al. show that the bare airframe lift contribution is generally small compared to thrust generated by the propulsion system; furthermore, the authors highlight drag force and provide experimental data showing that the zero-pitch attitude allows to minimize this contribution. The ratio between the thrust coefficient of the full vehicle and the isolated rotor is defined as the download factor DL,

$$DL = \frac{C_{T_{vehicle}}}{C_{T_{rotor}}}. \tag{3.38}$$

Based on Russell experimental data [100], Figure 3.11 shows the download DL for a DJI Phantom 3 and a SUI Endurance UAS. The full vehicle thrust coefficient is smaller than the single rotor owing to wake interaction with bare airframes. Moreover, DJI shows smaller values of download factor as higher interaction between the rotor wakes and the vehicle arms occur. According to numerical prediction reported by [117], landing gear and battery are immersed in the 3D rotor wake resulting in a total thrust reduction of 1%. However, CFD analysis show that the airframe allows a reduction of the interaction between the rotors and as a reported in [126], four rotors generate less thrust without the airframe than with it.

The full vehicle aerodynamics is strongly affected by the propeller performance, vehicle geometry as well as flight conditions. Details on the aerodynamic field are reported for completeness considering experimental research.

3.2.1 Hover flight

The hover capability of multirotor UAS is leveraged for many applications related to monitoring, surveillance and photogrammetry. In this situation, thrust generated by the propulsion system equals the vehicle weight. As already reported in Figure 3.11, the full vehicle thrust coefficient is slightly smaller compared the isolated rotor C_T due to mutual interaction between rotors and the effect of the vehicle airframe.

A detailed investigation of a multirotor wake structure at difference distance from the rotor plane is reported in [116]. Hot-wire anemometry as well as stereoscopic Particle Image Velocimetry (PIV) were used to collect data on wake shape. Hot-wire measurements were taken at different downstream location, respectively $z/R = 1$, $z/R = 2$ and $z/R = 3$. As shown in Figure 3.12, for $z/R = 1$ the downwash from each rotor is clearly defined and limited mixing between the rotor wake occurs. For $z/R = 2$, all the rotor wakes are mixed in a single core flow; the contribution of each propeller is almost
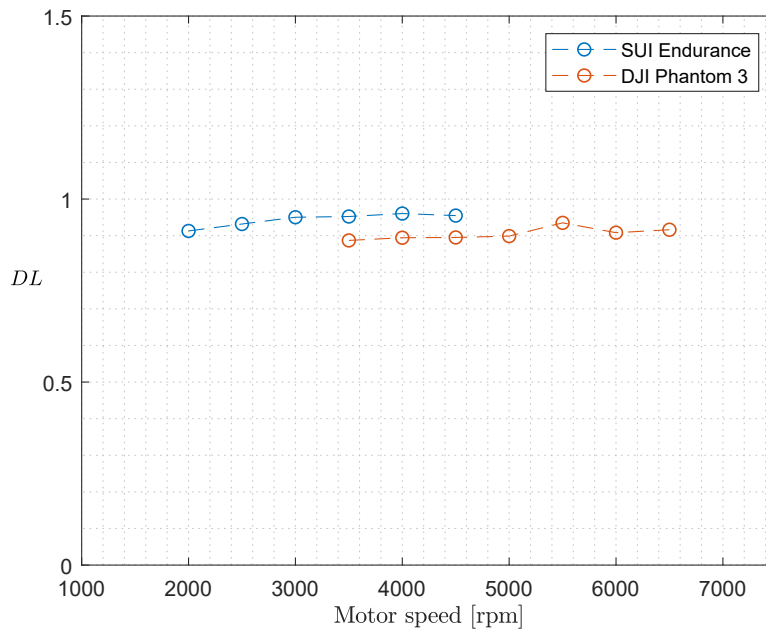
Figure 3.11: Comparison between the download factor of SUI Endurance and DJI Phantom 3

indiscernible and the flow shows a symmetric pattern. Finally, at $z/R = 3$ the multirotor wake is asymmetric and according to the authors this behaviour may be related to high turbulence intensity by vortex shedding from the UAS sting attachment.
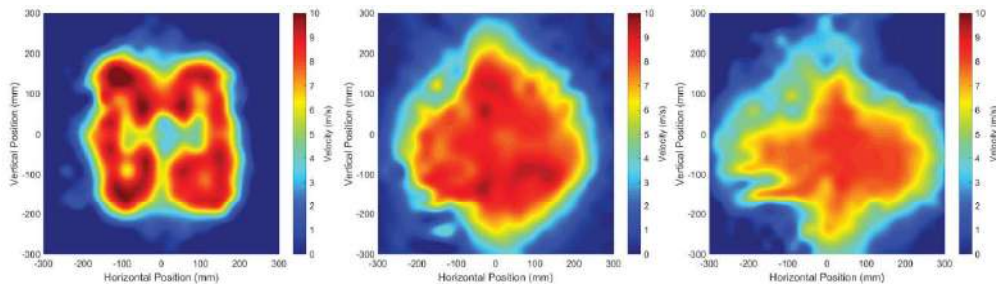
Figure 3.12: Hot-wire measurement for multirotor wake analysis in hover [116]

When considering hover flight, further discussion are required as the the UAS could experience additional non-linear effect. A comprehensive analysis of ground, ceiling and wall effects on multirotor UAS was carried out by Conyers [19, 20] and [21] at the University of Denver. When the vehicle is in ground effect, induced velocity is smaller as the flow is forced to spread radially. As the thrust is inversely proportional to the induced velocity, in ground effect, the overall thrust increase. A non linear behaviour

is shown in Figure 3.13 owing to the mutual interaction between the rotor wakes. Furthermore, the assumptions made by the classical Cheeseman and Bennet equation [16] are not valid when considering multirotor vehicles. On the other side, when the UAS experiences ceiling effect, the induced flow is reduced due to the obstructions. As a result, the pressure difference across the rotor disks increase and the vehicle is sucked up into the ceiling. However, compared to ground effect, the experimental data of ceiling effect fit better the Chesseman and Bennet formulation until z/R close to 2. For smaller z/R ratios, the estimated provided by theoretical model over-predict real conditions. The experimental activities performed by Conyers provide also insight on near-wall effect. The author states that the aerodynamic interaction between rotor wakes and the wall is responsible for a horizontal attraction force on the aircraft frame. At the same time, the vehicle experiences a pitching and rolling moments as a consequence of the attractive forces acting on the airframe.

(a) *Ground effect*   (b) *Ceiling effect*
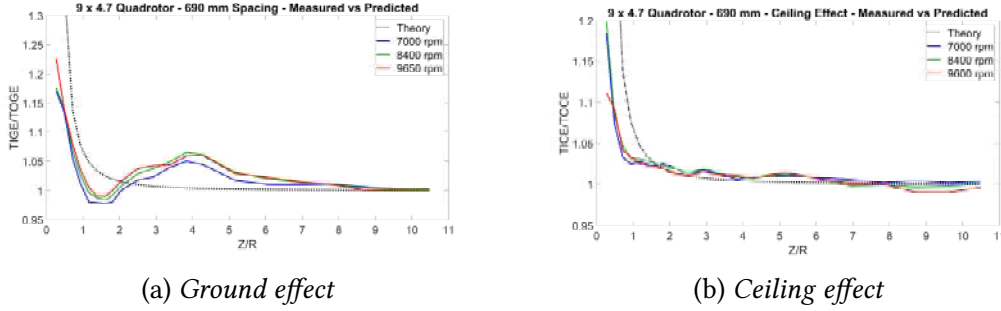
Figure 3.13: multirotor thrust non-linearities due to ground and ceiling effects [21].

3.2.2 Climb and descend

Particle Image Velocimetry (PIV) and smoke methods provide details on the structure of a multirotor wake for both climb and descend flights. In [114], the authors leverage the aforementioned methods to study a multirotor wake during climb flight conditions. The authors show that for small Reynolds numbers ($R_e \approx 4E4$), the multirotor wake during vertical climb is characterized by a recirculation zone underneath the vehicle body. Based on the flow visualization [127], as the Reynolds is increased (faster motor speeds), the interaction between the recirculation zone and each rotor wake is attenuated and a single core flow is developed.

The aerodynamic field during descending flight depends on the vertical velocity and is characterized by different flow conditions as for conventional helicopters. A schematic representation is shown in Figure 3.14. In vertical descend [10], if the upstream flow becomes large enough, some of the air will recirculate the rotors and the vehicle will experience *Vortex Ring* (VR) state. VR occurs when the rate of descend is of the same order of the induced velocity in hover flight and results in vortexes that

encircle the rotor disk causing unsteady flow ad high vibrations. As the descend rate equals the induced velocity, the vehicle experience the *Turbulent Wake* state and the rotor will act as a bluff body with limited thrust generated. Moreover, higher descend rates result in *Windmill Brake* state: in this condition, the air slows down on passing through the rotor.

(a) *Vortex Ring*   (b) *Turbulent Wake*   (c) *Windmill*
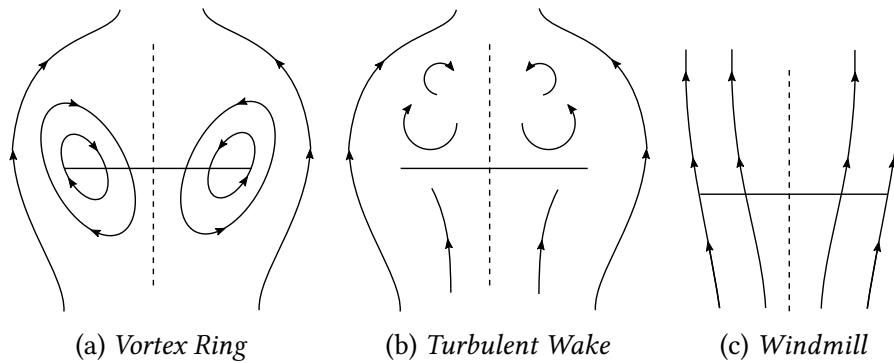
Figure 3.14: Rotor flow field in descending flight

The experimental free flight test performed in the vertical wind tunnel at NASA Langley [31] confirm VR state may occur in small multirotor vehicles. In this particular condition, the pilot workload is increased as the UAS controllability is compromised due to strong disturbances. As reported by the authors, VR state experienced by multirotor UAS results in uncontrolled pitch, roll and yaw excursion toward the overall thrust reduction.

3.2.3 Forward flight

multirotor forward flight is characterized by the interaction between the flow speed and the rotor wakes. According to [114], flow visualizations suggest a recirculating zone under vehicle body. The extent and the strength of this bubble depends on forward flight velocity.

A preliminary analysis on the effect of forward flight speed on multirotor wake structure is reported in [22]. The author performed smoke and tuft measurements to give an idea of how the UAS wake interacts with the flow field of a wind tunnel. The investigation was carried out to highlight flow recirculation inside the small wind tunnel and quantify its effect on performance test of a DJI Phantom 3. Smoke visualizations in Figure 3.15 provide a qualitative representation of the stream interaction with the UAS wake. Despite recirculating flow inside the test section, as the throttle is increased, the smoke streamline (highlighted by a red line) is deflected more sharply.

More details on multirotor wake in forward flight are reported by the experimental work carried out by Prudden et al. in [92]. The authors installed a quad-rotor UAS in the test section of a wind tunnel. The sting attachment include a 6-axes load cell
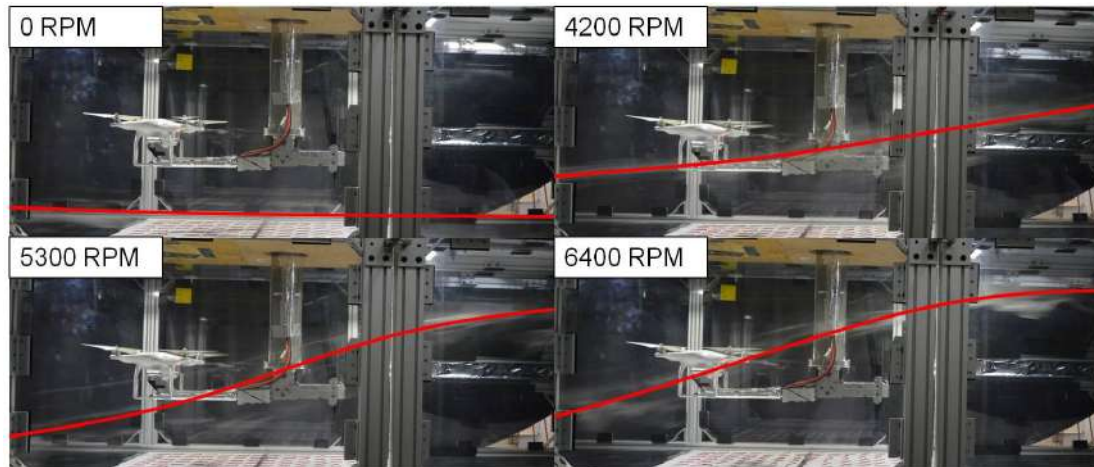
Figure 3.15: DJI Phantom 3 wake analysis in forward flight [22]

to measure forces and moments when forward flight conditions are simulated. When flying in forward flight with a pitch angle, the vehicle experiences a pitch-up moment so that additional thrust is required to the rear rotors to reach the pitch equilibrium. Moreover, as the distance between rear and front rotors increase, the differential thrust is reduced as a consequence of the increase in moment arm. The authors conclude that the upstream rotor wakes is responsible for a reduction of the downstream rotor thrust given the same power availability for both rotors.

3.3 Discussion

Mathematical tools used to describe propeller performance have been presented. Different approaches are possible: the global perspective of the Momentum Theory based on conservation laws and the differential formulation of the Blade Element Theory are combined in the Blade Element Momentum Theory, the most common algorithm implemented for numerical predictions. It is important to outline the assumptions made by these theory are not always valid when considering propellers for small scale UAS. Moreover, geometrical parameters and a high quality aerodynamic databased are needed to fill the analytical model. Most of the propellers used for commercial applications do not report these information compromising the application of numerical simulations.

Small scale multirotor UAS are characterized by propeller working at Reynolds numbers below 100,000 and non-linearities in lift-drag polars are common as a consequence of laminar separation bubble. In addition, the mutual interaction between rotors and vehicle airframe is not negligible and usually result in worsen thrust capabilities when considering the overall vehicle. Other important effects, such as ground, ceiling and

wall interferences, are responsible for non-linear thrust coefficients and power consumptions compared to results predicted by theories.

In the aforementioned context, experimental testing of multirotor UAS is still of interest, especially when unconventional flight conditions are considered. The measured data are important elements to understand the physical phenomena occurring at low Reynolds numbers and provide essential data to improve accuracy of simulation models. The novelty of this study is to investigate propeller as well as full vehicle performance systematically varying weather conditions. High quality data are collected over a wide range of Reynolds numbers, combining different temperatures and pressures. The proposed experimental setup is used to highlight the relationship between thrust coefficients and Reynolds numbers; details on motor performance while working at unconventional air atmospheres will be also discussed.

Chapter 4

Experimental Setup and Methodology

The following Chapter provides details on the experimental activity carried out inside terraXcube simulator. Section 4.1 focuses on the test stand and sensor selection. The environmental conditions simulated in the laboratory are challenging as dedicated hardware are required, especially for the low temperature and high altitude considered in this study. Details on the propulsion system for the isolated rotor tests as well as full vehicle used in this research are provided. Considering the propeller tests, commercial thrust stand are already available for medium to small propeller diameters; however, preliminary tests in terraXcube revealed unstable measurements due to the extreme temperature conditions of interest and dedicated sensors were required.

All the measurement were performed in the Large Chamber of terraXcube facility to avoid the aerodynamic interaction with the facility. Test procedures and protocols are described in Section 4.2. Best practice as well as suggestion for high quality data measurements are also highlighted in order to avoid undesired effects. The environmental conditions set in the chamber consists of a test matrix of 5 temperatures and up to 6 altitudes with extreme conditions reached for ± 40 ℃ 9000 m. Final considerations are reported in Section 4.3.

4.1   Experimental test bed

The test stand consists of a welded-steel construction with a central hollow tube and two removable end caps. The dimension of the test bed are reported in Figure 4.1: the central hollow cylinder, 130 mm in diameter and 1500 mm height, is filled with 25 kg of sand in a similar way as reported by [21], to absorb vibration energy. In addition, lateral straps are used to anchor the test stand to the floor and reduce mechanical vibrations. The upper removable end cap (Figure 4.2) is designed to house the 6-axes load cell.
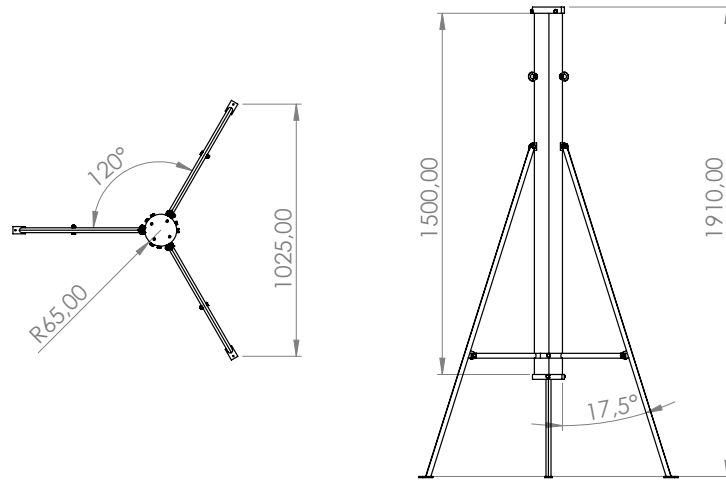
Figure 4.1: Test bed preliminary design - upper and lateral view, dimensions in millimetres

(a) *Welded-steel construction*   (b) *Upper plate for load cell installation*

Figure 4.2: Test stand for experimental testing

4.1.1   Sensors

Load cell

Force and torque (F/T) measurements are collected using the 30E15A4 sensor by JR3 [110]. This F/T device has a capacity of $(\pm 200\,N,\ \pm 200\,N,\ \pm 400\,N)$ for thrust $(F_x,\ F_y,\ F_z)$

and $\pm 16\ Nm$ for torques along all axes; note that the z-axis is aligned along the sensor vertical direction while x and y are the in-plane F/T axes. The minimum resolution of the sensor are respectively $(0.025\ N,\ 0.025\ N,\ 0.05\ N)$ for thrust and $0.002\ Nm$ for torques, with a manufacturer-stated accuracy of 0.25%. This sensor device is able to handle low temperatures (up to -40 ℃) and is equipped with a dedicated external electronics that allows to select analogue or digital measurements. While the sensor is placed inside the test section over the test stand, the JR3 electronics is installed in the control room and directly connected to the acquisition computer. All the measurement are taken in digital mode with a sampling frequency of 10 Hz (100 ms). The analogue raw data from the sensor are digitalized and decoupled by the F/T electronics; an additional low pass filter with a cut-off frequency of 0.5 Hz is set to remove noise due to mechanical vibrations.

Before testing, check loads are applied to evaluate the sensor accuracy for thrust and torque along the $z-$axis at two temperatures, $+25$℃ and -40℃ respectively. Thrust F_z calibration is accomplished considering 985, 1936 and 2936 g weights, while for torque M_z calibration, a 990 g weight is applied at 0.2, 0.3 and 0.4 m away from centre of the F/T sensor using a dedicated arm, as in Figure 4.3.

Figure 4.4a shows $z-$axis thrust behaviour for both increasing and decreasing loads. The red circle markers correspond to data measured at $+25$℃ while the blue square markers represent data at -40℃. If the load cell measurements were perfect, the measured loads would follow the black line with a slope equal to one; the resulting calibration error for the range considered is equal to $0.012\ F_z$ for both air temperatures. At the same time, the hysteresis error is 0.063 N and 0.027 N for $+25$℃ and -40℃ respectively. Figure 4.4b shows $z-$axis torque data for both increasing and decreasing loads. In this case, the calibration error is $0.018\ M_z$, while the hysteresis error is $0.02\ Nm$. As reported by Russell [99], the accuracy of this sensor is higher compare to sting balances used in wind tunnel facilities; however, the JR3 F/T device is chosen as it represent an acceptable balance between performance and cost. Moreover, the sensor capability to operate at -40℃ and the possibility to use the same F/T sensor as in [100] for a comparison suggested to select this load cell.

Tachometers

Motor speeds are measured using digital photoelectric sensors (Sick WLAP16 [107]) which sense the blade passing frequency. A reflective square-marker is placed 1.5 m over the test bed (Figure 4.5). In this way, non-intrusive measurements of the motor speed are possible without any additional probes on the propellers. The photoelectric sensors provide an impulse each time the light beam is interrupted by the blade. The blade passing frequency is converted in to motor speed by a dedicated counter module of the Data Acquisition system (DAQ). The minimum operating temperature of the WALP sensor is -40℃ wich is compatible with the temperatures expected during test sessions. The sensor frequency of commutation is 1000 Hz, one order of magnitude higher than

Figure 4.3: F/T sensor calibration with check loads

(a) Thrust calibration

(b) Torque calibration
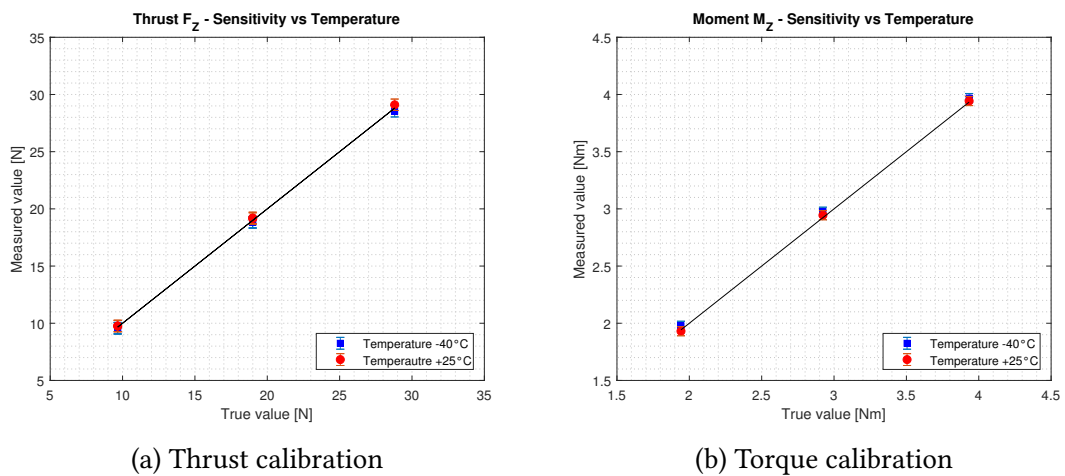
Figure 4.4: Load cell calibration

the maximum expected motor speed (250 Hz at 6000 rpm).

(a) *Propeller*   (b) *Quadrotor*
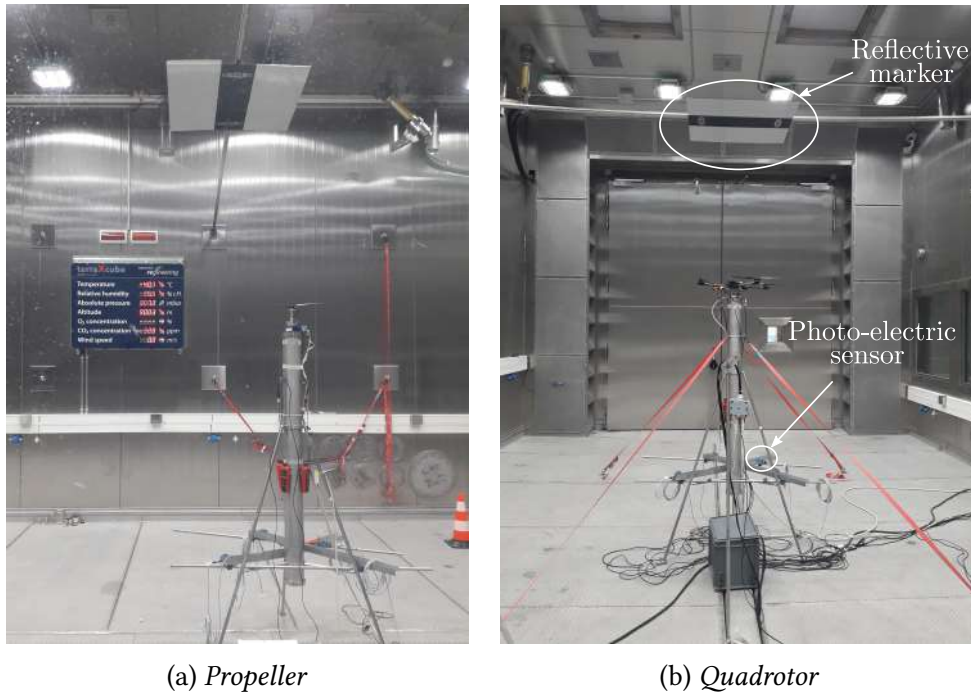
Figure 4.5: Test stand inside terraXcube laboratory

Additional sensors

The test stand is also equipped with shunt resistors to measured the electrical current
[84] of each motors installed on the UAS. The selected precision shunt resistor is char-
acterized by a resistance of 1 $m\Omega$ (50 A at 50 mV maximum) with an accuracy of 0.25%.
The operating temperature of the sensor is in the range $-40°C$ to $+60°C$ with a Temper-
ature Coefficient of Resistance (TRC) of ±15 ppm/℃, so that thermal effect on resistors
can be neglected.

Finally, the overall electrical voltage is measured using probes directly connected to
the Data Acquisition System, as the expected voltages are compatible with the values
the DAQ is able to handle.

4.1.2 Environmental sensors and auxiliary equipments

The test section of the large chamber of terraXcube simulator is equipped with sensors
to measure the environmental parameters of interest and provide feedback signals for
the atmosphere control. For the purposes of this study, additional sensors are placed
inside the test section, near the test stand, to collect temperature and pressure measure-
ments. The temperature is measured using the EE211 Eletronik sensor [30], with tem-
perature probe (PT100) characterized by a maximum accuracy of $\pm0.5°C$ at $-40°C$ and

±0.1℃at room temperature (20℃). The test section pressure is measured with the precision barometer HD9408.3B by Delta OHM [79], with an accuracy of ±0.3 hPa in the range (500 to 1200 hPa) and ±0.4hPa in the range (0 to 500 hPa).

Additional equipments include the integrated digital acquisition system Ipetronik, a rugged modular system that is able to manage at the same time excitation of the sensors as well as analogue and digital signal recording. The experimental setup is completed by a DC power supply in the control room to provide electrical power to the vehicle or isolated rotor and avoid battery charging time. The supply voltage is controlled and set to 16.8V, with a maximum output current of 70A. This solution allows to reduce transient voltage fluctuations which are common when using Li-Po batteries. As the objective of this study is the aerodynamic performance of UAS at low Reynolds numbers, thermal effects on battery are not accounted for.

4.1.3 Supplementary sensors and their limitations

To reduce testing time, preliminary attempts to measure simultaneously single rotor as well as full vehicle performance in the same test session were made. While the quadrotor UAS was mounted in the test bed previously described, a commercial test stand for UAS propeller was leveraged, as depicted in Figure 4.6. This simple test stand (RCBenchmark 1585 [96]) allows to measure thrust, torque, motor speed (electrical estimate based on phase current sensing) and electrical power. The motor torque is measured by two load cells, given the distance between them. The propeller and motor are mounted to avoid airflow interaction with the support rod (Figure 4.6). In this configuration, the load cell is compressed by the propeller thrust and the brushless motor and electronic speed controller are not inside the propeller downstream flow. This is not the conventional motor installation for UAS propulsion systems, however this configuration was preferred to reduce the aerodynamic effects, as suggested by [113]. The PWM signal to the electronic speed controller was automatically set by a computer in the control room and consist of a step sequence from 1400us up to 2000us equally subdivided in the 10 parts. Each step was made by a settling time of 3s after which a new log entry was recorded. To reduce noise, 20 samples were averaged and stored.

The main limitation of this compact thrust stand for propellers is the operating temperature as this dynamometer is designed to measure performance in standard environmental conditions. According to manufacturer, components are rated for −40℃ to 85℃ . However, experimental testing using the RCBenchmark revealed a strong influence of temperature on load cell response and current data [101]. Non-repeatable measurements were found provided the same PWM signal to the propeller under test for temperatures below 0℃. A possible cause are load cell non-linearities even though according to the manufacturer thrust and torque sensors are thermally compensated, probably not down to those temperatures. Moreover, thermal effects on precision shunt resistor might have affected electrical current data.

Initial attempts to measure motor speeds were made using the Eagle Tree brushless
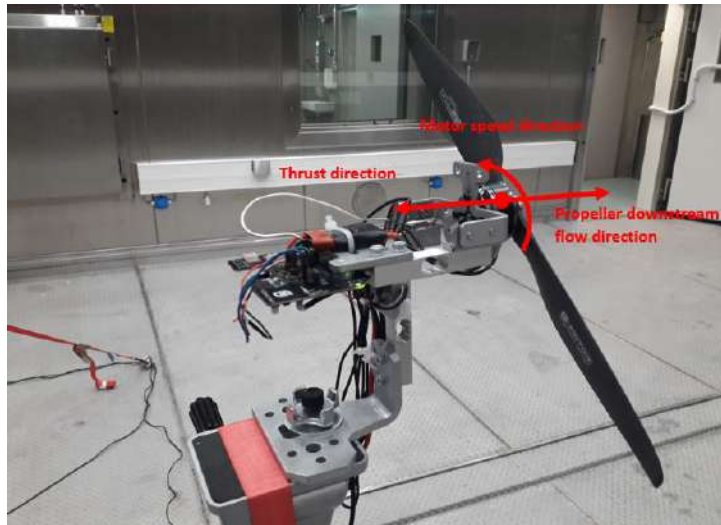
Figure 4.6: RCBenchmark 1585 thrust stand

motor RPM sensor, as made by Russell [100]. These low-cost sensors require a dedicated logger and are not designed for the extreme temperatures considered in this study; as a result, un-reliable data were provided by these sensors. Motor speed measurements were also performed using the TP0030 tachometer, based on laser reflection on a marker placed over the propeller. Unfortunately, the sensor was not able to provide stable data due to light conditions; moreover, the required distance between the light emitter and the marker on propeller was too small and unpractical for a physical installation without affecting the airflow.

For all the aforementioned reasons, propeller tests were performed using the experimental setup described in Section 4.1 (Figure 4.7), even though an additional test session was required. Stable thrust, torque as well as motor speed data were collected for the propeller in the same way as for the quadrotor vehicle.

4.1.4 Isolated rotor and full vehicle tested

The propeller and motor used for the tests are representative of small/medium scale UAS. The T-Motor 15′ x 5′ (Figure 3.5) is a carbon fibre propeller used by professional drone applications. Even tough nylon propellers are more common for hobbyists and researchers due to their low cost, the T-Motor was selected as it is possible to compare the data with experimental tests performed by Russell [100]. The electric brushless motor is the T-Motor MN3508 380KV [111] with a maximum power of 310 W. The motor is controlled by a Turnigy Push 30 A Electronic Speed Controller (ESC).

The quadrotor vehicle used for the tests (Figure 4.8) is a professional UAS with a Maximum Take-Off Weight (MTOW) of 1.7 kg and is designed for crop field monitoring with optical sensors. The four motors and propellers are mounted according the

Figure 4.7: Propeller testing - setup details

quad-X architecture and are the same used for the single propeller test. The ESC installed in this vehicle are the Flyduino KISS. Simplicity and reconfigurable design of this UAS allow a friendly interface with the test stand, with particular regard to the load cell installation. In addition, preliminary experimental studies in wind tunnel for drag coefficient estimate were performed on the same UAS [65].

As the primary objective of this work is the aerodynamic characterization of the vehicle performance in terms of thrust and power coefficients, the onboard autopilot is bypassed and installed only to supply the ESCs with the required voltage. The PWM signals to the electronic speed controllers are provided by the test engineer through the onboard transmitter connected to the Radio Control (RC). In this way, the same PWM command is provided to all the brushless motors.

It is important to highlight that the overall distance from the floor to the upper removable end cap of the test stand is 1910 mm. This value allows to minimize the influence of ground effect (GE). As reported in [21], GE is strongly related to z/R ratio, where z is the propeller disk distance from floor and R is the propeller radius. For

Figure 4.8: Q4L UAS and test stand during full vehicle test

$z/R \approx 10$, ground effect is almost negligible as $T_{IGE}/T_{OGE} \approx 1$, where T_{IGE} is Thrust-In-Ground-Effect and T_{OGE} is Thrust-Out-Ground-Effect. Considering the propeller used is $15'$ diameter, $z/R \approx 10$, which ensure negligible GE for both propeller and full vehicle, as experimentally proved in [21].

4.2 Test Methodology

In order to measure performance of isolated rotor as well as the full vehicle for different air conditions, +40 ℃, +20 ℃, 0 ℃, −20 ℃ and −40 ℃temperatures are considered; for all of these air temperature, the equivalent altitudes set in the test section are 0 m (sea level), 1500 m, 3000 m, 4500 m and 6000 m. Based on Equation (2.1), the corresponding pressure are respectively 1013 hPa, 845 hPa, 700 hPa, 577 hPa and 470 hPa. In addition, to highlight extreme low pressure effects on propeller performance, the maximum altitude of 9000 m (300 hPa) was simulated for the temperature for the hot and cold temperatures.

The test section air densities resulting from the aforementioned combinations of temperature and pressure are computed leveraging the ideal gas law

$$p = \rho R T, \qquad (4.1)$$

where p is the air pressure [Pa], ρ is the density [kg/m^3], R is the specific gas constant (287 J/kgK for the air) and T is the temperature [K]. Figure 4.9 shows the air

densities corresponding to the environmental conditions simulated. High densities correspond to low temperature and sea level conditions; the opposite for high temperature and altitudes. In total, 29 different climatic conditions were investigated for propeller testing and 25 for the quadrotor.
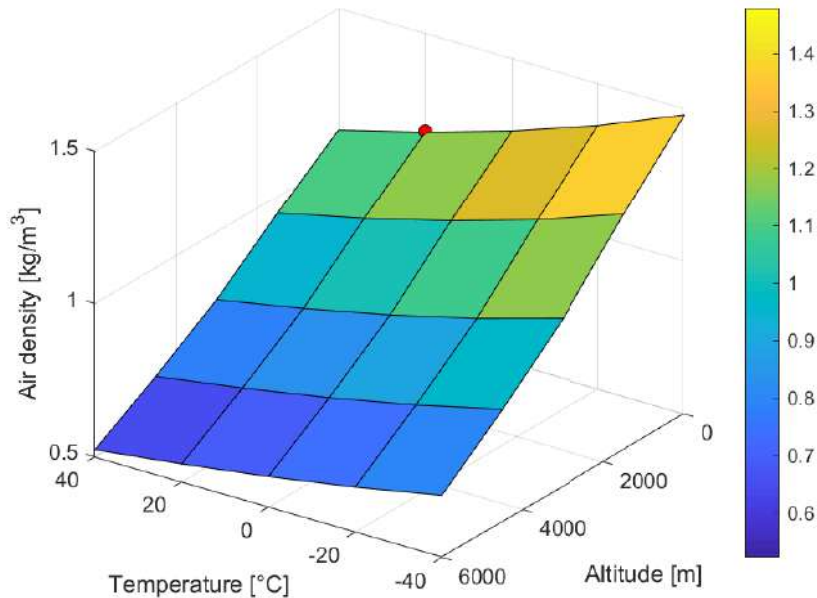
Figure 4.9: Air densities corresponding to the temperature and pressure combinations set for the tests

When setting a new temperature, all the measurements were taken after 15 min from reaching the set-point condition. This time was required for the stabilization of the load cell. To reduce testing time, the following gradients were leveraged: temperature rate of change of 30 ℃/h, altitude rate of climb/descent of 5 m/s. In general, the thermal equilibrium of terraXcube test section required a great amount of time, especially when temperature below −20℃ were set. In order to reduce testing time, first a temperature was set, than the altitudes at that temperature were investigated. This procedure allowed test section and sensors stabilization before starting data collection. Moreover, it was possible to enter inside the test section before low pressure were set and make the necessary adjustments if unexpected behaviours were experienced.

The *environmental matrix* corresponding to desired temperature and altitude combination was simulated from +40℃ to −40℃, from sea level to the maximum altitude. For both single rotor and complete UAS, a Remote Controller was used to set Pulse Width Modulation (PWM) signal to control the motor speed. Four throttle levels (50%, 66%, 80% and 100%) were set for all the tests. Each throttle level was associated to a RC switch in order to allow the repeatability of these commands. Each throttle was

sampled for 30 s for stable flow conditions.

Technical problems related to the environmental conditions were founded during the test, especially when high altitudes were set. A common issue revealed at low pressure was the behaviour of the electronic speed controllers; sometimes, one of the motor was spinning visibly slower than the others. In these cases, the ESC calibration was performed again to ensure the same motor speed was reached by the four propellers. Another common problem was the de-soldering of motor phases by the ESC connectors, probably due to *cold welding* and mechanical stress resulting from low temperatures and pressure conditions.

4.3 Final considerations

In this Chapter, the experimental setup and methodology for the tests in terraXcube were presented. A dedicated test stand was used to install the isolated propulsion system as well as the quadrotor UAS in order to collect thrust, torque, electrical current and motor speed data. The main challenge faced during sensor selection was the compatibility of the instruments with the extreme environmental conditions inside the test section. Most of the sensors used in literature for experimental testing of UAS in wind tunnels were not compatible with lo temperatures expected for the test in this study, with particular regard to the load cell and shunt resistors. Preliminary tests performed with commercial thrust stand for propellers of UAS revealed low temperatures have a strong influence on measured data and for this reason a dedicated instrumentation was required. The test stand was designed to minimize ground effect. For the propellers used in this study, the ratio z/R was set approximately equal to 10 as this distance ensure T_{IGE}/T_{OGE} close to 1.

The test consists in performance measurements for a set of temperatures and altitudes according to the environmental test matrix. To reduce testing time, different altitudes were considered while the same temperature was set. One of the main problem was related to the test section stabilization when environmental conditions were changed. When a new temperature was set, a settling time of 15 minutes was required to ensure properly acclimatisation of sensors, especially for the load cell. Technical problems related to wire de-soldering and re-calibration of ESC were common and required a dedicated inspection before performing all the measurements at constant temperature and sea level altitude in order to access inside the test section and make necessary adjustments.

Chapter 5

Experimental data analysis

In this Chapter, test results are presented for both isolated propeller and quadrotor. Section 5.1 focuses on data reduction based on the measurements collected in the tests and provides the essential definitions of the performance quantities of interest. Propeller test results is the objective of Section 5.2. Firstly, a comparison with the experimental data available in literature for the same propeller is performed to assess the overall setup. Secondly, temperature and altitude effects are investigated separately. Additional details related to motor performance are included, such as time response to throttle commands and electrical considerations at low temperature. Finally, combined effects of temperature and altitude are reported providing thrust and torque coefficients with respect to Reynolds numbers corresponding to the simulated atmospheres presented in Chapter 4. In Section 5.3, the focus is given to full vehicle performance in term of thrust and electrical power coefficients. A comparison between isolated propeller and quadrotor UAS is reported for completeness.

5.1 Data reduction

Thrust, torque, motor speed as well as electric power consumptions are the experimental data measured using the setup described in Chapter 4. To highlight the impact of air temperature and pressure on performance, all the data are processed to compute non-dimensional coefficients

$$
\begin{aligned}
c_T &= \frac{T}{1/2\rho n^2 D^4}, \\
c_Q &= \frac{T}{1/2\rho n^2 D^5},
\end{aligned}
\tag{5.1}
$$

where c_T and c_Q are respectively the thrust and torque coefficients, T and Q are the propeller/full vehicle thrust and torque, ρ is the air density and D is the propeller diameter. For the isolated rotor tests, n is the motor speed [rev/min] while for quadrotor tests, n is the average value of the four motor speeds [rev/sec].

Considering the single rotor test case, the torque required to spin the propeller and the corresponding motor speed are used to evaluate the mechanical power coefficient as

$$c_P = \frac{Q\Omega}{1/2\rho D^5 n^3}, \tag{5.2}$$

where Ω is the motor speed in [rad/s]. As reported in [67], the relationship between torque and power coefficient for the propeller is

$$c_P = 2\pi c_Q. \tag{5.3}$$

For the full vehicle tests, it is not possible to measure the torque as motor directions are coupled two-by-two and the overall resulting torque is close to zero. For the same reason, the mechanical power can't be measured and the focus will be given to the electrical power as detailed in Section 5.3.

Air temperature and pressure changes are responsible for different Reynolds number, defined as

$$R_e = \frac{\rho\Omega RL}{\mu}, \tag{5.4}$$

where R is the propeller radius, μ is the air viscosity computed based on Sutherland's model [45] and L is the characteristic length scale defined as the propeller's chord at $75\%R$ for the isolated rotor test.

5.2 Isolated Rotor

Propeller test results are reported in the following section. A comparison between the experimental data in standard conditions and those available in literature is reported in Subsection 5.2.1. Altitude effect at constant air temperature is investigated in Subsection 5.2.2 to highlight how the propeller performance are affected; on the other hand, temperature effect at sea level altitude is reported in Subsection 5.2.2. Finally, all the measured data corresponding to the simulated atmospheres (the *environmental test matrix* shown in Fig. 4.9) are discussed in Subsection 5.2.4. All the experimental data are reported in Appendix A.

5.2.1 Comparison with other experimental data

Trust and torque generated by the propeller in standard air atmosphere are compared with experimental data available in literature for the T-Motor $15'x5'$. The manufacturer propeller data-sheet as well as measurements performed by Russell [99] provide reference values. The comparison is made in term of thrust and torque coefficients in order to avoid the effect of air density. Note that torque data are not available from the

T-Motor data-sheet [111]; moreover, for these data the air density is assumed equal to 1.225 kg/m^3 as the data-sheet does not provide any information on air temperature and pressure: standard air conditions (15℃, 1013 hPa) are considered to compute the thrust coefficient from T-Motor data.

Propeller coefficient comparison is shown in Figure 5.1 where the experimental data collected in this study reveal a consistent overlap with those from NASA. Considering the thrust coefficient (Figure 5.1a), a linear trend with respect to Reynolds number is evident for data collected in terraXcube. This is in agreement with the experimental activity performed by Brandt and Selig [11, 12] as the thrust coefficient is directly proportional to Reynolds number and therefore to the angular rate of the motor. The maximum difference between our data and those measured by NASA is lower than 10%, which is acceptable considering different test stand installation and speed sensor used for the tests. On the other hand, the thrust coefficient computed from T-Motor data is slightly higher than measured data, with a decreasing trend as the Reynolds increases. The manufacturer thrust coefficient provides a preliminary reference value; however, as reported in Figure 5.1a, the actual C_T is smaller. On the other hand, the torque coefficient in Figure 5.1b is almost constant, in accordance with the expected trend investigated by Brandt and Selig. The comparison with NASA torque coefficient shows a limited offset with a percentage difference lower than 9%. In general, the highlighted differences in both thrust and torque coefficients are acceptable and may be related to different speed sensors used and test stand installations.

(a) Thrust coefficient   (b) Torque coefficient
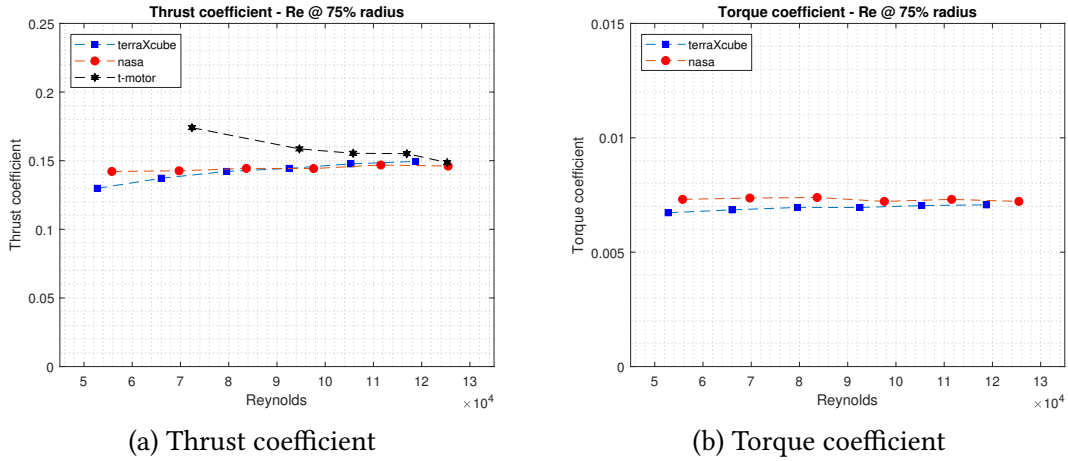
Figure 5.1: Comparison between measured propeller coefficients and data available in literature

5.2.2 Altitude effect - constant temperature

To investigate high altitude propeller performance, a constant temperature of +40℃ is set while different pressures are considered. Figure 5.2 shows the propeller thrust and

mechanical power with respect to motor speed and throttle levels, from sea level up to 9000 m. The dashed circle lines in the figure represent thrust to motor speed curve, which shows a parabolic trend as expected from theory. Each circle corresponds to a throttle level as reported in the arrow text box. In addition, the square-marked line labelled as *Hover* represents a reference thrust level equal to 4.5 N, which is approximately the thrust required by each motor to hover the full vehicle. It can be noticed that as the altitude is increased, the required motor speed to achieve the reference thrust value increases as well. In the most extreme case, 9000 m altitude, the increase in speed is up to 74% compared to sea level with propeller thrust close to the maximum value the rotor is able to generate at 100% throttle for this altitude. The higher the altitude the higher the throttle level for the desired thrust. On the other hand, a reference motor speed will result in a reduced thrust generated by the propeller when different altitudes are set.
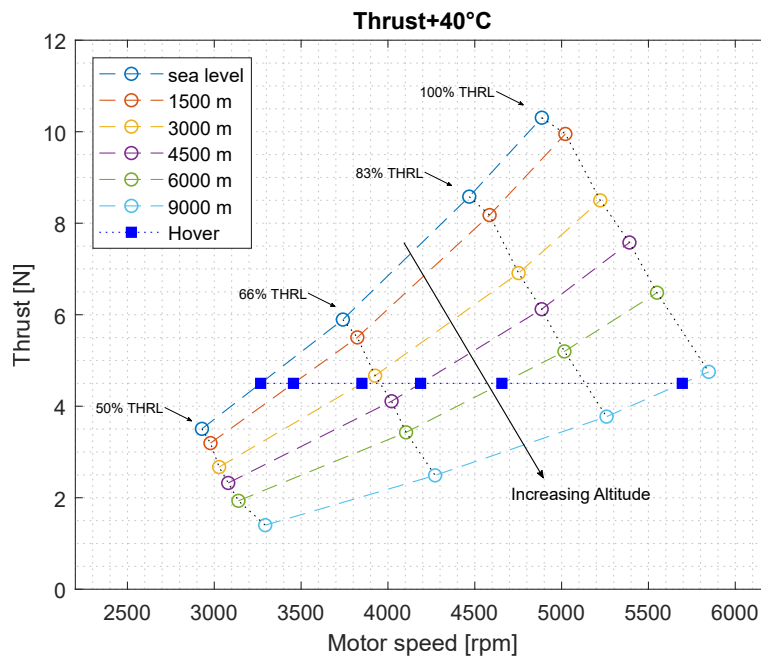
Figure 5.2: Propeller thrust - altitude effect, +40℃ constant temperature

Similar considerations are made for the mechanical power of the motor shown in Figure 5.3a. As the altitude increases, the mechanical power required to achieve a reference thrust (square marks in the figure) increases too. This is a direct consequence of the higher motor speed needed for the same thrust. At the same time, the mechanical power generated by the motor at constant throttle condition (i.e. full throttle) decreases as higher altitudes are set meaning that the air density reduction prevails over motor speed increase. The same behaviour is experienced by the electrical current absorbed by the motor in Figure 5.3b.

(a) Mechanical power

(b) Electrical current
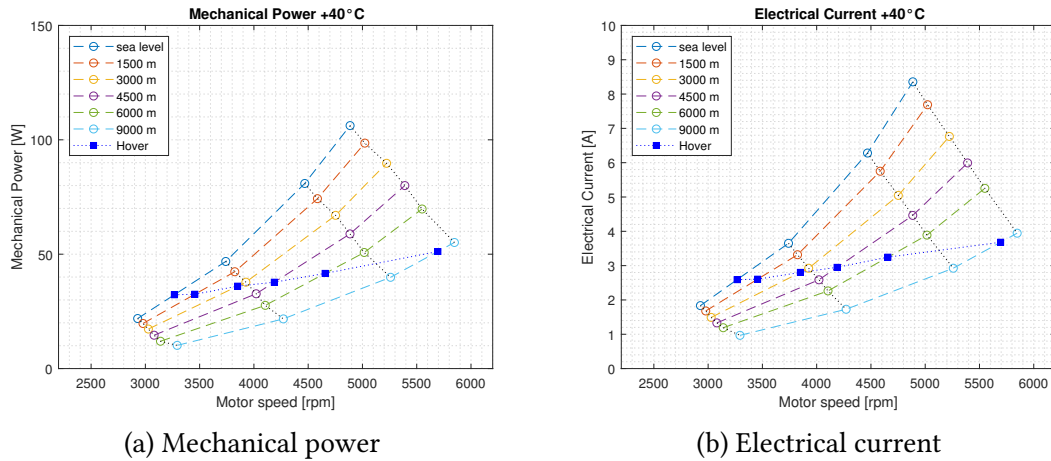
Figure 5.3: Mehcanical power and electrical current - altitude effect, +40℃constant temperature

Thrust and torque coefficient as a function of Reynolds number are shown in Figure 5.4 for all the altitudes and throttle levels considered at +40℃ air temperature. Low Reynolds represent high altitude and low throttle conditions, the opposite for high Reynolds numbers. The experimental data are represented by blue circle marker while dotted red lines are interpolations. The thrust coefficient in Figure 5.4a shows a linear trend as the Reynolds increases while the torque coefficient is almost constant. These results are in accordance with the experimental trend measured by Brandtl, Selig and Deters [11, 12, 25, 26]. As the altitude increases, the corresponding reduction in air density is responsible for lower Reynolds number. The lower the Reynolds, the less the local airfoil lift coefficient and the higher airfoil drag coefficient. The overall result is a reduction of the propeller C_T while constant C_Q and C_P are experienced.

For completeness, a transient altitude condition from 7000 m to sea level (rate of descent 5 m/s) at constant temperature (−40℃) is included. The data are collected setting the propeller throttle to 50%. As previously highlighted, high altitude results in fast motor speed but reduced propeller thrust, as shown in Figure 5.5a. Compared to sea level condition, the motor speed increase is 7.3% while thrust reduction is closed to 55%. As a result, motor speed increase does not compensate air density decrease as a consequence of high altitude. Similar considerations are made for propeller torque which is reduced of 53% at 7000 m. The mechanical power decrease (−47% with respect to sea level) is smaller compared to thrust and torque due to motor speed increase at high altitude. Thrust and torque coefficients in Figure 5.6 confirm the trend reported previously discussed, with a linear relationship between C_T and Reynolds number and a constant torque coefficient.

The experimental data collected during the tests allow further considerations. In
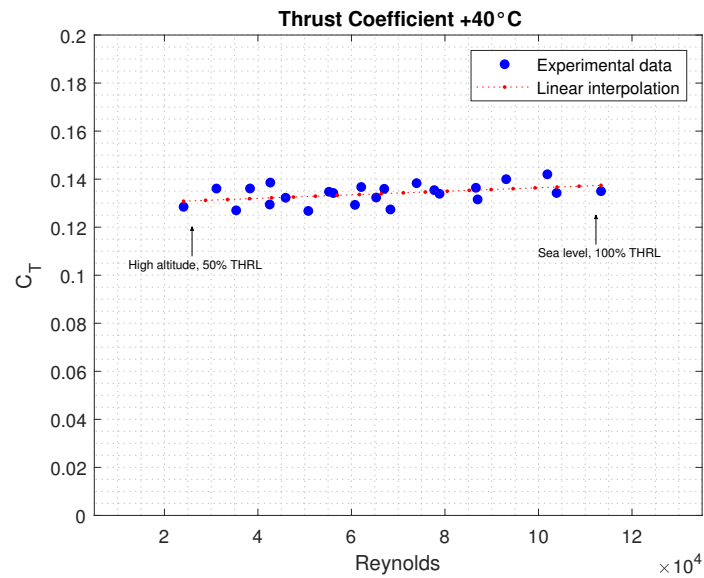
(a) Thrust coefficient
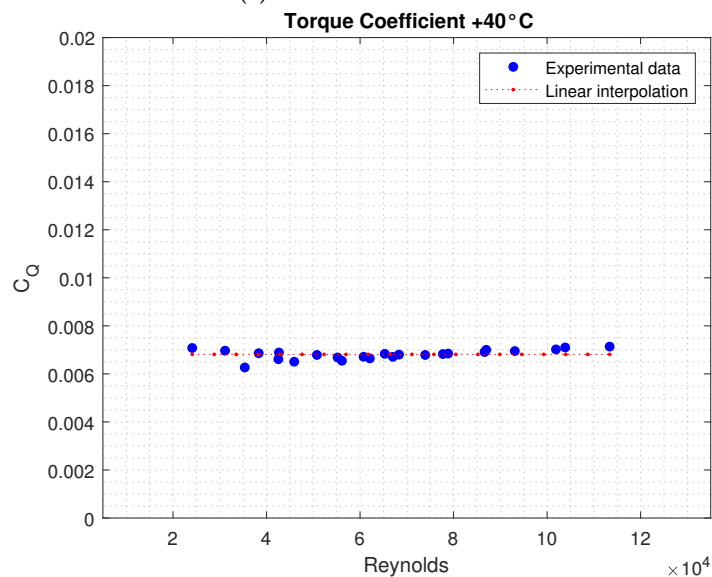
(b) Torque coefficient

Figure 5.4: Trust and torque coefficients with respect to Reynolds number - altitude effect, +40℃ constant temperature

particular, during the tests at constant temperature it was noticed that when high altitudes were set the motor response to throttle commands took longer time. To investigate how low pressure conditions affect motor speed, the mechanical time constant in response to throttle command is considered. To evaluate the mechanical time constant, the motor angular rate time history is used. First, the time T required by the motor in response to a step down from 100% to 0% throttle is evaluated for each altitude. Secondly,

(a) Thrust and motor speed

(b) Torque and mechanical power
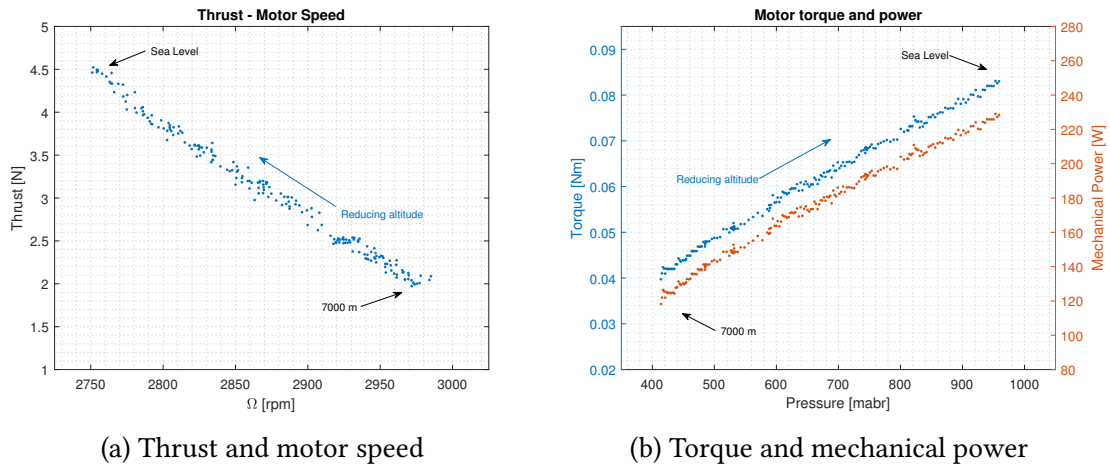
Figure 5.5: Effect of altitude descent from 7000 m to sea level - constant temperature (−40℃) and thottle (50%)on propeller performance
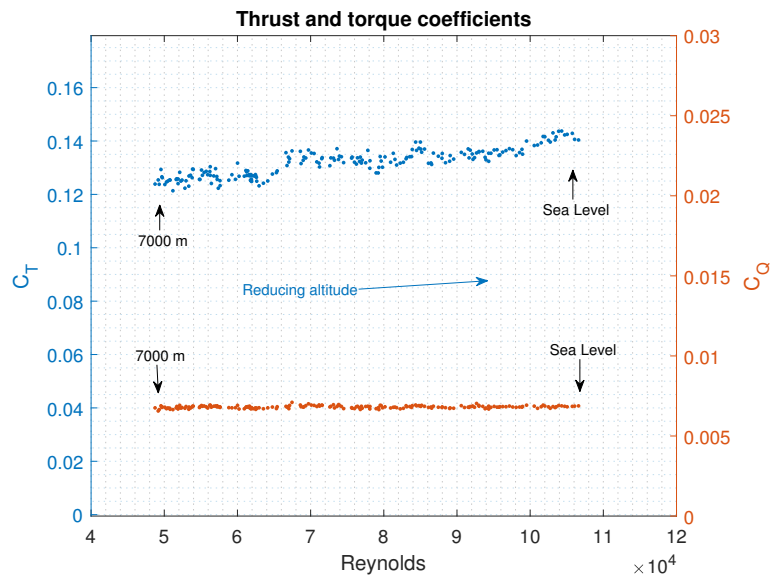
Figure 5.6: Effect of altitude descent on thrust and torque coefficients

the time constant τ is computed as the time required by the motor speed to reduce up to 63% of the initial value, approximately one fifth the total time T. A typical motor speed time history is reported in Figure 5.7a; Figure 5.7b shows the mechanical time constant as a function of altitude for a reference temperature of +40℃. The higher the altitude, the longer the time constant. The experimental trend of τ with respect to the altitude is validated by analytical considerations. The dynamic equilibrium governing the motor speed transient is given by the differential equation

$$J\dot{\Omega} + \frac{1}{2}\rho C_Q D^5 \Omega^2 = 0$$
$$\Omega(t_0) = \Omega_0$$

(5.5)

where J is the propeller and motor inertia, Ω is the motor angular rate, ρ is the air density, D is the propeller diameter, C_Q is the torque coefficient and Ω_0 is the initial motor speed. Eq. 5.5 is a Cauchy problem that leads to the solution

$$\Omega(t) = \frac{\Omega_0}{1 + \frac{1}{2}\frac{\rho C_Q D^5 \Omega_0 t}{J}}$$

(5.6)

where it is possible to define the time constant

$$\tau = \frac{2J}{D^5 C_Q \rho \Omega_0}.$$

(5.7)

Finally, Eq. 5.7 shows the motor speed time constant is inversely proportional to air density: considering constant air temperature conditions, the lower the pressure the smaller the density and the greater the time constant τ. At high altitude, the propeller response to throttle command is less reactive, requiring longer time to reach the desired motor speed.

5.2.3 Temperature effect - constant altitude

Temperature effects are investigated at constant altitude; Figure 5.8 shows propeller thrust for all the temperatures considering a reference altitude of 1500 m. The circle-dashed curves are thrust-motor speed curve for different air temperatures while the blue square-marked line labelled as $Hover$ represents a reference thrust level equal to 4.5 N. The reference thrust suggests air temperature decrease is responsible for motor speed reduction. In the same way, mechanical power and electrical current (Figure 5.9) are lowered (for the the hover thrust) when cold temperatures are set as a result of motor speed reduction.

Considering constant motor speed conditions, thrust generated by the propeller increases as lower temperatures are set. This is a direct consequence of air density changes (increase) considering a constant pressure as stated by Eq. 4.1. On the other hand, for constant throttle condition (i.g. full throttle), the lower the temperature the higher the propeller thrust and power while a small reduction in motor speed is experienced. As the temperature is lowered, the air density increase prevails over the motor speed reduction.

Thrust and torque coefficient as a function of Reynolds number are shown in Figure 5.10 for all the temperatures and throttle levels. Low Reynolds represent high temperature and low throttle conditions, the opposite for high Reynolds numbers. The experimental data are represented by blue circle marker while dotted red lines are polynomial
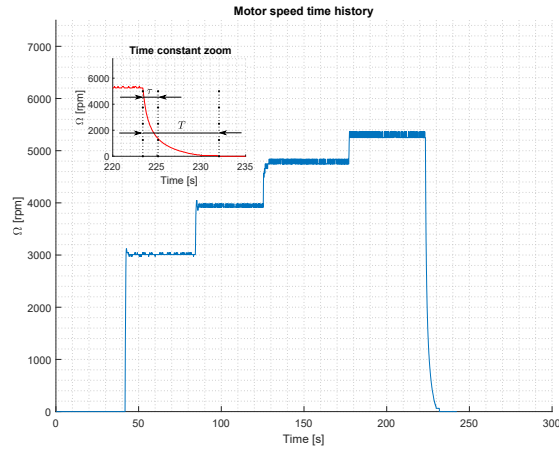
(a) Typical motor speed time history
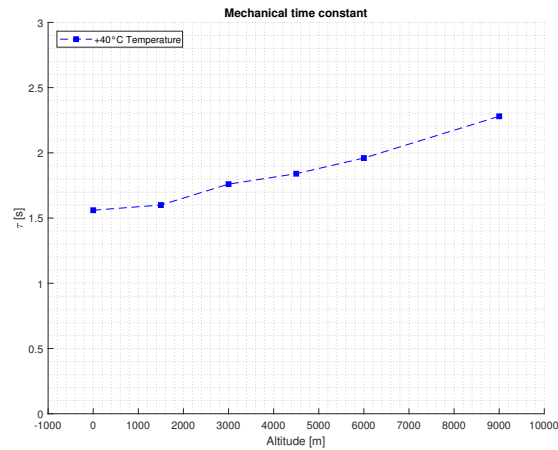
(b) Mechanical time constant as a function of altitude

Figure 5.7: Altitude effect on motor speed time constant τ, +40℃ air temperature

interpolations. As for altitude tests, the thrust coefficient in Figure 5.10a shows a linear trend as the Reynolds increases while the torque coefficient is almost constant.

The air temperature is responsible for different motor performance. Firs of all, the motor and electronic speed controller resistances are directly affected by air temperature. Direct measurement of motor winding resistance for UAS propulsion system is difficult as dedicated instruments are required to collected small values, $m\Omega$ order of magnitude. Further more, limited data are available from manufacturer' data-sheets. For the T-Motor MN3508 brushless motor used during the tests, a reference value of 205 $m\Omega$ is reported in the technical description of the motor; however, this value refers to a single phase resistance without any details on temperature conditions and related
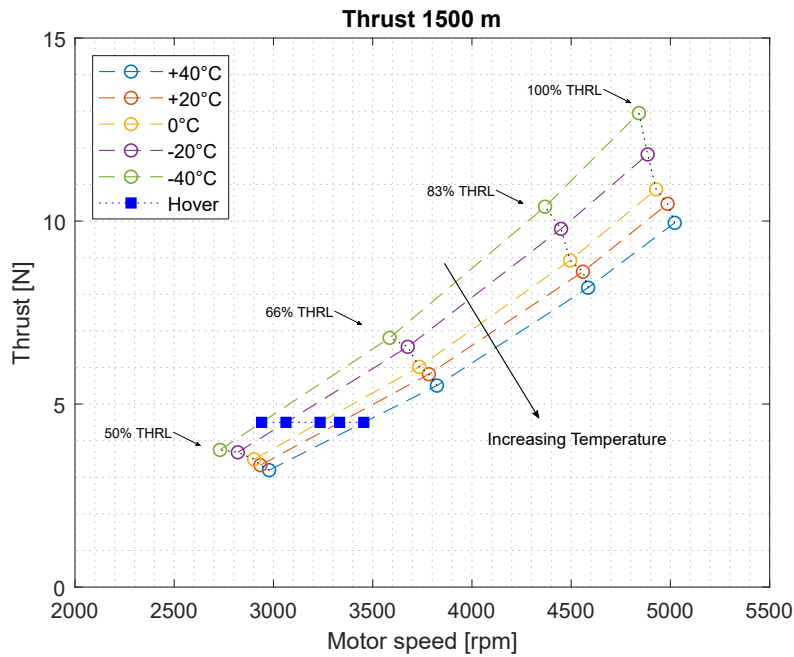
Figure 5.8: Propeller thrust - temperature effect, 1500 m constant altitude

(a) Mechanical power

(b) Electrical current
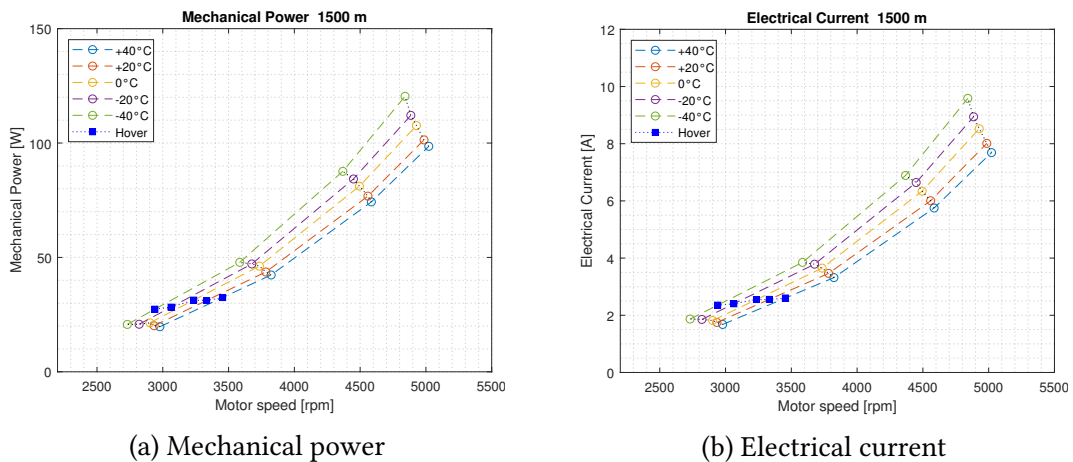
Figure 5.9: Mehcanical power and electrical current - temperature effect, 1500 m constant altitude

ESC resistance. It is possible to estimate the propulsion system resistance (motor windings and ESC) based on the electrical and mechanical power measured during the tests. To avoid undesired effects related to the Pulse Width Modulation ESC, the experimental data are collected setting different power supply voltages (8.4 V, 11.2 V, 14 V and 16.8 V) in full throttle conditions. The overall propulsion system architecture is reported in Figure 5.11a , while a simplified equivalent electrical circuit [40] is in Figure 5.11b.
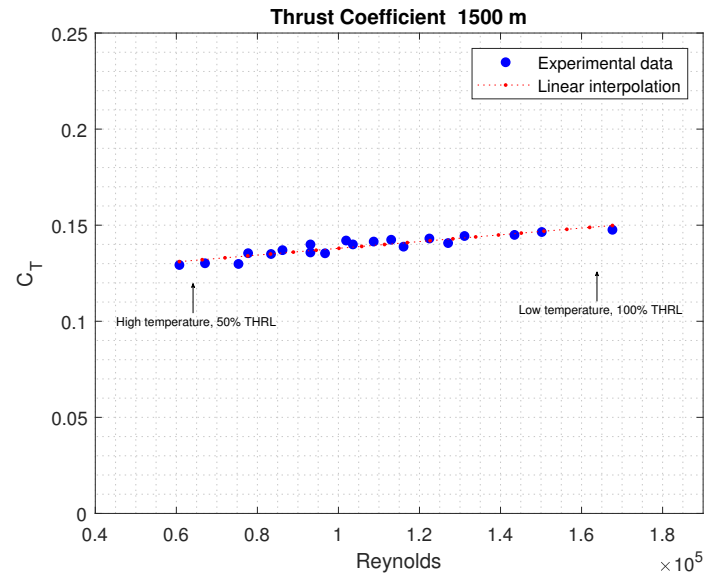
(a) Thrust coefficient
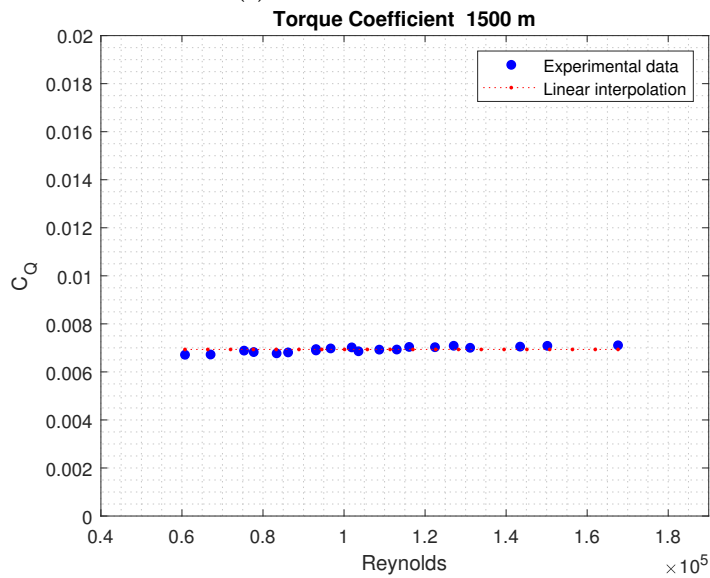
(b) Torque coefficient

Figure 5.10: Trust and torque coefficients with respect to Reynolds number - temperature effect, 1500 m constant altitude

Mechanical and electrical power required by the motor are computed as

$$P_M = Q\Omega$$
$$P_E = Vi \tag{5.8}$$

(a) BLDC motor schematization

(b) Simplified electrical circuit
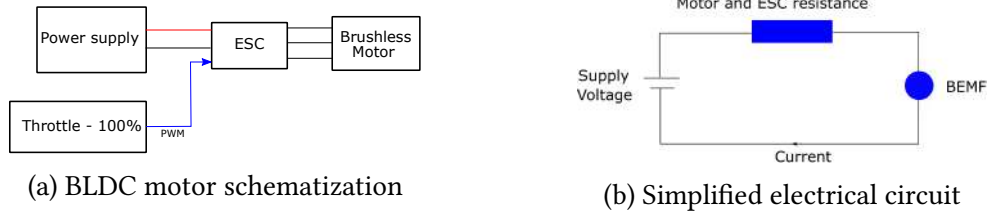
Figure 5.11: Brushless motor for UAS applications

where Q is the motor torque, Ω the speed, V is the supply voltage and i is the electrical current. The difference between electrical and mechanical power is the amount of power dissipated by Joule effect. The motor and ESC resistance R_{tot} is give by the following Equation:

$$R_{tot} = \frac{P_E - P_M}{i^2}. \tag{5.9}$$

The resistor changes with respect to air temperature is linear [103] so that the colder the environment the lower the motor and ESC resistance. The experimental data estimated in Figure 5.12 confirms the expected behaviour showing a 15% reduction at $-40°$ compared to ambient temperature.
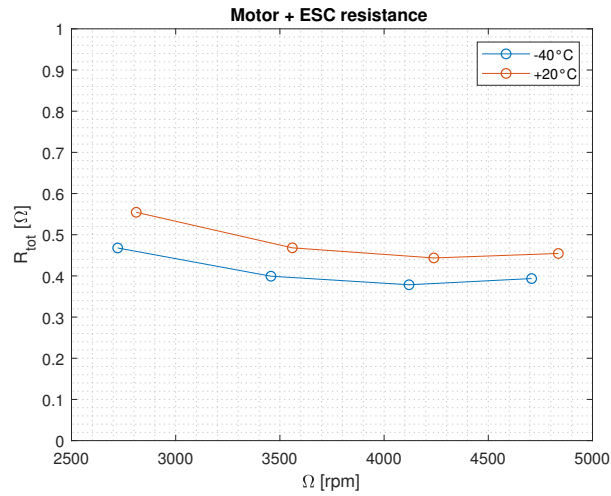
Figure 5.12: Temperature effect on motor and ESC resistance

Temperature is responsible also for no load current changes. This is the electrical current required to spin the motor without any loads applied to its shaft. It provides an estimate of the bearing friction power loss and viscous drag due to rotor spinning in the air. As the motor speed increases, the no load current grows up because the power required to spin the motor due to bearing friction and viscous drag increase as well. To evaluate the no load current, the propeller is removed and different throttles are set

to the ESC. The experimental data in Figure 5.13a confirm the expected behaviours, where the no load current is given with respect to the motor speed. In addition, it can be noted that a low temperature results in increased no-load current, suggesting higher friction power loss are experience by the motor. The higher the no load current, the less efficient is the propulsion system as more power is dissipated during the electrical to mechanical conversion. Finally, temperature effect on motor efficiency is in Figure 5.13b. Low ambient temperature results in degraded motor efficiency as a result of increased no load current.

(a) No load current
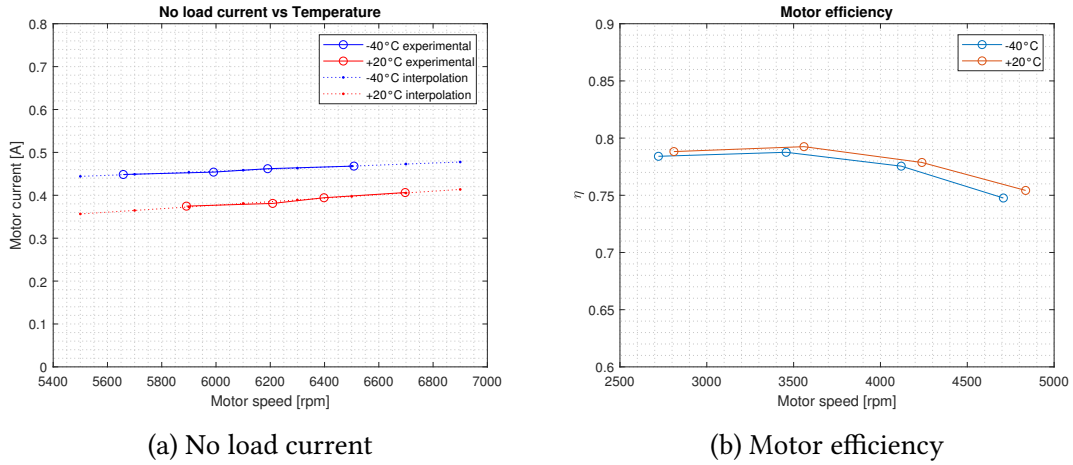
(b) Motor efficiency

Figure 5.13: Temperature effect on no load current and motor efficiency

5.2.4 Complete matrix

In previous paragraphs, the effect of temperature and altitude were presented separately. In the followings, temperature and altitude combinations (the simulated atmospheres in Figure 4.9) are reported for the isolated rotor tests.

Figure 5.14 shows thrust and torque generated by the propeller for all the atmospheres of interests. Each surface corresponds to a different throttles and while red circles highlight thrust and torque in standard air condition (+20℃, sea level). The corresponding thrust coefficients are in Figure 5.15. The experimental data are represented by blue circles, a linear interpolation is given by the red dotted line while the black square marker is the C_T value corresponding to standard air condition. The experimental data confirms a linear relationship between thrust coefficient and Reynolds number, in accordance with data in literature. The resulting linear interpolation, based on least square method, is

$$C_T = C_{T_0} + k R_e \tag{5.10}$$

where $C_{T_0} = 0.1172$ and $k = 186.4E - 9$. Compared to standard air atmospheres, the maximum C_T increment is 8.1% at the highest Reynolds number while a reduction of 12.7% occurs at the lowest Reynolds. On the other hand, torque and power coefficients are not affected by the Reynolds, as depicted in Figure 5.16. For this reason, a zero order interpolation is adopted for the torque coefficient

$$C_Q = C_{Q_0}, \tag{5.11}$$

where $C_{Q_0} = 6.864E - 3$.

(a) Thrust   (b) Torque
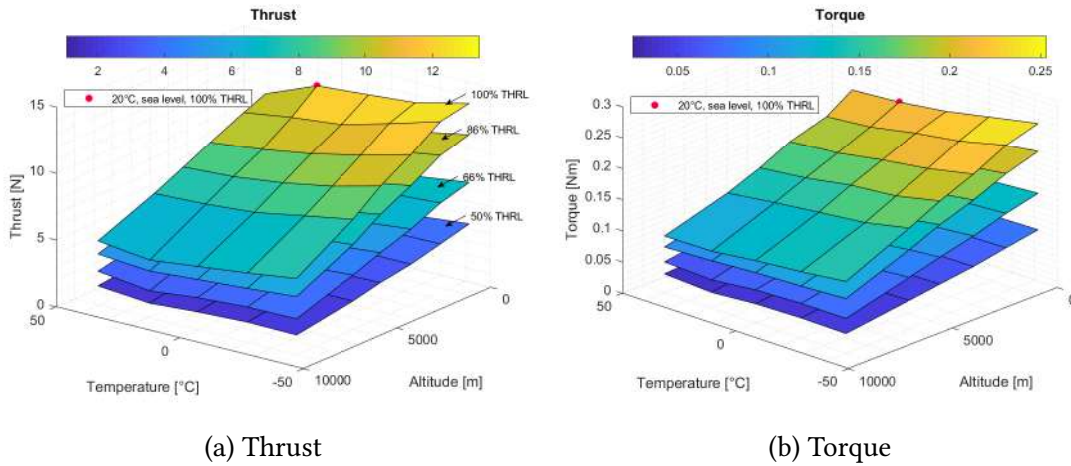
Figure 5.14: Propeller thrust and torque for all the simulated atmospheres

The combined effect of air temperature and altitude on motor speed time constant is presented in Figure 5.17. As suggested by Eq. 5.7, the mechanical time constant is strictly related to the air density. In particular, as the temperature is decreased at constant altitude the time constant τ is shortened so that the propeller response to a throttle command is faster; the opposite for high temperatures.

5.3 Full vehicle

Temperature and altitude effects on quadrotor performance are the same as for the isolated propeller as the physical phenomenon governing the aerodynamics of low Reynolds number is once again the *laminar separation bubble*. In the following Section, full vehicle performance are presented in term of thrust coefficient. Moreover, a comparison between the isolated propeller and quadrotor C_T is discussed. All the experimental data are reported in Appendix B.
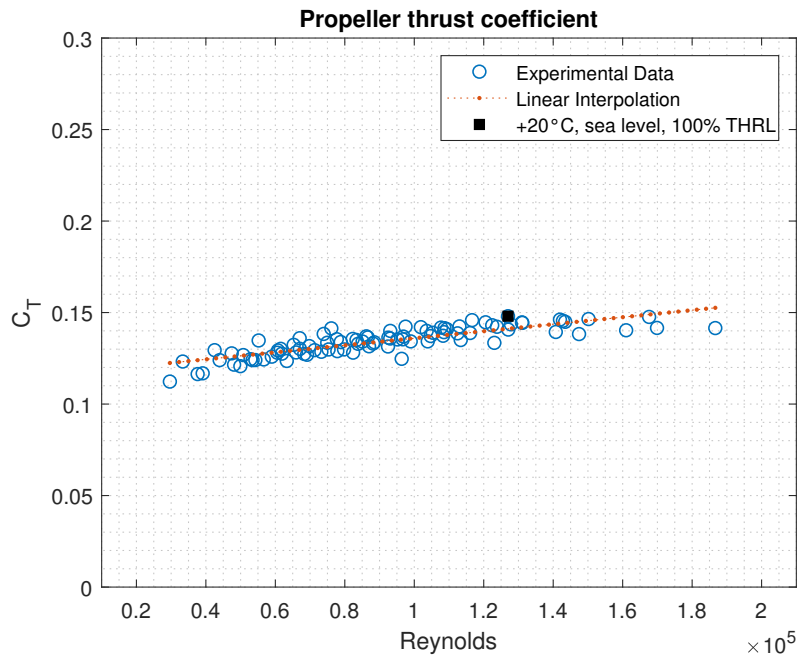
Figure 5.15: Propeller thrust coefficient
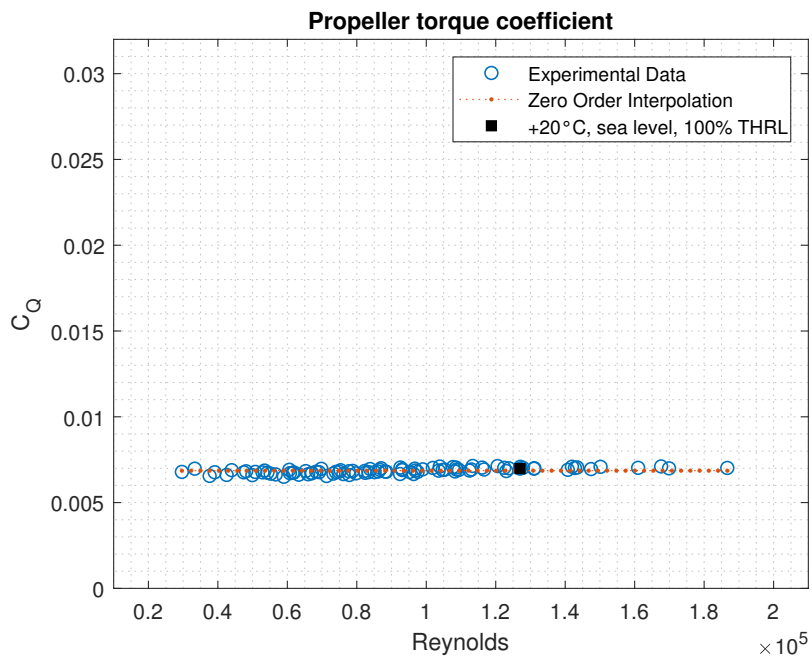
Figure 5.16: Propeller torque coefficient
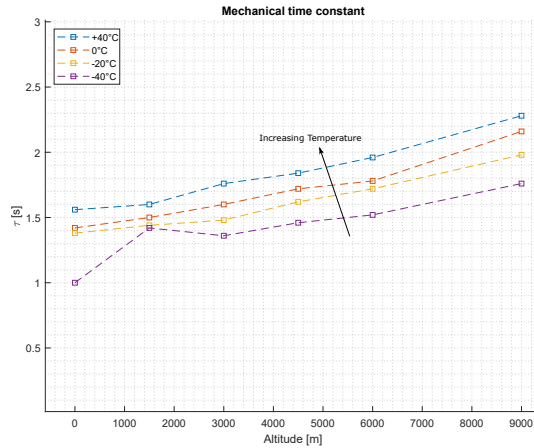
Figure 5.17: Temperature and altitude effects on motor speed time constant

5.3.1 Complete matrix

The quadrotor thrust coefficient is reported in Figure 5.18a for all the simulated atmospheres. The circle markers represent experimental data, the dotted line is a linear interpolation and the black square marker represent C_T for a reference test condition of +20℃ sea level 3400 rpm test. The maximum altitude considered for the full vehicle test is limited to 6000 m as undesired effects occurred during the experimental session, such as motor winding de-soldering and unexpected electronic speed controller response to throttle commands.

(a) Thrust coefficient

(b) Electric power coefficient
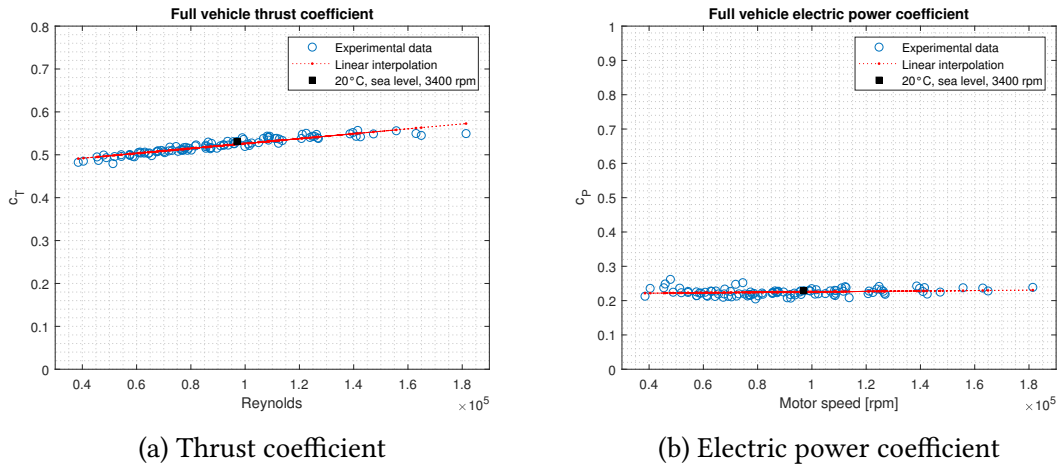
Figure 5.18: Quadrotor performance coefficients and Reynolds number

As for propeller tests, the full vehicle C_T shows a linear trend with respect to Reynolds, with lower values corresponding to high altitude and temperature as well as low throttle levels. With respect to the reference condition, high Reynolds numbers result in

thrust coefficient increase up to 8%; similar percent values are experienced for C_T reduction when considering low Reynolds. Thrust coefficient interpolation with respect to Reynolds number is given by the following Equation

$$C_T(R_e) = C_{T0} + kR_e, \tag{5.12}$$

where C_{T0} is 0.469 and k is equal to $5.7174E - 7$.

For the full vehicle tests, the torque measured by the load cell sensor is closed to zero as the motors are installed two by two in opposite spin directions (clockwise and counter-clockwise). For the same reason, it is not possible to evaluate the mechanical power required by the vehicle and the power coefficient C_{P_E} is computed considering the electrical power required by the motor

$$C_{P_E} = \frac{VI}{1/2\rho D^5 n^3}, \tag{5.13}$$

where V is the supply voltage and I the total electrical current absorbed by the four motors. Compared to the power coefficient in Eq.5.2 which focuses on the mechanical power required to spin the motor, the C_{P_E} coefficient includes additional effects related to motor and ESC efficiency. However, C_{P_E} represents a global quantities which summarizes vehicle performance from the overall system point of view. The electrical power coefficient in Figure 5.18b, computed from experimental data, fit a flat curve suggesting the Reynolds number has a limited influence on C_{P_E} (similar results were found for propeller C_P). In conclusion, the electrical power is directly proportional to the product between air density and cube of motor speed ($VI \propto \rho n^3$).

5.3.2   Propeller and quadrotor comparison

Figure 5.19a shows the comparison between propeller and full vehicle thrust coefficient, where the green square marker are the isolated rotor $C_{T_{prop}}$, the red star markers represent full vehicle data $C_{T_{UAS}}$ and the blue circles are four times the isolated propeller thrust coefficient. This figure suggests the UAS thrust coefficient is smaller compared to the isolated rotor C_T owing to aerodynamic interface between multiple rotors and airflow interaction with the vehicle arm as well as airframe. The comparison between propeller and quadrotor thrust coefficient is based on the download factor DL [99] defined as

$$DL = \frac{4C_{T_{prop}} - C_{T_{UAS}}}{4C_{T_{prop}}}, \tag{5.14}$$

and Figure 5.19b shows the DL as a function of Reynolds number. The experimental data from vehicle and single rotor result in a decreasing DL with increasing Reynolds, with an average value closed to 3.5% and a maximum difference of 5.7% for

high Reynolds. The *DL* curve is accordance with the experimental measurements performed at NASA Ames [99] and the general trend suggest the higher the Reynolds the stronger the aerodynamic interaction between the rotor resulting in worsen C_T values.

(a) Thrust coefficients   (b) Download factor
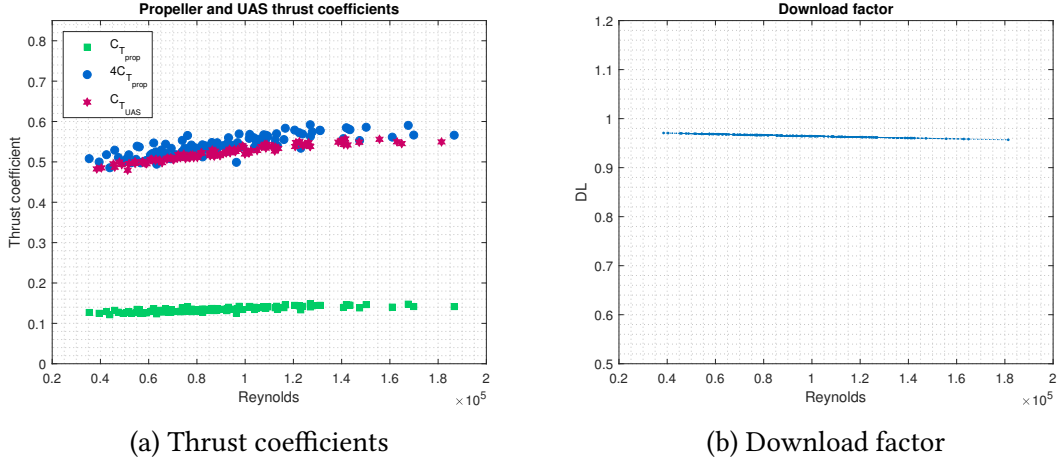
Figure 5.19: Comparison between single rotor and UAS thrust coefficients

5.4 Measurement Uncertainty

A detailed analysis of measurement uncertainty was not the objective of this studty as an in-depth analysis of the uncertainty of the measurement chain is still under discussion in terraXcube facility. To this end, the methodology presented in [17] will be a necessary starting point for further uncertainty analysis. Some considerations are reported in this section for completeness to provide suggestion for future works.

A detailed analysis of sources of uncertainties in the overall measurement chain will be required. To this end, a preliminary reference related to UAS testing is s reported in [100]. The authors focus on load cell uncertainty analysis while limited considerations are made for the ESC voltage and current data. In the aforementioned work, in the uncertainty analysis the overall measurement chain uncertainties (i.e. wind speed, UAS attitude, environmental conditions sources of uncertainty) is not reported and the analysis is limited to standard deviation values about the mean. The same approach is followed in our research work. For all the experimental data, mean values as well as the standard deviation about the means are computed as these are the only quantifiable source of uncertainty as reported in Appendix A and B. A detailed analysis on measurement uncertainties will be considered in future works.

5.5   Final considerations

In this Chapter, the experimental data collected for propeller and full vehicle were presented in terms of thrust and power coefficients as a function of Reynolds number. In general, the $C_T(R_e)$ curve shows a linear trend with increasing Reynolds, in accordance with the experimental activities performed by Brandt, Selig, Deters and Russell. Worsen propeller and vehicle thrust capabilities at low Reynolds numbers are experienced owing to the laminar separation bubble. On the other hand, constant torque and power coefficients suggest they are not affected by the surrounding air atmospheres.

Details on brushless motor performance are provided at different altitude and temperature. As the air density decreases, the motor response to throttle commands experience longer time constants meaning that the propeller and vehicle are less reactive to pilot commands. Moreover, low temperature are responsible for reduced motor and ESC resistance but increased no-load current, resulting in worsen motor efficiency in cold environmental conditions.

Full vehicle performance are essentially the same as for isolated propeller as the physical phenomenon is once again the laminar separation bubble experienced by each rotor. However, the comparison between isolated propeller and quadrotor UAS suggest a slightly influence of rotor-to-rotor interaction as well as airframe effect on thrust coefficient. The experimental data reveals a reduction in UAS thrust coefficient up to 5.7% compared to isolated propeller performance especially when high Reynolds numbers are achieved.

Chapter 6

Propulsion system simulation

In the following chapter, Section 6.1 focus on a simplified mathematical model for the simulation of a brushless motor. The presented model allows preliminary consideration during the design process and it is validated with the experimental data discussed in previous Chapter. Section 6.2 provide implementation details of the Blade Element Momentum Theory, including a comparison between simulation results and propeller experimental data measured in terraXcube.

6.1 Brushless motor simulation

The propulsion system of multicopter UAS usually leverages Brushless DC motors (BLDC). They consist of a stator, commonly a three phase star connection winding, and a rotor where the permanent magnets are installed. In a typical configuration (Out-Runner BLDC), the rotor is part of the motor case. The main advantage of BLDC motor is the electronic commutation performed by the Electronic Speed Controller (ESC), without any mechanical commutator as used in brushed DC motor. Transistors and diodes are arrange to switch on and off each motor phase according to the rotor position. To this end, *H-Bridges* are usually involved. Compared to a traditional brushed DC motor, longer lifetime, faster motor speed and higher motor efficiency are achieved using brushless motors [61].

6.1.1 Model description

As reported in [118], it is possible to model a BLDC motor as a brushed DC motor. The equivalent electrical circuit is reported in Figure 5.11. As suggested in [91], it is important to highlight the role of the throttle as it is responsible for the actual motor voltage supply. When a full throttle is set (100% THRL), the ESC provides the whole power supply to the motor windings. On the other hand, a 0% THRL condition result in no-voltage supplied by the ESC to the windings and motor does not spin. Therefore, when a 50% throttle is set the effective voltage supplied by the ESC to the motor

windings is equal to half the power supply. In addition, the electronic speed controller commutations result in power loss [38] even though high efficiency levels are usually achieved ($85-90$ %).

Considering a simplified BLDC model as in Figure 5.11b, the electrical current required by the motor is computed using Eq. 6.1, where V is the supply voltage, Ω is the motor speed and K_V is the speed constant, usually provided by the manufacturer.

$$I = \frac{V - \Omega/K_V}{R} \tag{6.1}$$

The motor shaft power P_M is computed from the electrical power subtracting the power loss due to Joule effect in the winding resistance R (total resistance including motor windings and ESC) and the no load-current I_0,

$$P_M = (V - IR)(I - I_0). \tag{6.2}$$

The motor torque Q is evaluated by the shaft power given the motor speed Ω, as in Eq. 6.3

$$Q = \frac{P_M}{\Omega}. \tag{6.3}$$

Finally, the electronic speed controller is modelled considering a linear relationship between the input pulse width modulation signal and the effective motor speed voltage V as in Eq.

$$V = V_0 \frac{\text{THRL}}{\text{THRL}_{\text{max}}}, \tag{6.4}$$

where V_0 correspond to the battery voltage supply, THRL is throttle command while THRL_{max} is maximum throttle signal. Implementation details are reported in Appendix C.

6.1.2 Simulation results

All the simulations are performed considering the T-Motor 3508 $380KV$ motor, the same used for the experimental testing described in Section 5.2. Simulation parameters are reported in Table 6.1.

Parameter	Value	UOM
K_V	380	$[rpm/V]$
R	510	$[\Omega]$
I_0	0.4	$[A]$

Table 6.1: Brushless motor simulation parameters
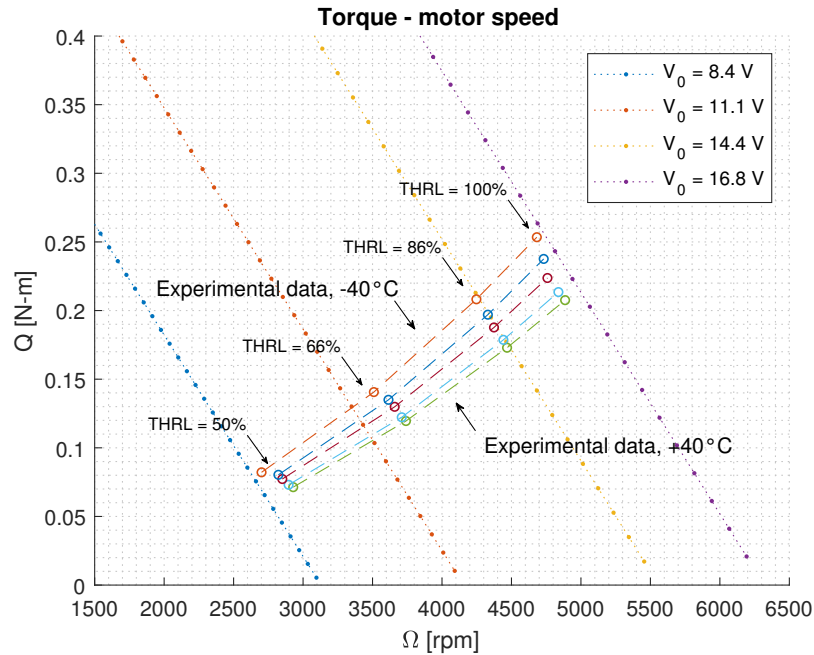
Figure 6.1: Torque to motor speed curve - simulation results and experimental data
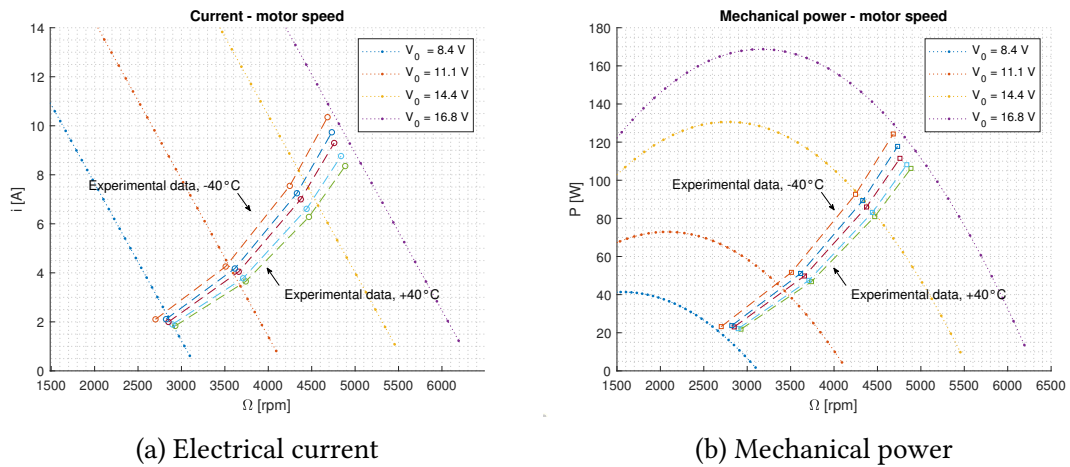
(a) Electrical current (b) Mechanical power

Figure 6.2: Electrical current and mechanical power - simulation results and experimental data

Figure 6.1 shows the simulated torque to motor speed for different supply voltage. Simulation results are represented by dotted straight lines while circle markers are the experimental data collected during propeller test in terraXcube for different temperature at sea level conditions. The simulated $Q - \Omega$ is characterized by a linear behaviour with a decreasing torque as motor speed is fasten. The experimental $Q - \Omega$ data allow

to evaluate the motor-propeller matching chart. Simulation results for $V_0 = 14.4\ V$ shows a good overlap with the measured torque and motor speed for a throttle level of 86%. Similar considerations are valid for the electrical current in Figure 6.2a; simulation results and data experimentally collected in terraXcube reveal a reasonable overlap especially for low throttle commands. The simulated motor shaft power is given with respect to the motor speed in Figure 6.2b where a parabolic trend is clearly identifiable as expected from Eq. 6.2.

The propeller matching chart shown in previous figures reveals the simplified mathematical model implemented is able to predict motor performance in accordance with the experimental data. Some discrepancies are related to model assumptions and measurement uncertainties. A major role is played by the ESC power loss which is usually simulated using a bi-linear model accounting for throttle and current [38]. A detailed power motor characterization would require a dedicated power meter to develop empirical model for the components under test, out of the scope of this study. The simplified model proposed in this work still remains a suitable engineering tool for preliminary evaluation during the designing phase of the UAS propulsion system.

6.2   Propeller simulation

In the following Section, the focus is given to the Blade Element Momentum Theory implementation in order to provide a way to predict propeller thrust and torque coefficients based on geometrical data available for the propeller used in the experimental tests.

6.2.1   Model assumptions

The Blade Element Momentum Theory described in Section 3.1.3 is implemented in Matlab to compare experimental data and simulation results (the code is reported in Appendix C) . Some important assumptions are highlighted:

– The T-Motor 15'x5' propeller is characterized by a continuous varying airfoil shape in the radial direction, as shown in Figure 3.7. Moreover, each airfoil is not comparable with conventional airfoils, such as NACA $4 - 5$ digits or Clark-Y. To reduce the complexity of the problem, as the blade element momentum theory is intended for preliminary propeller performance evaluation, the airfoil located at 50% of the radius is considered as the most significant airfoil shape and used for all the blade elements. This assumption corresponds to a zero-order approximation. The geometry of the airfoil, twist and chord distribution is taken from [100].

– A high quality aerodynamic database for the propeller airfoil is required. The major complexity is the estimate of drag and lift coefficient according the airfoil

shape and local Reynolds number. The aerodynamic coefficients (lift and drag) are evaluated using JavaFoil [43] considering angle of attacks from $-10°$ to $+20°$, and Reynolds numbers in range $5E3$ to $4.5E5$. The estimated airfoil polar data using JavaFoil for the selected T-Motor section are reported in Figure 6.3. Low Reynolds number effects are shown for both lift and drag coefficient. As the Reynolds increases, the maximum lift coefficient and stall angle (Figure 6.3a) increase as well due to the capability of the airflow streamline to handle higher gradient pressure [46]. On the other hand, low Reynolds numbers result in higher drag coefficients (Figure 6.3b) as a consequence of air viscosity effect. It is important to highlight that JavaFoil is a relative simple program used to perform potential flow analysis as well as boundary layer analysis. A major limitation is that this software does not model laminar separation bubbles and turbulent flow separation. XFOIL was also considered to gather airfoil's lift and drag coefficients; however, due to the airfoil shape (T-Motor airfoil is not a *conventional* airfoil) and the low Reynolds of interest, XFOIL was not able to converge during the computation at different angle of attacks. For this reason, JavaFoil was used taking in mind its limitations. To this end, a detailed CFD analysis was planned based on 3D laser scan of the propeller as well as suitable mathematical model to handle the transition from laminar to turbulen airflow and laminar separation bubble [13].

– As the BEMT model is based on a 2D airflow description, a correction factor is required to account for tip vortex loss and provide a zero lift as the propeller radial direction approaches the tip section. Prandlt tip loss coefficient [68, 94] is implemented as follows

$$F = \frac{2}{\pi}\arccos(e^{-f}),\tag{6.5}$$

with the localized correction factor f computed as

$$f = \frac{B}{2}\frac{1-r}{r\sin(\phi)},\tag{6.6}$$

where B is the total number of blades, r is the local radial distance from the propeller hub and ϕ is the inflow angle.

6.2.2 Simulation results

Thrust simulation results in standard air temperature and sea level conditions are presented in Figure 6.4 with a black star marker; other experimental data are included for a direct comparison: thrust data in terraXcube are reported by a red dashed square marker, NASA measurements are blue dashed circles and T-Motor data-sheet are green diamonds. While the manufacturer's data overestimate the thrust generated by the propeller (both data collected by NASA and in terraXcube reveal lower thrust values), the BEMT results are close to the measurements performed in terraXcube. The maximum

(a) Lift coefficient
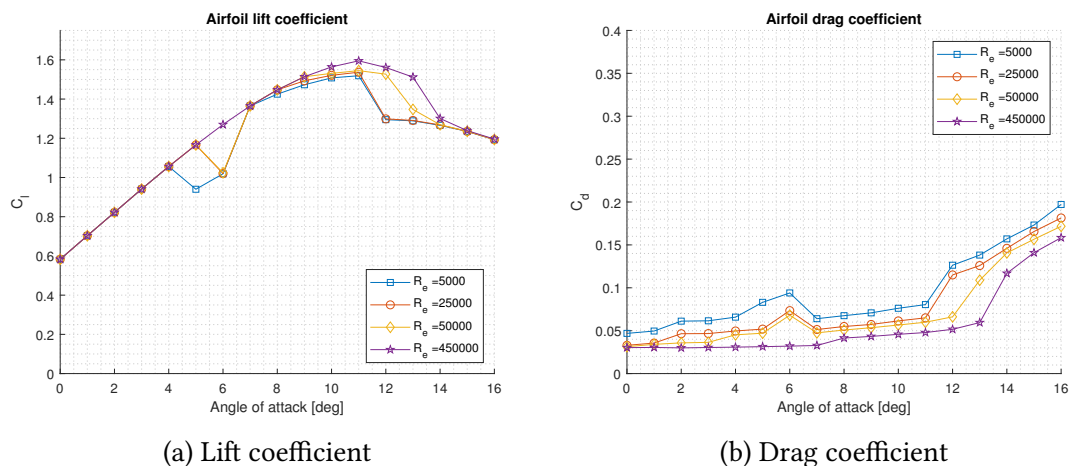
(b) Drag coefficient

Figure 6.3: Lift and drag coefficients for the T-Motor 15' x 5' propeller, airfoil located at 50% of the propeller radius
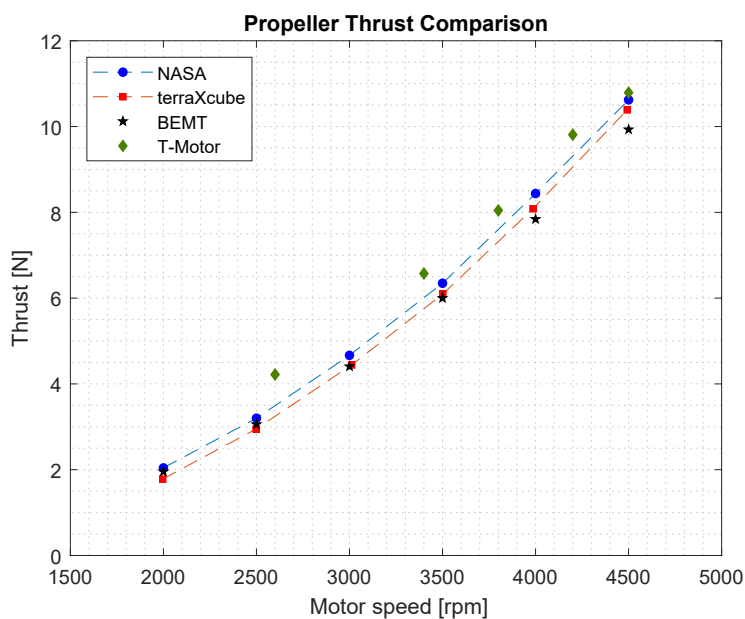
Figure 6.4: Comparison between experimental data and BEMT simulation, standard temperature and sea level test condition

thrust percent difference between BEMT simulations and terraXcube data is 8.8% at the minimum speed with a decreasing percent difference for faster motor speed (4% difference at 4500 rpm) as a result of reduced effect of low Reynolds on propeller aerodynamic performance.

Thrust and torque coefficients are shown in Figure 6.5. While the thrust coefficient

(a) Thrust coefficient

(b) Torque coefficient
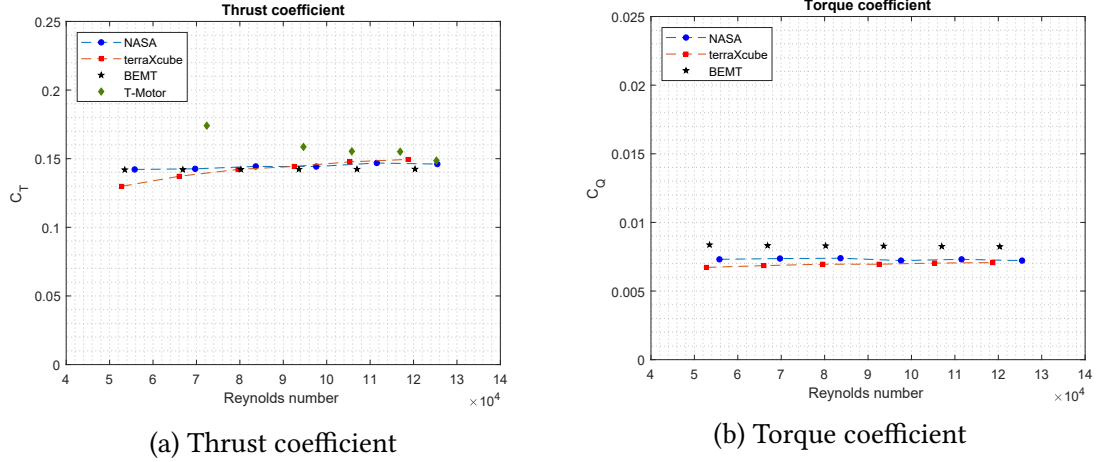
Figure 6.5: Thrust and torque coefficients for the T-Motor 15' x 5' propeller, standard temperature and sea level test condition

is close to the experimental data (NASA and terraXcube), the torque coefficient computed by the BEMT simulation over-estimates the measured values, with an average difference of 20%. This behaviour could be related to the over-prediction of the airfoil drag coefficients by JavaFoil.

Thrust and torque coefficients computed by the BEMT and experimental data are compared in Figure 6.6, while the percentage differences are in Fig. 6.7. Considering the thrust coefficient, the BEMT simulation is able to make reasonable prediction of the propeller C_T for Reynolds number within the range $8E4$ to $2E5$ as the percentage difference with the experimental data is almost $\pm 5\%$. For lower Reynolds numbers, the BEMT over-predicts thrust coefficient as the aerodynamic database computed in JavaFoil does not account non-linearities in lift and drag coefficient values due to laminar separation bubble. Simulated propeller performance for Reynolds number below $8E4$ are affected by a percentage error grater than 10% compared to measured values by experimental testing. For the torque coefficient C_Q, the BEMT simulation provides a systematic over estimation, with an average percentage difference of 20% for Reynolds number in range $8E4$ to $2E5$ and higher values as low Reynolds are set. Once again, the BEMT results are strongly affected by the aerodynamic database and its capabilities to describe lift and drag coefficients of the airfoil, especially when low Reynolds numbers are considered. Considering the BEMT is a relatively simple tool for preliminary propeller predictions, the comparison with the experimental data suggests more advanced techniques, such as Computational Fluid Dynamics (CFD), should be leveraged when extremely low Reynolds flow are of interest. While better performance estimation are possible with CFD, drawbacks related to the detailed CAD model, grid resolution as well as computational cost arise. For these reasons, the BEMT still remains an important tool for preliminary assessment when propeller geometry is available and standard

atmospheres are considered.

(a) Thrust coefficient

(b) Torque coefficient
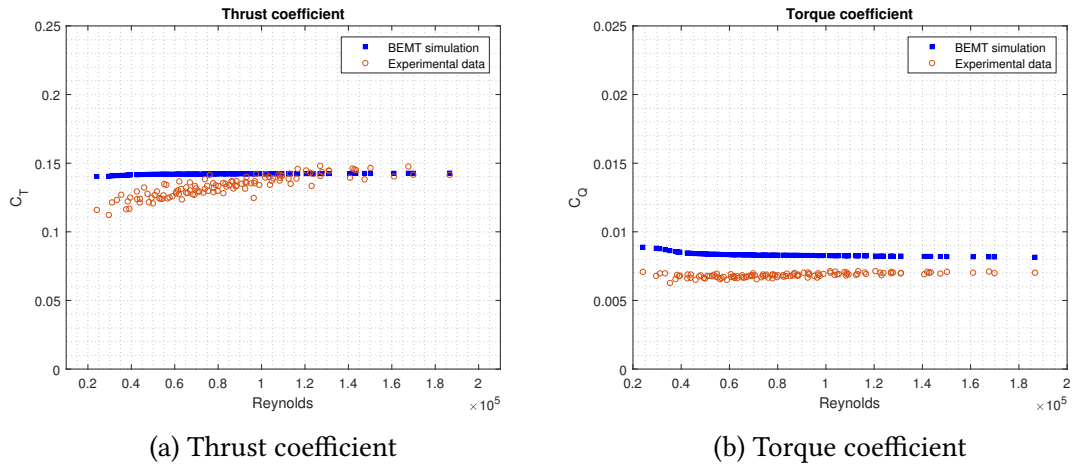
Figure 6.6: Experimental data and BEMT simulation comparison for the thrust and torque coefficients of the T-Motor 15' x 5', all the simulated atmosphere tested in terraXcube laboratory

(a) Thrust coefficient

(b) Torque coefficient
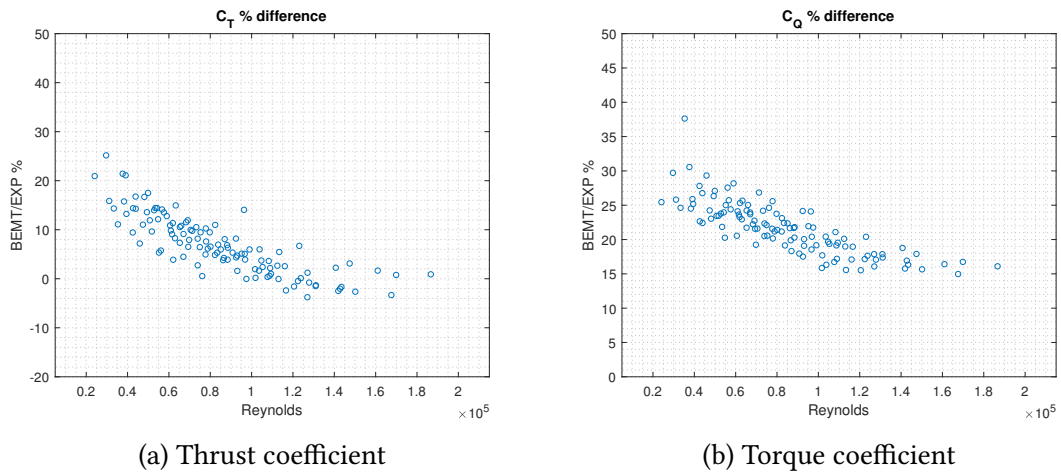
Figure 6.7: BEMT thrust and torque coefficients percentage difference compared to experimental data collected in terraXcube laboratory

6.3   Final considerations

In this Chapter the mathematical tools used to describe the propulsion system of UAS vehicles have been preseted. The simulation model proposed in this study include modelling of the brushless motor as well as the propeller performance.

The mathematical model used for DC brushless motor simulation implemented is based on phisical quantities measured during the experimental testing in terraXcube. The parameters considered by the model are the overall electrical resistance (motor windings and electronic speed controller), no load current arising power loss friction and the motor speed constant. Motor torque, current and mechanical power have been reported with respect to the motor speed for different supply voltages. Moreover, propeller torque, elecitrical current and mechanical power collected during the experimental acitivity in terraXcube were included in order to evaluate the motor-propeller matching.

The Blade Element Momentum Theory, presented in Chapter 3, was implemented considering the propeller leveraged for the experimental tests. The software implementation required important assumption concering the geometrical as well as aerodynamics of propeller sectional airfoils. Lift and drag coefficients were evaluated using JavaFoil software considering the airfoil shape at 50% of the propeller radius Reynolds number range over the propeller radial direction.

A comparison between the experimental propeller coefficient and those computed using the BEMT tool was reported. Firstly, a standard air atmosphere was considered (ambient temperature and sea level conditions): thrust and torque coefficients estimated by BEMT are in accordance with the experimental data collected in this study and with those measured at NASA Ames. In general, the BEMT simulation provides a C_T close to the experimental thurst coefficient while C_Q is generally over-estimated. A possible cause is related to the aerodynamic coefficients used by the BEMT for each blade element. Considering non-standard atmospheres (low temperature and pressures), low Reynolds airflow conditions are preponderant and non-linearities owing to laminar separation bubble are responsible for over-estimated C_T and C_Q coefficients. As soon as the Reynolds number is increased, the difference between the thrust coefficient computed using BEMT and the experimental value is strongly reduced. The torque coefficient is constantly over-estimated by BEMT compared measured C_Q and suggest to use improved aerodynamic data for higher simulation accuracies. Unfortunately, the aerodynamic characterization of propellers used by small UAS is a complex tasks owing to a continuously varying airfoil shape along the propeller radial direction. More advance techiniques might be considered, such as CFD analysis. The BEMT still remains an important tool for preliminary predictions of propeller performance when standard atmospheric conditions are considered. On the other hand, experimental testing is needed when very low Reynolds numbers arise in order to collect high quality data affected by non-linearities on propeller airfoils.

Chapter 7

Conclusions

In this PhD dissertation, the experimental testing of Unmanned Aircraft Systems under extreme environmental conditions was carried out.

Firstly, wind tunnel facilities for UAS testing were reported to highlight important limitations related to data collection of small scale multirotor UAS configurations. While research studies were conducted in wind tunnel laboratories, important environmental parameters, such as temperature and altitude have never been studied owing to the non-reproducibility of the same climatic conditions.

The proposed experimental setup allowed a systematic approach to investigate small scale UAS (multirotors) and their propulsion systems under extreme environmental conditions. The test bench consist of thrust/torque load cell, tachometer for speed sensing as well as shunt resistors for collection of electrical power data. A wide range of environmental conditions were considered. While standard temperature and sea level altitude provide a reference atmosphere for a comparison with experimental data already available in literature, the proposed test procedures allowed to quantify low temperature and pressure effects on thrust generated by propellers as well as full vehicle performance.

The experimental data were analyzed considering thrust, torque and power versus motor speed for both isolated rotor and full vehicle (quadrotor UAS). Four throttle levels were set for each simulated atmosphere inside the climatic altitude chamber. Propeller and vehicle coefficients (thrust, torque and power) were considered with respect to Reynolds numbers to highlight laminar separation bubble effect resulting from low Reynolds number flow conditions.

Thrust coefficient computed from experimental data showed linear trend with increasing values as higher Reynolds numbers are considered. Thrust coefficient reduction at low Reynolds is a consequence of laminar separation bubble occurring when high altitude and low temperature are set owing the region of separated flow over the propeller airfoils. While the section lift coefficient strongly affects the propeller C_T, the combination of lift and drag coefficients along the propeller radius results in constant torque and power coefficients, which are not affected by Reynolds number.

The propulsion system of small scale UAS was simulated leveraging the BEMT to describe the propeller aerodynamics. A major limitation related to the simulation implementation was related to the geometrical data of the propeller owing to the continuous varying airfoil shape along the propeller radial direction. Moreover, the comparison between the experimental data and those computed using BEMT revealed this simulation tool is not able to fully describe propeller performance when unconventional weather conditions are considered. The experimental testing still remains an essential methodology to assess UAS performance and collect high quality data.

Future works include the definition of additional testing scenarios. First of all, the characterization of propeller thrust and power coefficients when icing conditions occur. Preliminary studies were carried out considering low temperature air conditions neglecting altitude effects. A custom ice-wind tunnel was designed in terraXcube to perform qualitative analysis on ice accretion over small scale fixed wing vehicles. The proposed experimental setup represent a basis for further analysis on ice-accretion for unmanned vehicles in order to define a strategy to mitigate undesired effects. Furthermore, battery performance under low temperature and high altitude conditions are important topics related to future rotorcraft and aircraft electrification.

Free flight tests in terraXcube are also included in future works as they provide a way to systematically study UAS stability and their relation to extreme weather conditions. The experience gained during this PhD activity provide an important starting point. In order to enable autonomous free flight tests inside terraXcube, further steps are required to improve the navigation strategy for indoor tests. As reported in Appendix D, the author investigated different architecture, with optical sensors providing the best results. Visual Inertial Odometry algorithms will be essential to provide accurate pose data to autopilots. Moreover, sensor integration with open source autopilot projects, such as PX4 or Ardupilot, is not trivial and it usually requires fine tuning of the digital filter to reach stable hover flight. To this end, during the PhD programme a custom autopilot was developed for indoor applications in order to have total control of the software modules. The target board was a low power micro-controller (ST Nucleo L432KC) that ensures enough computational power for low level control while a dedicated onboard companion computer (Orange Pi) was in charge of high level tasks, such as optical sensor integration and communication with the ground station.

Free flight tests in terraXcube were not accomplished due to safety considerations and limited pose accuracy obtained during preliminary flight tests in standard atmosphere conditions. However, broader objectives were reached including UAS simulation [27], path planning [90] and autopilot Software/Hardware-In-The-Loop [82]. Finally, future works include also topic related to Artificial Intelligence for the management of UAS and their cooperation with manned aviation. To this end, a preliminary UAS Traffic Management (UTM) strategy was proposed by the author in [89] leveraging a priority based approach. Multi-agent path planning within the context of UTM will be also considered by the author.

In conclusion, the experimental data collected in this PhD activity, in collaboration with terraXcube, will be essential to populate UAS performance database and step forward on UTM development. The ultimate objective of this PhD thesis is to allow safe UAS flight under unconventional weather conditions, leveraging the experimental methodology proposed to assess UAS performance.

Appendix A

Propeller experimental data

Sea level altitude - measurements							
t [℃]	p [mbar]	THRL [%]	Ω [rpm]	T [N]	Q [Nm]	I [A]	V [V]
40.65	987	50	2929	3.5058	0.0713	1.8348	16.7
41.23	987	66	3741	5.894	0.1195	3.6507	16.6
41.29	987	86	4468	8.5808	0.1729	6.2811	16.5
41.61	987	100	4886	10.3062	0.2076	8.3567	16.3
20.19	987	50	2896	4.0691	0.0731	1.8958	16.7
20.25	987	66	3710	6.7217	0.1222	3.778	16.6
20.36	987	86	4442	9.8707	0.1787	6.6107	16.4
20.43	987	100	4838	11.8806	0.2135	8.7648	16.3
-0.28	986	50	2850	4.0167	0.0773	1.9962	16.7
-0.48	986	66	3659	6.9574	0.1299	4.0458	16.6
-0.75	986	86	4374	10.2133	0.1877	7.0007	16.4
-1.04	986	100	4759	12.1741	0.2237	9.2972	16.3
-19.83	987	50	2822	3.9461	0.0803	2.1081	16.7
-19.4	987	66	3615	6.9135	0.135	4.1766	16.6
-19.45	987	86	4330	10.2788	0.197	7.2477	16.4
-19.34	987	100	4732	12.4542	0.2376	9.7355	16.3
-41.58	985	50	2701	4.3436	0.0821	2.1024	16.7
-41.61	985	66	3509	7.444	0.1406	4.2573	16.6
-41.27	985	86	4248	11.0616	0.2082	7.5479	16.4
-40.85	984	100	4683	13.4102	0.2534	10.3503	16.3

Table A.1: Propeller test, sea level altitude - measurements

Sea level altitude - standard deviation							
t [℃]	p [mbar]	THRL [%]	Ω [rpm]	T [N]	Q [Nm]	I [A]	V [V]
0.54	0.05	0	19	0.046	0.001	0.096	0.007
0.27	0.05	0	28	0.073	0.001	0.095	0.006
0.36	0.05	0	35	0.136	0.001	0.091	0.006
0.11	0.05	0	37	0.107	0.001	0.085	0.005
0.01	0.05	0	12	0.035	0.001	0.101	0.007
0.03	0.05	0	25	0.027	0.001	0.101	0.007
0.03	0.05	0	39	0.031	0.001	0.073	0.005
0.03	0.05	0	36	0.096	0.001	0.088	0.005
0.09	0.08	0	16	0.04	0.001	0.116	0.008
0.11	0.05	0	26	0.058	0.001	0.099	0.006
0.12	0.05	0	38	0.078	0.001	0.087	0.006
0.15	0.05	0	34	0.082	0.002	0.09	0.006
0.20	0.05	0	24	0.056	0.001	0.123	0.008
0.13	0.05	0	20	0.063	0.001	0.106	0.007
0.08	0.05	0	26	0.08	0.001	0.103	0.006
0.04	0.05	0	33	0.087	0.001	0.096	0.006
0.10	0.05	0	20	0.06	0.001	0.11	0.007
0.13	0.05	0	20	0.067	0.001	0.124	0.008
0.30	0.05	0	36	0.12	0.001	0.113	0.007
0.14	0.05	0	40	0.138	0.002	0.121	0.007

Table A.2: Propeller test, sea level altitude - standard deviation

1500 m altitude - measurements							
t [°C]	p [mbar]	THRL [%]	Ω [rpm]	T [N]	Q [Nm]	I [A]	V [V]
37.82	850	50	2978	3.1945	0.0632	1.6791	16.7
38.49	850	66	3824	5.5042	0.1057	3.3177	16.6
38.74	850	86	4585	8.1779	0.1547	5.7511	16.5
38.95	850	100	5022	9.9512	0.1874	7.689	16.4
18.48	850	50	2934	3.3304	0.0655	1.7492	16.7
19.01	850	66	3783	5.8155	0.1101	3.4658	16.6
19.54	850	86	4559	8.6163	0.1608	6.0058	16.5
19.9	850	100	4986	10.4706	0.1941	8.011	16.4
-1.59	850	50	2902	3.4895	0.0705	1.8178	16.7
-1.2	850	66	3734	6.0165	0.1181	3.6503	16.6
-0.78	850	86	4494	8.9245	0.1724	6.3409	16.5
-0.52	850	100	4928	10.8653	0.2085	8.5248	16.4
-20.63	849	50	2820	3.6828	0.0704	1.8552	16.7
-20.45	851	66	3677	6.5639	0.1224	3.7863	16.6
-20.09	850	86	4449	9.7875	0.1809	6.6429	16.5
-19.74	849	100	4885	11.8195	0.2191	8.9405	16.4
-40.44	845	50	2730	3.7475	0.0725	1.8681	16.7
-40.82	844	66	3585	6.8093	0.1275	3.8493	16.6
-41.49	845	86	4368	10.3917	0.1916	6.8884	16.5
-41.65	850	100	4841	12.9488	0.2375	9.5853	16.3

Table A.3: Propeller test, 1500 m altitude - measurements

1500 m altitude - standard deviation							
t [℃]	p [mbar]	THRL [%]	Ω [rpm]	T [N]	Q [Nm]	I [A]	V [V]
0.41	0.08	0	31	0.065	0.001	0.087	0.006
0.20	0.09	0	18	0.044	0.001	0.094	0.006
0.16	0.15	0	41	0.072	0.001	0.082	0.005
0.09	0.09	0	46	0.087	0.001	0.077	0.005
0.21	0.14	0	13	0.045	0.001	0.093	0.007
0.13	0.13	0	18	0.046	0.001	0.099	0.006
0.11	0.05	0	24	0.044	0.001	0.106	0.007
0.07	0.08	0	48	0.064	0.001	0.077	0.005
0.14	0.07	0	12	0.057	0.001	0.103	0.007
0.16	0.06	0	18	0.077	0.001	0.104	0.007
0.13	0.06	0	26	0.081	0.001	0.099	0.006
0.07	0.05	0	31	0.073	0.001	0.084	0.005
0.05	0.08	0	17	0.038	0.001	0.12	0.008
0.10	0.57	0	18	0.044	0.001	0.118	0.007
0.15	0.26	0	39	0.095	0.001	0.109	0.006
0.12	0.22	0	48	0.065	0.001	0.094	0.006
0.09	0.34	0	19	0.05	0.001	0.124	0.008
0.16	0.12	0	25	0.05	0.001	0.121	0.007
0.16	0.73	0	28	0.06	0.001	0.119	0.007
0.15	1.54	0	48	0.084	0.001	0.108	0.006

Table A.4: Propeller test, 1500 m altitude - standard deviation

3000 **m altitude - measurements**							
t [℃]	*p* [**mbar**]	**THRL** [%]	Ω [**rpm**]	*T* [**N**]	*Q* [**Nm**]	*I* [**A**]	*V* [**V**]
39.37	704	50	3028	2.6712	0.0545	1.4909	16.7
40.91	705	66	3926	4.6676	0.0918	2.9247	16.6
41.36	705	86	4752	6.9097	0.1346	5.0461	16.5
41.38	705	100	5223	8.4997	0.1641	6.765	16.4
18.87	705	50	2997	2.7481	0.0559	1.5703	16.7
19.54	705	66	3889	4.7752	0.0946	3.0599	16.6
20.02	705	86	4712	7.2802	0.141	5.3406	16.5
20.39	705	100	5167	8.9507	0.1711	7.1249	16.4
-0.48	704	50	2963	2.8584	0.0584	1.6022	16.7
-0.18	705	66	3862	5.031	0.1008	3.2293	16.6
0.03	705	86	4644	7.6207	0.15	5.6032	16.5
0.3	705	100	5101	9.5337	0.1836	7.6053	16.4
-20.44	705	50	2910	3.1181	0.0601	1.6776	16.7
-20.07	704	66	3789	5.3519	0.1034	3.303	16.7
-20.29	704	86	4602	8.3339	0.1573	5.8633	16.5
-20.26	704	100	5062	10.3557	0.1941	7.9847	16.4
-41.63	703	50	2783	3.1174	0.0613	1.6412	16.8
-40.62	703	66	3686	5.7447	0.1101	3.3895	16.7
-40.18	703	86	4515	9.0021	0.1679	6.096	16.5
-39.85	703	100	5023	11.3375	0.2095	8.5095	16.4

Table A.5: Propeller test, 3000 m altitude - measurements

3000 m altitude - standard deviation							
t [℃]	p [mbar]	THRL [%]	Ω [rpm]	T [N]	Q [Nm]	I [A]	V [V]
0.70	0.17	0	16	0.032	0.001	0.086	0.006
0.29	0.13	0	29	0.039	0.001	0.086	0.006
0.31	0.12	0	46	0.042	0.001	0.072	0.005
0.18	0.12	0	42	0.063	0.001	0.071	0.004
0.28	0.15	0	18	0.039	0.001	0.094	0.007
0.10	0.14	0	27	0.046	0.001	0.109	0.007
0.15	0.13	0	37	0.054	0.001	0.075	0.005
0.08	0.14	0	53	0.057	0.001	0.075	0.005
0.08	0.28	0	16	0.045	0.001	0.096	0.007
0.10	0.10	0	21	0.04	0.001	0.097	0.006
0.16	0.07	0	31	0.038	0.001	0.105	0.006
0.17	0.08	0	51	0.046	0.001	0.083	0.005
0.13	0.37	0	16	0.032	0.001	0.111	0.007
0.07	0.12	0	16	0.037	0.001	0.112	0.007
0.08	0.17	0	43	0.031	0.001	0.093	0.006
0.10	0.32	0	50	0.053	0.001	0.095	0.006
0.26	0.29	0	12	0.038	0.001	0.121	0.009
0.26	0.14	0	28	0.043	0.001	0.134	0.008
0.17	0.09	0	36	0.066	0.001	0.106	0.006
0.09	0.08	0	45	0.062	0.001	0.108	0.006

Table A.6: Propeller test, 3000 m altitude - standard deviation

4500 m altitude - measurements							
t [℃]	p [mbar]	THRL [%]	Ω [rpm]	T [N]	Q [Nm]	I [A]	V [V]
39.23	579	50	3080	2.3232	0.0452	1.3312	16.7
40.32	580	66	4021	4.1086	0.0777	2.587	16.7
40.67	580	86	4885	6.121	0.1151	4.4634	16.6
40.57	580	100	5391	7.5784	0.1417	5.9929	16.5
19.24	580	50	3054	2.4096	0.0486	1.3797	16.7
19.91	580	66	3979	4.1592	0.082	2.688	16.7
20.27	580	86	4854	6.342	0.1231	4.6998	16.5
20.62	580	100	5341	7.7884	0.1498	6.2733	16.5
-0.3	579	50	3012	2.4461	0.0506	1.418	16.7
-0.14	580	66	3942	4.2707	0.0868	2.7856	16.7
0.09	580	86	4786	6.5876	0.1314	4.9111	16.5
0.29	580	100	5289	8.2468	0.1623	6.6841	16.5
-20.36	580	50	2929	2.5257	0.0497	1.4638	16.7
-19.96	580	66	3878	4.5244	0.0884	2.8855	16.7
-19.98	580	86	4741	7.098	0.1356	5.1484	16.6
-20.04	580	100	5243	8.9212	0.1692	7.0342	16.5
-39.69	579	50	2838	2.6132	0.0517	1.4458	16.8
-39.55	579	66	3796	4.8493	0.0945	2.996	16.7
-39.54	579	86	4640	7.7163	0.1466	5.3912	16.6
-39.8	579	100	5185	9.8384	0.1847	7.5637	16.5

Table A.7: Propeller test, 4500 m altitude - measurements

4500 m altitude - standard deviation							
t [°C]	p [mbar]	THRL [%]	Ω [rpm]	T [N]	Q [Nm]	I [A]	V [V]
0.58	0.10	0	19	0.045	0.001	0.081	0.006
0.17	0.32	0	27	0.034	0.001	0.081	0.006
0.22	0.22	0	31	0.047	0.001	0.083	0.005
0.16	0.05	0	57	0.08	0.001	0.075	0.005
0.32	0.23	0	19	0.043	0.001	0.097	0.007
0.10	0.14	0	24	0.038	0.001	0.086	0.006
0.11	0.30	0	44	0.056	0.001	0.09	0.006
0.10	0.09	0	30	0.052	0.001	0.075	0.005
0.06	0.07	0	13	0.046	0.001	0.093	0.007
0.05	0.13	0	31	0.036	0.001	0.102	0.007
0.12	0.09	0	46	0.035	0.001	0.087	0.006
0.15	0.14	0	54	0.035	0.001	0.084	0.005
0.16	0.16	0	17	0.03	0.001	0.12	0.009
0.04	0.10	0	30	0.029	0.001	0.12	0.008
0.04	0.08	0	23	0.037	0.001	0.096	0.006
0.03	0.09	0	31	0.072	0.001	0.095	0.006
0.04	0.05	0	21	0.039	0.001	0.114	0.008
0.07	0.07	0	29	0.036	0.001	0.128	0.008
0.14	0.06	0	35	0.044	0.001	0.104	0.006
0.20	0.13	0	47	0.094	0.001	0.111	0.006

Table A.8: Propeller test, 4500 m altitude - standard deviation

6000 m altitude - measurements							
t [℃]	p [mbar]	THRL [%]	Ω [rpm]	T [N]	Q [Nm]	I [A]	V [V]
39.74	474	50	3139	1.9331	0.0363	1.1905	16.7
40.85	474	66	4104	3.4289	0.0643	2.2628	16.7
40.86	474	86	5016	5.1982	0.0966	3.8895	16.6
40.91	474	100	5549	6.4818	0.12	5.2527	16.5
18.68	473	50	3102	1.9889	0.0412	1.2254	16.7
19.57	474	66	4089	3.5707	0.0713	2.3884	16.7
20.08	474	86	4987	5.3792	0.1058	4.0952	16.6
20.47	474	100	5505	6.6547	0.13	5.5045	16.5
0.14	474	50	3067	2.0178	0.0422	1.2697	16.7
0.15	474	66	4023	3.5793	0.0732	2.4561	16.7
0.24	474	86	4929	5.5514	0.1119	4.3311	16.6
0.24	474	100	5449	6.9365	0.1382	5.8415	16.5
-20.55	474	50	2995	2.1438	0.0434	1.3093	16.8
-20.7	474	66	3957	3.8524	0.0765	2.5397	16.7
-20.37	474	86	4864	6.0352	0.1178	4.4944	16.6
-19.45	474	100	5409	7.6219	0.1461	6.1146	16.5
-40.27	473	50	2873	2.1636	0.0453	1.2741	16.8
-39.95	473	66	3885	4.1023	0.082	2.6047	16.7
-39.8	473	86	4778	6.3739	0.1262	4.6449	16.6
-39.71	473	100	5354	8.2687	0.161	6.5779	16.5

Table A.9: Propeller test, 6000 m altitude - measurements

6000 m altitude - standard deviation							
t [℃]	p [mbar]	THRL [%]	Ω [rpm]	T [N]	Q [Nm]	I [A]	V [V]
0.54	0.13	0	15	0.043	0.001	0.083	0.006
0.15	0.12	0	36	0.043	0.001	0.09	0.006
0.21	0.09	0	45	0.054	0.001	0.081	0.005
0.16	0.11	0	37	0.056	0.001	0.076	0.005
0.42	0.14	0	21	0.048	0.001	0.085	0.006
0.13	0.12	0	25	0.046	0.001	0.085	0.006
0.13	0.16	0	47	0.045	0.001	0.078	0.005
0.07	0.13	0	57	0.038	0.001	0.072	0.005
0.05	0.11	0	19	0.03	0.001	0.098	0.007
0.12	0.10	0	31	0.03	0.001	0.097	0.007
0.12	0.08	0	27	0.039	0.001	0.088	0.006
0.10	0.10	0	54	0.059	0.001	0.087	0.006
0.04	0.23	0	17	0.033	0.001	0.095	0.007
0.03	0.10	0	29	0.055	0.001	0.108	0.007
0.20	0.12	0	46	0.04	0.001	0.091	0.006
0.23	0.10	0	59	0.077	0.001	0.096	0.006
0.10	0.10	0	19	0.035	0.001	0.118	0.009
0.03	0.10	0	19	0.051	0.001	0.123	0.008
0.14	0.10	0	42	0.07	0.001	0.105	0.006
0.17	0.08	0	51	0.06	0.001	0.108	0.006

Table A.10: Propeller test, 6000 m altitude - standard deviation

9000 **m altitude - measurements**							
t [°C]	*p* [mbar]	THRL [%]	Ω [rpm]	*T* [N]	*Q* [Nm]	*I* [A]	*V* [V]
40.05	309	50	3293	1.4001	0.0294	0.9686	16.7
40.86	309	66	4271	2.489	0.0485	1.7287	16.7
40.88	309	86	5259	3.773	0.0725	2.9251	16.6
40.73	309	100	5847	4.7521	0.09	3.9461	16.6
18.68	309	50	2908	1.0681	0.0251	2.3233	16.7
19.57	309	66	3979	1.988	0.0449	3.0772	16.6
20.08	309	86	5155	3.4664	0.0757	4.5748	16.3
20.47	309	100	5679	4.2946	0.091	5.5312	16.1
0.52	308	50	3193	1.3141	0.0303	1.0296	16.8
0.31	308	66	4203	2.3713	0.0524	1.8878	16.7
0.26	308	86	5171	3.7379	0.08	3.2386	16.6
0.34	308	100	5746	4.7088	0.0993	4.3326	16.6
-20.68	308	50	3105	1.4797	0.0319	1.059	16.8
-19.98	308	66	4117	2.6099	0.0552	1.9499	16.7
-19.43	308	86	5104	4.0002	0.0829	3.3074	16.7
-19.39	308	100	5700	5.1496	0.1059	4.5624	16.6
-40.37	308	50	3026	1.4391	0.0309	1.0638	16.8
-39.77	308	66	4033	2.6451	0.0551	1.9832	16.7
-39.53	308	86	5011	4.3089	0.087	3.4583	16.7
-39.33	308	100	5653	5.6613	0.1142	4.8625	16.6

Table A.11: Propeller test - 9000 m altitude

9000 **m altitude - standard deviation**							
t [℃]	p [**mbar**]	**THRL** [%]	Ω [**rpm**]	T [**N**]	Q [**Nm**]	I [**A**]	V [**V**]
0.51	0.10	0	21	0.066	0.001	0.078	0.006
0.15	0.10	0	31	0.045	0.001	0.075	0.006
0.15	0.09	0	57	0.057	0.001	0.07	0.005
0.15	0.09	0	54	0.075	0.001	0.069	0.005
0.12	0.09	0	11	0.059	0.002	0.003	0.001
0.10	0.04	0	2	0.044	0.002	0.015	0.003
0.15	0.08	0	5	0.039	0.001	0.022	0.004
0.11	0.10	0	6	0.009	0.001	0.022	0.004
0.09	0.08	0	18	0.042	0.002	0.096	0.008
0.06	0.09	0	34	0.023	0.001	0.103	0.007
0.09	0.09	0	50	0.037	0.001	0.09	0.006
0.12	0.09	0	35	0.034	0.001	0.084	0.005
0.16	0.09	0	20	0.028	0.001	0.108	0.008
0.20	0.28	0	45	0.031	0.001	0.117	0.008
0.15	0.08	0	49	0.05	0.001	0.104	0.006
0.12	0.04	0	56	0.064	0.001	0.098	0.006
0.15	0.09	0	14	0.024	0.001	0.105	0.008
0.10	0.09	0	27	0.043	0.001	0.112	0.007
0.13	0.08	0	32	0.047	0.001	0.11	0.007
0.11	0.04	0	62	0.075	0.001	0.098	0.006

Table A.12: Propeller test, 9000 m altitude - standard deviation

Appendix B

Quadrotor experimental data

Sea level altitude - measurements												
t [℃]	p [mbar]	THRL [%]	Ω_1 [rpm]	Ω_2 [rpm]	Ω_3 [rpm]	Ω_4 [rpm]	T [N]	I_1 [A]	I_2 [A]	I_3 [A]	I_4 [A]	V [V]
39.57	997	50	2765	2777	2856	2693	12.666	1.579	1.667	1.518	1.473	16.5
39.45	996	66	3458	3466	3572	3361	20.151	3.138	3.36	3.025	2.945	16.1
39.38	996	86	3995	4023	4131	3946	27.438	4.93	5.342	4.853	4.836	15.7
39.49	996	100	4421	4414	4553	4403	33.857	7.063	7.501	6.989	7.088	15.2
20.19	995	50	2824	2707	2779	2649	13.411	1.645	1.527	1.456	1.482	16.5
20.23	995	66	3480	3416	3502	3341	21.673	3.383	3.289	3.068	3.107	16.1
20.48	995	86	4008	3977	4066	3895	29.503	5.059	5.003	4.806	4.93	15.7
20.81	995	100	4415	4400	4508	4347	36.668	7.726	7.734	7.331	7.471	15.2
0.87	985	50	2876	2633	2720	2714	14.533	1.881	1.531	1.526	1.666	16.5
0.93	985	66	3531	3349	3438	3415	23.353	3.721	3.259	3.16	3.395	16.1
1.06	985	86	4042	3906	3999	3965	31.497	5.787	5.209	5.121	5.443	15.7
1.23	985	100	4399	4340	4442	4382	38.801	8.139	7.777	7.655	7.916	15.1
-17.69	981	50	2920	2645	2734	2814	16.302	2.062	1.671	1.628	1.857	16.5
-18.12	981	66	3550	3349	3430	3426	25.458	4.002	3.563	3.37	3.631	16.1
-18.68	981	86	4061	3886	3977	3965	34.389	6.135	5.576	5.363	5.758	15.6
-18.74	981	100	4372	4333	4426	4353	41.584	8.548	8.542	8.124	8.242	15.2
-39.47	980	50	2807	2635	2713	2723	16.862	1.802	1.548	1.509	1.703	16.5
-39.69	980	66	3474	3358	3430	3369	26.904	3.804	3.525	3.365	3.544	16.1
-39.5	980	86	3979	3922	3979	3895	36.202	6.343	6.138	5.804	5.927	15.6
-38.77	980	100	4338	4310	4388	4316	44.207	8.954	8.918	8.465	8.622	15.1

Table B.1: UAS test, sea level altitude - measurements

Sea level altitude - standard deviation												
t [℃]	p [mbar]	THRL [%]	Ω_1 [rpm]	Ω_2 [rpm]	Ω_3 [rpm]	Ω_4 [rpm]	T [N]	I_1 [A]	I_2 [A]	I_3 [A]	I_4 [A]	V [V]
0.04	0.06	0	16	31	18	25	0.153	0.038	0.036	0.034	0.036	0.005
0.04	0.06	0	21	30	26	22	0.088	0.128	0.129	0.1	0.075	0.005
0.01	0.06	0	31	46	36	26	0.206	0.224	0.233	0.183	0.132	0.019
0.06	0.07	0	39	58	43	36	0.186	0.244	0.284	0.216	0.155	0.024
0.01	0.05	0	21	24	16	20	0.119	0.221	0.244	0.182	0.136	0.015
0.03	0.06	0	26	28	28	26	0.239	0.067	0.07	0.059	0.053	0.011
0.10	0.08	0	33	33	33	30	0.285	0.172	0.163	0.13	0.098	0.022
0.08	0.06	0	50	40	40	34	0.348	0.138	0.112	0.087	0.081	0.022
0.02	0.05	0	14	25	17	14	0.309	0.243	0.259	0.187	0.137	0.021
0.03	0.05	0	24	27	40	24	0.158	0.274	0.315	0.216	0.159	0.023
0.05	0.05	0	33	33	37	34	0.315	0.215	0.268	0.195	0.149	0.021
0.05	0.07	0	36	42	45	40	0.341	0.252	0.284	0.2	0.17	0.022
0.08	0.06	0	21	30	42	21	0.088	0.266	0.298	0.206	0.154	0.023
0.16	0.05	0	27	35	99	27	0.16	0.227	0.249	0.184	0.131	0.024
0.14	0.06	0	31	33	66	33	0.169	0.185	0.175	0.145	0.127	0.022
0.11	0.07	0	38	45	60	34	0.272	0.059	0.069	0.068	0.053	0.011
0.07	0.06	0	18	30	22	18	0.135	0.217	0.24	0.163	0.12	0.018
0.04	0.05	0	25	34	38	25	0.194	0.217	0.277	0.19	0.135	0.019
0.16	0.07	0	35	47	52	42	0.364	0.29	0.252	0.164	0.156	0.025
0.22	0.06	0	39	52	44	36	0.358	0.271	0.252	0.203	0.14	0.02

Table B.2: UAS test, sea level altitude - standard deviation

1500 m altitude - measurements												
t [℃]	p [mbar]	THRL [%]	Ω_1 [rpm]	Ω_2 [rpm]	Ω_3 [rpm]	Ω_4 [rpm]	T [N]	I_1 [A]	I_2 [A]	I_3 [A]	I_4 [A]	V [V]
39.22	850	50	2832	2838	2895	2679	11.076	1.357	1.426	1.324	1.257	16.5
39.15	851	66	3556	3579	3663	3453	18.007	2.656	2.86	2.612	2.551	16.2
39.12	851	86	4115	4160	4259	4067	24.634	4.464	4.851	4.372	4.34	15.8
39.17	850	100	4601	4603	4741	4571	30.883	6.601	7.001	6.463	6.551	15.3
20.66	850	50	2898	2766	2833	2785	11.963	1.465	1.346	1.313	1.377	16.5
20.67	851	66	3582	3506	3598	3523	19.456	3.056	2.891	2.76	2.898	16.2
20.72	850	86	4133	4090	4189	4110	26.989	5.126	5.029	4.711	4.858	15.8
20.79	850	100	4602	4571	4682	4587	33.753	7.383	7.414	6.939	7.17	15.3
1.06	850	50	2972	2671	2763	2804	12.723	1.723	1.337	1.348	1.521	16.5
1.21	850	66	3649	3429	3521	3505	20.678	3.431	2.924	2.886	3.098	16.2
1.37	850	86	4186	4018	4116	4073	28.609	5.448	4.883	4.772	5.039	15.8
1.52	850	100	4571	4497	4613	4524	35.417	7.281	7.033	6.883	7.158	15.3
-17.73	850	50	3004	2709	2799	2845	14.393	1.605	1.209	1.257	1.512	16.5
-18.44	848	66	3651	3416	3512	3522	22.779	3.536	3.074	2.939	3.208	16.2
-18.56	849	86	4199	4004	4093	4078	31.111	5.506	4.908	4.764	5.189	15.7
-18.31	848	100	4532	4495	4585	4499	38.356	7.726	7.594	7.315	7.583	15.3
-39.27	849	50	2863	2714	2768	2794	15.117	1.886	1.675	1.558	1.71	16.5
-38.49	849	66	3533	3451	3514	3487	24.399	3.589	3.391	3.184	3.368	16.2
-38.3	848	86	4070	4028	4089	4031	33.469	5.839	5.674	5.352	5.536	15.7
-39.13	850	100	4476	4455	4533	4480	41.042	8.479	8.465	8.002	8.162	15.2

Table B.3: UAS test, 1500 m altitude - measurements

1500 m altitude - standard deviation												
t [℃]	p [mbar]	THRL [%]	Ω_1 [rpm]	Ω_2 [rpm]	Ω_3 [rpm]	Ω_4 [rpm]	T [N]	I_1 [A]	I_2 [A]	I_3 [A]	I_4 [A]	V [V]
0.02	0.20	0	39	58	40	68	0.142	0.286	0.307	0.416	0.168	0.026
0.02	0.36	0	42	60	49	50	0.139	0.232	0.248	0.180	0.136	0.019
0.00	0.29	0	69	77	75	63	0.157	0.265	0.287	0.198	0.134	0.024
0.04	0.34	0	72	104	87	80	0.197	0.230	0.258	0.182	0.128	0.017
0.01	0.14	0	28	60	37	34	0.075	0.255	0.275	0.205	0.138	0.016
0.01	0.14	0	53	60	78	43	0.137	0.210	0.235	0.172	0.117	0.025
0.02	0.17	0	71	71	70	55	0.227	0.155	0.175	0.144	0.095	0.014
0.02	0.13	0	104	106	88	69	0.272	0.296	0.309	0.222	0.165	0.016
0.06	0.33	0	54	55	55	61	0.168	0.249	0.263	0.195	0.148	0.019
0.04	0.19	0	53	51	96	50	0.145	0.055	0.049	0.061	0.048	0.019
0.05	0.12	0	66	69	72	60	0.206	0.218	0.269	0.197	0.133	0.024
0.02	0.14	0	117	85	93	79	0.219	0.174	0.198	0.139	0.106	0.012
0.16	0.86	0	44	57	88	40	0.185	0.230	0.219	0.153	0.119	0.021
0.22	1.59	0	56	72	188	51	0.178	0.286	0.287	0.216	0.161	0.022
0.15	1.47	0	70	72	132	74	0.267	0.202	0.155	0.135	0.133	0.015
0.07	0.90	0	83	81	136	69	0.317	0.230	0.222	0.186	0.135	0.014
0.22	0.57	0	55	95	65	43	0.141	0.153	0.199	0.145	0.099	0.018
0.21	0.39	0	68	81	128	65	0.313	0.236	0.270	0.200	0.156	0.023
0.16	0.80	0	73	94	108	67	0.246	0.254	0.273	0.206	0.162	0.027
0.20	0.20	0	83	103	119	80	0.375	0.234	0.203	0.130	0.097	0.019

Table B.4: UAS test, 1500 m altitude - standard deviation

3000 m altitude - measurements												
t [℃]	p [mbar]	THRL [%]	Ω_1 [rpm]	Ω_2 [rpm]	Ω_3 [rpm]	Ω_4 [rpm]	T [N]	I_1 [A]	I_2 [A]	I_3 [A]	I_4 [A]	V [V]
38.79	705	50	3106	2974	3040	2995	10.492	1.481	1.404	1.314	1.384	16.5
38.83	706	66	3836	3708	3814	3723	16.621	2.735	2.668	2.488	2.583	16.2
38.9	705	86	4428	4304	4427	4373	22.608	4.411	4.373	4.043	4.292	15.9
39.11	705	100	4883	4811	4943	4786	27.937	6.334	6.506	5.948	6.06	15.5
20.98	705	50	2965	2835	2892	2846	10.186	1.345	1.25	1.195	1.247	16.5
21.01	705	66	3714	3619	3716	3627	16.798	2.726	2.603	2.467	2.557	16.2
21.05	705	86	4310	4249	4350	4244	23.344	4.404	4.327	4.065	4.233	15.9
21.1	705	100	4810	4773	4883	4775	29.768	6.503	6.545	6.127	6.325	15.4
1.68	705	50	3040	2728	2820	2918	10.913	1.54	1.164	1.216	1.379	16.5
1.68	705	66	3766	3530	3628	3609	17.979	2.999	2.501	2.515	2.706	16.2
1.66	705	86	4359	4161	4263	4225	25.09	4.867	4.264	4.2	4.469	15.9
1.63	705	100	4769	4705	4817	4713	31.777	7.03	6.815	6.509	6.699	15.4
-17.78	704	50	3064	2772	2854	2943	12.359	2.133	1.881	1.678	1.744	16.5
-17.74	705	66	3772	3538	3617	3671	19.918	3.393	2.96	2.773	3.05	16.2
-17.92	705	86	4358	4151	4236	4264	27.642	5.628	5.101	4.731	5.062	15.8
-18.15	704	100	4724	4688	4782	4701	34.393	7.06	6.933	6.624	6.887	15.4
-39.04	705	50	2946	2768	2819	2860	12.841	1.915	1.737	1.552	1.624	16.5
-38.87	705	66	3682	3560	3626	3601	21.469	3.358	3.108	2.882	3.074	16.2
-38.63	705	86	4271	4181	4240	4196	29.532	5.432	5.205	4.818	5.033	15.8
-38.3	705	100	4691	4674	4749	4662	36.757	7.612	7.594	7.153	7.341	15.4

Table B.5: UAS test, 3000 m altitude - measurements

3000 m altitude - standard deviation												
t [℃]	p [mbar]	THRL [%]	Ω_1 [rpm]	Ω_2 [rpm]	Ω_3 [rpm]	Ω_4 [rpm]	T [N]	I_1 [A]	I_2 [A]	I_3 [A]	I_4 [A]	V [V]
0.04	0.33	0	17	26	22	20	0.068	0.272	0.308	0.214	0.15	0.025
0.01	0.32	0	28	36	36	28	0.122	0.248	0.273	0.203	0.143	0.026
0.05	0.27	0	38	41	38	29	0.11	0.248	0.269	0.185	0.134	0.024
0.07	0.37	0	125	46	50	42	0.191	0.252	0.293	0.193	0.136	0.021
0.02	0.15	0	13	35	19	19	0.065	0.238	0.265	0.186	0.138	0.021
0.01	0.17	0	27	32	34	23	0.112	0.233	0.275	0.189	0.131	0.021
0.02	0.17	0	77	43	38	29	0.235	0.255	0.285	0.193	0.151	0.023
0.02	0.19	0	85	63	48	44	0.36	0.25	0.271	0.203	0.153	0.022
0.01	0.15	0	21	26	38	21	0.123	0.091	0.087	0.078	0.06	0.007
0.01	0.13	0	30	27	69	28	0.129	0.085	0.095	0.076	0.066	0.008
0.01	0.15	0	39	36	46	35	0.214	0.079	0.073	0.073	0.07	0.006
0.01	0.36	0	68	47	45	46	0.232	0.289	0.342	0.242	0.185	0.028
0.04	0.12	0	20	33	41	22	0.097	0.116	0.168	0.093	0.072	0.01
0.04	0.32	0	30	28	96	28	0.125	0.072	0.076	0.075	0.051	0.006
0.06	0.09	0	39	37	67	32	0.179	0.238	0.262	0.188	0.136	0.023
0.08	0.4	0	41	44	74	44	0.311	0.18	0.193	0.153	0.101	0.017
0.06	0.18	0	23	48	41	18	0.082	0.186	0.19	0.137	0.103	0.01
0.05	0.15	0	30	38	78	27	0.189	0.247	0.282	0.198	0.14	0.022
0.09	0.12	0	41	50	68	34	0.283	0.282	0.283	0.209	0.164	0.022
0.10	0.13	0	45	54	70	40	0.285	0.241	0.304	0.236	0.153	0.022

Table B.6: UAS test, 3000 m altitude - standard deviation

4500 m altitude - measurements												
t [℃]	p [mbar]	THRL [%]	Ω_1 [rpm]	Ω_2 [rpm]	Ω_3 [rpm]	Ω_4 [rpm]	T [N]	I_1 [A]	I_2 [A]	I_3 [A]	I_4 [A]	V [V]
38.54	584	50	3102	3022	3075	3014	8.793	0.995	0.907	0.929	1.036	16.5
39.87	650	66	3926	3823	3914	3812	14.223	2.377	2.326	2.152	2.245	16.3
39.53	705	86	4583	4457	4575	4497	19.811	4.021	3.999	3.633	3.809	16
38.74	705	100	5083	5012	5132	5019	24.808	5.597	5.729	5.261	5.415	15.6
21.65	580	50	3022	2886	2942	2873	8.613	1.278	1.205	1.11	1.146	16.5
21.57	580	66	3818	3728	3795	3657	14.297	2.541	2.432	2.282	2.281	16.3
21.49	581	86	4467	4397	4483	4352	20.36	4.034	3.898	3.639	3.751	16
21.48	581	100	5024	4989	5098	4958	26.438	5.815	5.778	5.427	5.632	15.6
1.63	581	50	3092	2792	2875	2977	9.28	1.241	0.94	0.999	1.165	16.6
1.73	580	66	3428	3374	3429	3328	12.481	1.968	1.929	1.777	1.781	16.4
1.69	581	86	4284	4256	4342	4227	20.314	3.695	3.622	3.438	3.514	16.1
1.52	577	100	4959	4956	5057	4901	27.847	6.214	6.223	5.799	5.936	15.6
-18.7	581	50	3111	2834	2906	3010	10.367	1.562	1.334	1.242	1.367	16.6
-18.68	581	66	3893	3630	3751	3806	16.914	2.881	2.506	2.38	2.643	16.3
-18.18	580	86	4523	4292	4384	4439	23.666	4.686	4.145	3.912	4.325	15.9
-17.59	580	100	4929	4891	4993	4933	29.988	6.55	6.422	6.047	6.341	15.5
-39.05	581	50	3017	2834	2867	2916	10.889	1.307	1.12	1.059	1.21	16.6
-38.89	581	66	3813	3670	3727	3708	18.371	3.166	2.968	2.688	2.804	16.3
-38.75	581	86	4431	4333	4392	4336	26.687	4.879	4.579	4.247	4.467	16
-38.53	581	100	4879	4861	4939	4855	32.448	6.957	7.003	6.498	6.67	15.5

Table B.7: UAS test, 4500 m altitude - measurements

4500 m altitude - standard deviation												
t [℃]	p [mbar]	THRL [%]	Ω_1 [rpm]	Ω_2 [rpm]	Ω_3 [rpm]	Ω_4 [rpm]	T [N]	I_1 [A]	I_2 [A]	I_3 [A]	I_4 [A]	V [V]
0.52	5.47	0	12	21	21	20	0.083	0.196	0.205	0.141	0.113	0.018
0.52	29.53	0	31	33	31	30	0.089	0.054	0.068	0.043	0.043	0.004
0.52	0.66	0	43	47	43	41	0.166	0.067	0.064	0.05	0.051	0.016
0.15	0.41	0	48	49	49	35	0.166	0.263	0.298	0.207	0.159	0.022
0.02	0.18	0	19	31	23	27	0.094	0.129	0.144	0.107	0.072	0.019
0.03	0.17	0	32	33	35	30	0.148	0.063	0.067	0.065	0.057	0.008
0.01	0.16	0	77	40	33	35	0.157	0.164	0.168	0.127	0.093	0.017
0.01	0.16	0	73	63	49	45	0.283	0.096	0.13	0.075	0.058	0.019
0.05	0.2	0	20	30	55	19	0.083	0.246	0.263	0.189	0.134	0.014
0.02	0.17	0	20	29	65	28	0.096	0.225	0.24	0.182	0.135	0.017
0.03	0.16	0	36	37	48	35	0.601	0.06	0.074	0.062	0.056	0.009
0.08	5.49	0	52	48	52	49	0.268	0.247	0.264	0.188	0.136	0.018
0.05	0.17	0	18	21	43	19	0.1	0.251	0.278	0.194	0.142	0.019
0.08	0.24	0	30	31	120	32	0.211	0.278	0.287	0.217	0.164	0.023
0.19	0.23	0	42	42	60	36	0.187	0.294	0.316	0.217	0.17	0.025
0.13	0.1	0	59	51	71	43	0.168	0.067	0.08	0.073	0.054	0.006
0.10	0.19	0	20	45	44	19	0.087	0.174	0.2	0.153	0.107	0.015
0.02	0.13	0	28	39	95	31	0.096	0.17	0.189	0.143	0.111	0.02
0.07	0.12	0	42	46	79	33	2.011	0.272	0.293	0.224	0.164	0.022
0.09	0.14	0	44	61	80	49	0.377	0.31	0.332	0.239	0.184	0.023

Table B.8: UAS test, 4500 m altitude - standard deviation

6000 m altitude - measurements												
t [℃]	p [mbar]	THRL [%]	Ω_1 [rpm]	Ω_2 [rpm]	Ω_3 [rpm]	Ω_4 [rpm]	T [N]	I_1 [A]	I_2 [A]	I_3 [A]	I_4 [A]	V [V]
36.09	475	50	3130	3141	3183	3099	7.434	0.925	0.939	0.89	0.961	16.6
36.31	475	66	3978	3983	4055	3918	12.245	2.258	2.349	2.109	2.116	16.3
36.77	474	86	4673	4694	4780	4607	17.172	3.439	3.609	3.293	3.336	16.1
37.38	474	100	5272	5227	5321	5154	21.633	4.819	4.947	4.56	4.674	15.8
20.02	474	50	3072	2970	3001	2941	7.182	1.022	0.963	0.907	0.953	16.6
20.57	474	66	3916	3829	3885	3761	12.109	1.949	1.91	1.788	1.859	16.4
21.11	474	86	4620	4531	4619	4476	17.304	3.455	3.468	3.144	3.21	16.1
21.54	474	100	5238	5190	5299	5151	22.695	5.348	5.442	4.956	5.097	15.7
1.51	474	50	3087	3002	3041	3011	7.897	1.253	1.206	1.103	1.138	16.6
1.63	474	66	3930	3834	3891	3821	13.085	2.398	2.333	2.123	2.175	16.4
1.7	474	86	4628	4532	4601	4521	18.764	3.668	3.504	3.292	3.455	16.1
1.73	474	100	5148	5149	5244	5126	24.317	5.578	5.587	5.168	5.32	15.7
-16.32	474	50	3106	2922	2985	3028	8.171	1.186	1.059	1.01	1.122	16.6
-17.2	475	66	3947	3748	3831	3865	13.869	2.367	2.106	2.016	2.24	16.4
-17.88	475	86	4641	4432	4528	4551	19.815	4.222	3.783	3.564	3.858	16.1
-17.76	474	100	5115	5060	5178	5116	25.408	5.989	5.92	5.473	5.681	15.7
-38.76	475	50	3037	2864	2903	2934	8.806	1.284	1.168	1.042	1.131	16.6
-38.51	474	66	3881	3751	3819	3797	15.315	2.473	2.28	2.119	2.275	16.4
-38.26	474	86	4575	4466	4523	4476	21.883	4.479	4.277	3.878	4.023	16.1
-38.15	475	100	5069	5062	5139	5039	28.079	5.795	5.77	5.427	5.68	15.7

Table B.9: UAS test, 6000 m altitude - measurements

6000 m altitude - standard deviation												
t [℃]	p [mbar]	THRL [%]	Ω_1 [rpm]	Ω_2 [rpm]	Ω_3 [rpm]	Ω_4 [rpm]	T [N]	I_1 [A]	I_2 [A]	I_3 [A]	I_4 [A]	V [V]
0.04	0.2	0	20	22	20	21	0.066	0.201	0.226	0.157	0.109	0.018
0.09	0.26	0	31	33	34	30	0.096	0.166	0.196	0.139	0.092	0.015
0.17	0.27	0	45	44	43	41	0.129	0.277	0.307	0.216	0.158	0.025
0.17	0.23	0	81	45	41	52	0.126	0.233	0.269	0.175	0.122	0.019
0.15	0.13	0	16	44	25	19	0.066	0.243	0.268	0.189	0.135	0.023
0.17	0.12	0	22	39	31	36	0.09	0.208	0.225	0.159	0.118	0.018
0.14	0.14	0	72	50	41	39	0.21	0.095	0.1	0.071	0.053	0.008
0.10	0.14	0	92	68	57	43	0.199	0.164	0.154	0.113	0.077	0.021
0.03	0.12	0	14	32	72	20	0.072	0.224	0.248	0.175	0.124	0.025
0.04	0.14	0	35	41	67	35	0.212	0.177	0.192	0.151	0.123	0.02
0.02	0.15	0	84	43	44	35	0.122	0.31	0.347	0.238	0.176	0.028
0	0.14	0	95	51	65	51	0.208	0.271	0.343	0.243	0.158	0.026
0.19	0.13	0	20	25	48	19	0.078	0.204	0.226	0.162	0.123	0.016
0.28	0.19	0	33	37	84	31	0.127	0.271	0.291	0.211	0.154	0.023
0.09	0.15	0	35	38	49	42	0.186	0.2	0.216	0.154	0.127	0.016
0.14	0.14	0	58	49	70	53	0.246	0.267	0.301	0.207	0.153	0.015
0.07	0.14	0	23	41	48	28	0.095	0.167	0.173	0.13	0.1	0.017
0.08	0.12	0	26	43	123	33	0.149	0.146	0.155	0.112	0.096	0.019
0.06	0.11	0	43	48	79	36	0.227	0.224	0.226	0.178	0.119	0.012
0.01	0.15	0	50	62	82	42	0.166	0.175	0.182	0.145	0.111	0.018

Table B.10: UAS test, 6000 m altitude - standard deviation

Appendix C

Propulsion system simulation

Brushless motor implementation

```matlab
function [i,Q,P,eta] = bldc_motor_pwm(v0,pwm,rpm,R,i0,KV)
%% Electric Motor Simulation
% Author: Matteo Scanavino
% Email : matteo.scanavino@polito.it
% A.A:  : 2019-2020
%
% This function is the implementatin of the model proposed by Drela
% Details are explained in ...
     http://web.mit.edu/drela/Public/web/qprop/
%
%%% INPUT
% v0     Motor voltage        [V]
% pwm    PWM throttle signal  [-]
% rpm    Motor speed          [rpm]
% R      Motor resistance     [Ohm]
% i0     Motor idle current   [A]
% KV     Motor constant       [rpm/V]
%
%%% OUTPUT
% i      Motor current        [A]
% Q      Motor torque         [Nm]
% P      Shaft power          [W]
% eta    Motor efficiency     [-]
%
%% Performance computation
%
v    = v0*pwm;
i    = zeros(length(v),length(rpm));
Q    = zeros(length(v),length(rpm));
P    = zeros(length(v),length(rpm));
```

```matlab
30  eta = zeros(length(v),length(rpm));
31  %
32  for k = 1: length(v)
33      for j = 1: length(rpm)
34          i(k,j)   = (v(k)-rpm(j)/KV)/(R);
35          P(k,j)   = (v(k)-i(k,j)*R)*(i(k,j)-i0);
36          Q(k,j)   = P(k,j)/(rpm(j)*pi/30);
37          eta(k,j) = P(k,j)./(v(k)*i(k,j));
38      end
39  end
40  %
41  i = i'; Q = Q'; P = P'; eta = eta';
42  %
43  end
```

Blade Element Momentum Theory implementation

```matlab
1   %%%%%%% BLADE ELEMENT MOMENTUM THEORY %%%%%%%%%%%
2   %
3   % Author: Matteo Scanavino
4   % Affiliation: Politecnico di Torino
5   % A.A.: 2019-2020
6   % Contact: matteo.scanavino@polito.it
7   %
8   %%%%%%%%%%%%%%%%%%%%%%%%%%%%%%%%%%%%%%%%%%%%%%%%%%
9   %
10  clear; close all; clc;
11  %
12  %% Input data
13  rpm  = [2000 2500 3000 3500 4000 4500]';      % Motor speed  [rpm]
14  temp = -[41.630 40.617 40.176 39.853 ...
15           39.687 39.554 39.537  39.801]';  % Temperature  [°C]
16  press= [703.464 702.886 702.913 703.316 ...
17           579.220 579.184 579.148 578.769]'; % Pressure    [hPa]
18  method  = 'linear';                          % Interpolation ...
        method
19  showplt = 0;                                 % If 1 display plot
20  %
21  %% Additional data
22  dia   = 15;              % Propeller diameter        [inch]
23  xnbla = 2;               % Nuber of blade            [-]
24  nelem = 100 ;            % BET elements              [-]
25  Vel   = 0.001*ones(1,length(rpm));% Flow speed       [m/s]
26  tau   = 1E-1;            % Inflow factor convergence [-]
27  tau2  = tau;             %                           [-]
28  tol   = 1E-6;            % Tollerance inflow factor  [-]
29  itermax = 1500;          % Maximum iterations        [-]
```

108

```
30  chdRe = 0.027178;              % Chord for Reynolds coputation [m]
31  station = 0.75;                % Reference station Reynolds
32  %
33  %% Constants
34  %
35  inch2m  = 0.0254;              % Conversion factor: inch to m
36  g       = 9.81;                % Gravity                     [m/s^2]
37  t0      = 273.15;              % Temperature conversion:°C to K
38  beta    = 1.458e-6;            % Constant 1 Shuterland        [m^2/s]
39  esse    = 110.4;               % Constant 2 Shuterland        [K]
40  Rair    = 287;                 % Air specific constant        ...
        [J/(kgK)]
41  alfar   = -20:60;              % Angle of attack in database   [deg]
42  reynr   = [5E3:5E3:40E3 5E4:1E5:45E4];  % Rynolds in database ...
            [-]
43  %
44  %% Propeller geometry
45  %
46  dia     = dia * inch2m;        % Converting diameter in m     [m]
47  R       = dia /2;              % Propeller radius             [m]
48  load    tmotor_dba.mat         % Aerodynamic database         [-]
49  load    tmotor.mat             % Chord distribution           [m]
50  %                              % Twist angle distribution     [deg]
51  %
52  % Initialize meshgrid for aerodynamic CL and CD surface vs AOA ...
        and Reynolds
53  X = zeros(81,13); Y=X;
54  [X,Y] = meshgrid(alfar,reynr);
55  %
56  %% Propeller chord and twist distribution plot
57  %
58  if showplt
59      figure('Name','Prop distrib');
60      plot(rR/R,chd,'o--'); hold on;
61      grid minor; ylabel('[mm]');
62      ylim([.01 .05]); xlim([0 1.05]);
63      yyaxis right; plot(rR/R,pitch,'o--'); hold on;
64      ylabel('[deg]'); xlabel('r/R %');
65      ylim([5 23]); xlim([0 1.05]);
66      legend('Chord [mm]','Pitch [deg]');
67      title('Chord and pitch distribution');
68  end
69  %
70  %% Computation
71  %
72  rhoi = press*1E2./((temp + t0)*Rair);        % Air density   ...
        [kg/m^3]
73  mui  = beta*(temp+t0).^1.5./((temp + t0)+esse); % Aid viscoity ...
        [m^2/s]
74  %
```

```matlab
75  % Vector initalization
76  thrust_v = zeros(length(rpm),1);      % Thrust vector
77  torque_v = zeros(length(rpm),1);      % Torque vector
78  power_v  = zeros(length(rpm),1);      % Mechanical power vector
79  ct_v    = zeros(length(rpm),1);       % Thrust coefficient vector
80  cq_v    = zeros(length(rpm),1);       % Torque coefficient vector
81  beta_r = zeros(length(rpm),nelem);    % Propeller twist vector
82  chd_r  = zeros(length(rpm),nelem);    % Propeller chord vector
83  phi_r  = zeros(length(rpm),nelem);    % Inflow vector
84  alfa_r = zeros(length(rpm),nelem);    % Angle of Attack vector
85  a_r    = zeros(length(rpm),nelem);    % Coefficient a vector
86  b_r    = zeros(length(rpm),nelem);    % Coefficient b vector
87  rey_r  = zeros(length(rpm),nelem);    % Reynolds vector
88  cl_r   = zeros(length(rpm),nelem);    % Lift coefficient vector
89  cd_r   = zeros(length(rpm),nelem);    % Drag coefficient vector
90
91  fprintf('Blade Element Momentum Theory\n')
92  fprintf('T-motor CF 15''x5''\n')
93  fprintf('Temperature \t= \t\t%0.f\t\t[°C]\n',temp)
94  fprintf('Pressure \t\t= \t\t%.0f\t\t[mabr]\n',press)
95  fprintf('Air density \t= \t\t%.3f\t[kg/m^3]\n',rho);
96  fprintf('\t\t-----\n')
97
98  %
99  for i = 1:length(rpm)
100     fprintf('Processing RPM = %.0f\t',rpm(i));
101     xs   = 0.15*R;                    % Lower bound integration [m]
102     B    = 1 - chd(end)/(2*R);
103     xt   = B*R;                       % Upper bound integration  [m]
104     rstep= (xt-xs)/nelem;             % Integration step         [m]
105     omega= rpm(i)/60*2*pi;            % Motor angular rate       ...
                [rad/s]
106     rl   = linspace(xs,xt,nelem);    % Propeller discretization [m]
107     thrust = 0;                       % Initial thrust value     [N]
108     torque = 0;                       % Initial torque value     [Nm]
109     vel    = Vel(i);                  % Flow speed               [m/s]
110     rho    = rhoi(i);                 % Air density              ...
                [kg/m^3]
111     mu     = mui(i);                  % Air viscosity            ...
                [m^2/s]
112
113     % BET loop
114     for j = 1:nelem
115
116         rad   = rl(j);                % Radial distance from hub   ...
                   [m]
117         chord = interp1(rR,chd,rad);  % Local chord                ...
                   [m]
118         theta = interp1(rR,pitch,rad);% Local twist                ...
                   [deg]
```

```
119            chd_r(i,j)  = chord;
120            beta_r(i,j) = theta;
121            theta   = deg2rad(theta);      % Twist conversion: deg to rad
122            a = 0.1;                       % Inflow coefficient a ...
                  initalization
123            b = 0.01;                      % Inflow coefficient b ...
                  initialization
124            isum        = 1;               % Counter initialization
125            finished    = 0;               % Control flag initialization
126
127            while (finished == 0)
128                v0          = vel*(1+a);            % Axial speed      ...
                      [m/s]
129                v2          = omega*rad*(1-b);      % Radial speed     ...
                      [m/s]
130                phi         = atan2(v0,v2);         % Inflow angle     ...
                      [rad]
131                alfa        = theta - phi;          % Angle of attack ...
                      [rad]
132                vlocal      = sqrt(v0^2+v2^2);      % Local speed      ...
                      [m/s]
133                relocal     = rho*vlocal*chord/mu;  % Local reynolds   ...
                      [-]
134
135                if(relocal<reynr(1))
136                    relocal = reynr(1);
137                    elseif (relocal>reynr(end))
138                    relocal = reynr(end);
139                end
140
141                if(rad2deg(alfa)<alfar(1))
142                    alfa = deg2rad(alfar(1));
143                elseif (rad2deg(alfa)>alfar(end))
144                    alfa = deg2rad(alfar(end));
145                end
146
147                % Lift and drag coefficient interpolation
148                cl = interp2(X,Y,tmotor_cl',rad2deg(alfa),   ...
149                          relocal,method);                       % Javafoil
150                cd = interp2(X,Y,tmotor_cd',rad2deg(alfa),   ...
151                          relocal,method);                       % Javafoil
152
153                % tip correction factor
154                f    = xnbla/2*(R-rad)/(rad*sin(phi));
155                F    = 2/pi*acos(exp(-f));
156
157                % Blade element thrust and torque
158                dtdr = xnbla*0.5*rho*vlocal^2*chord*     ...
159                        (cl*cos(phi)-cd*sin(phi));
160                dqdr = xnbla*0.5*rho*vlocal^2*chord*     ...
```

```
161                    (cd*cos(phi)+cl*sin(phi))*rad;
162
163               % Convergence
164               tem1 = dtdr/(4*pi*rad*rho*vel^2*(1+a)*F);
165               tem2 = dqdr/(4*pi*rad^3*rho*vel*(1+a)*omega*b*F);
166
167               anew = a*(1-tau)+tem1*tau;
168               bnew = b*(1-tau2)+tem2*tau2;
169
170               if(abs(anew-a)<tol) && (abs(bnew-b)<tol)
171                   finished = 1;
172               else
173                   if isum < itermax
174                       a     = anew;
175                       b     = bnew;
176                       isum = isum +1;
177                   else
178                       fprintf('iter max!\n')
179                       return
180                   end
181               end
182           end
183
184           a_r(i,j) = a;
185           b_r(i,j) = b;
186           alfa_r(i,j) = rad2deg(alfa);
187           phi_r(i,j)  = rad2deg(phi);
188           rey_r(i,j)  = relocal;
189           cl_r(i,j)   = cl;
190           cd_r(i,j)   = cd;
191           corr_f(i,j)   = F;
192           thrust = thrust+dtdr*rstep;
193           torque = torque+dqdr*rstep;
194           fprintf('.');
195       end
196
197       thrust_v(i,1) = thrust;
198       torque_v(i,1) = torque;
199       power_v(i,1)  = torque*omega;
200       ct_v(i,1)      = thrust/(0.5*rho*(rpm(i)/60)^2*dia^4);
201       cq_v(i,1)      = torque/(0.5*rho*(rpm(i)/60)^3*dia^5);
202
203       fprintf('\n');
204       clear thrust torque
205   end
206
207   rey = rhoi.*(rpm*pi/30*dia/2*station)*chdRe./mui;
208
209   % Display results
210   T = table(temp,press,rhoi,rpm,thrust_v,        ...
```

```
211                torque_v , power_v , ct_v , cq_v , rey )
212
213  if ( showplt )
214       figure ( 'Name' , 'Performance' )
215       yyaxis  left
216       plot ( rpm , thrust_v , 's - - ' ) ; hold  on ;
217       ylabel ( 'Thrust  [N] ' )
218       yyaxis  right
219       plot ( rpm , torque_v , 'd - - ' ) ;  grid  on ;
220       ylabel ( 'Torque  [Nm] ' ) ;  xlabel ( 'Motor  speed  [rpm] ' ) ;
221  end
```

Appendix D

Indoor navigation sensors

The feasibility of multicopter UAS flight inside terraXcube test section was evaluated as a possible scenario in addition to the single rotor and full vehicle performance test. Free flights of UAS inside would allow to understand the impact of extreme environments on flight qualities as in real operations. In this context, standard procedures are required to compare different vehicles. A possible solution is to perform autonomous flights without pilot intervention such as hover and waypoint navigation. Moreover, to assess vehicle performance as for real flights the onboard sensors and UAS architecture should be the same as in conventional operations. When operating in indoor environments, autonomous or automatic flights pose challenges related to the navigation module due to attenuation or reflection of Global Navigation Satellite System (GNSS) signals. According to [63] and [66], indoor environments may result in GNSS signal attenuation up to $20 - 30$dB compared to outdoor owing to multi-paths or signal reflections due to wall and furniture influence. Furthermore, autonomous indoor navigation relies on higher accuracy level, usually within few centimetres compared to common outdoor navigation requirements.

Considering terraXcube simulator, there are mainly two challenges related to autonomous indoor navigation. Firstly, the remote control of the UAS from the control room is mandatory as the pilot is not authorized to access the test section. The limited field of view from the control room requires to strongly rely on autonomous flight modes and in turn on robustness of the navigation module, with high accuracy and low latency. The second challenge is to find a suitable sensor in order to minimize any alteration and adjustment of the onboard avionics compared to the equipments used during outdoor operations. Provided the fact that GNSS sensors cannot be leveraged, other devices able to work in extreme environments and to easily communicate with autopilot boards are required.

In the following Appendix, details on testing of navigation system for autonomous indoor flight og UAS multicopter are provided. Different sensor solutions and architectures are detailed with their advantages and limitations. Autonomous indoor flight test in terraXcube still remains an open research topic to be investigated.

Motion Capture Systems

Among all sensors, motion capture systems (MoCap) are suitable solutions for precision position and attitude (pose) estimate. MoCap systems have been extensively used in several research fields and for recreational purposes as well [15, 29, 69]. The high precision and accuracy of optoelectronic MoCap systems [33, 71], such as Optitrack and Vicon, are responsible for their popularity in many UAV laboratories. The working principle is based on passive markers installed on the moving object. A set of infra-red cameras send out pulsed lights reflected by the markers and detected by the cameras. Given marker positions in perspective of several cameras, position and attitude of the object to be tracked are computed by a ground computer station. Several elements can be tracked at the same time using different marker configuration (shape) for each object. Conventional MoCap systems suffers important drawbacks: the expensive costs make these sensors unaffordable for small research laboratories; furthermore a systematic calibration tracking area is require to ensure accuracy and precision performance.

Otus Tracker

The Otus Tracker is a low cost motion capture system for UAV indoor navigation and robotic applications provided by RCBenchmark [95]. The position estimate provided by this sensor is based on HTC Vive laser beam technology which is a virtual reality system developed for full immersive gaming experience. The Otus Tracker consists of two IR light emitters (HTC Vive Base Stations) and an onboard tracker. The light emitters are actually passive elements as they do not have any information on the tracker position, which is the active component of the system. The tracker includes photo-diodes to grab the IR-light and an Inertial Measurement Unit. The pose is computed combining inertial data from the IMU and light detected by the photo-diodes leveraging *Angle-of-Arrival* algorithms. Each Base Station provides two light signals: a synchronization pulse is generated by an IR-led matrix emitter, while permanent magnet synchronous motors spin optical flywheels and control the lens system to generate laser beam lines. The photo-diodes installed in the trackers are essentially switchers that are activated when a sufficient amount of energy is captured by Base Station light emission. When the synchronization pulse flashes the tracker, all the timers are simultaneously set to zero. Then the sweep horizontal and vertical laser beams are generated by the base stations: when the tracker photo-diodes are illuminated by the beams, trigger signals are sent to evaluate the time interval between the synchronization signal and the laser beam detection. Given the angular speed of the beam and the time interval of each photo-diodes, the angle between the base-station normal vector and the photo-diode is computed. Combining light signals from different photo-diodes it is possible to compute the tracker pose and update the estimate provided by the IMU. The MoCap system for multirotor autonomous flight is shown in Figure D.1 where the IR emitter is in red, the onboard tracker in orange and the onboard companion computer in green.

IMU and photo-diodes signals are sent from the onboard tracker to the ground station wirelessly; a dedicated software in the ground computer is in charge of the position and attitude computation. The pose data is sent back to the UAS leveraging a WiFi connection between the ground station and a companion computer (Raspberry Pi 3+). Finally, Mavlink is used to feedback pose data to the autopilot board (Pixhawk Cube).
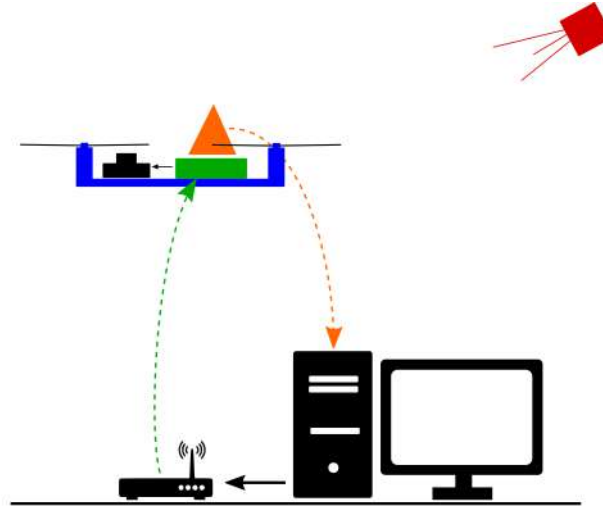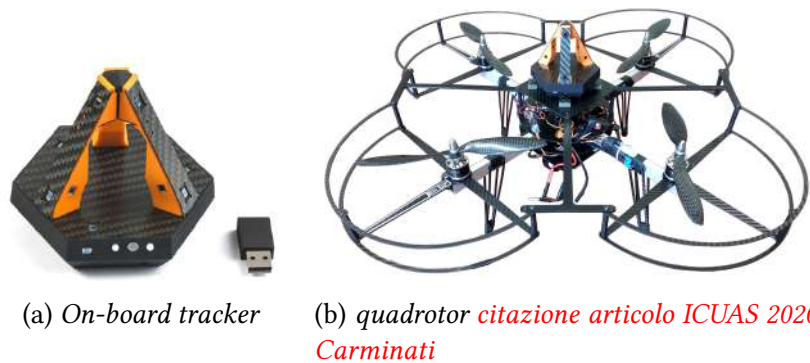

Figure D.1: Otus Tracher MoCap system architecture

(a) *On-board tracker*   (b) *quadrotor citazione articolo ICUAS 2020 Carminati*

Figure D.2: Onboard sensor and quadrotor for Otus Tracker testing

Several flight tests were performed to check the performance of the system and point out its limitations. First of all, static tests prove the precision of the system is closed to 1 mm. To this end, 9 x-y positions have been logged at 3 different altitudes (Figure D.3) for 30 seconds within the available tracking volume of 2.5 m x 2 m x 4 m (L x W x H). The corresponding precision of each position provided by the Otus (Figure D.4) is closed to 1 mm (in accordance with the sensor data-sheet) with the best values inside the core of the volume where the IR lights from the two opposite Base Stations are overlapped (precision lower than 1 mm).

Flight tests were accomplished in Altitude and Loiter Mode using a quadrotor vehicle and a PixHawk Cube Autopilot. In Loiter Mode, if no commands are given by the pilot, the UAS attempts to keep the current position and heading (hovering); when the pilot provides command through the RC, the autopilot follows the computed desired position while the throttle controls the vertical speed. Figure D.5 shows the performance of the MoCap in Loiter Mode. After take-off, the UAS is hovering; then the multicopter is controlled along a cross in the NED reference X and Y axes at constant altitude. Unfortunately, flight tests highlighted the onboard sensor is strongly sensitive to mechanical vibrations and light conditions which result in unstable position estimate and glitches (Figure D.6a). According to the manufacturer, mechanical vibrations, WiFi network interference and IR reflections are the primary causes low tracking performance. Despite the designed damping system in Figure D.6b, random track loosing were experienced in other indoor flight tests.
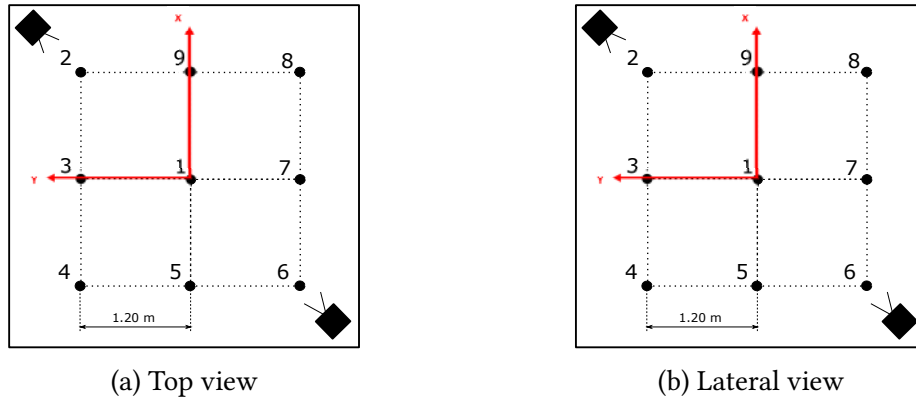

(a) Top view (b) Lateral view

Figure D.3: Tracked volume for precision test

Compared to camera-based tracking solutions (i.e. Vicon and Optitrack), the Otus Tracker MoCap system provides a relatively easy set-up. This is achieved by the integration with common open-source autopilot boards (i.e. PX4) as well as plug-in for multiple programming languages such as Python and Matlab. Furthermore, the HTC Vive technology leveraged by Otus does not require calibration of the flight area, resulting in higher flexibility and simplified procedures. More in general, Base Stations can be easily relocated so that the system is scalable to user needs. On the other hand, some important limitations are highlighted compared to conventional MoCap systems (i.e.). The onboard marker used by Optitrack and Vicon MoCap (i.e. Figure D.10) is lighter and works as a passive element. On the other hand, the Otus requires 5 V power supply and its weight is heavier with respect to passive markers. Moreover, camera-based tracking systems offer higher tracking resolution, usually 0.1 mm compared to 0.5 mm of Otus, and more resilience to mechanical vibrations and Radio Frequency.
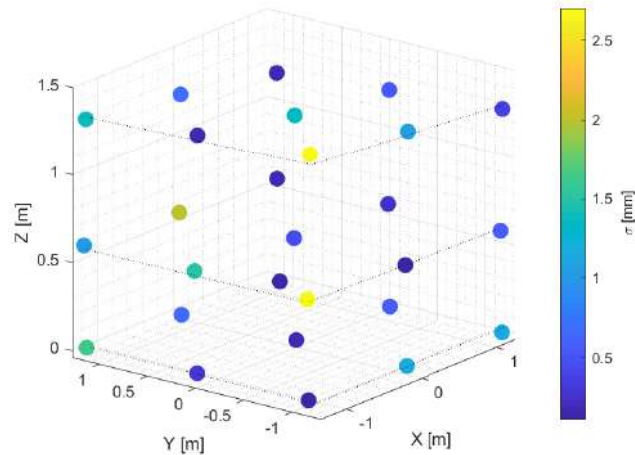
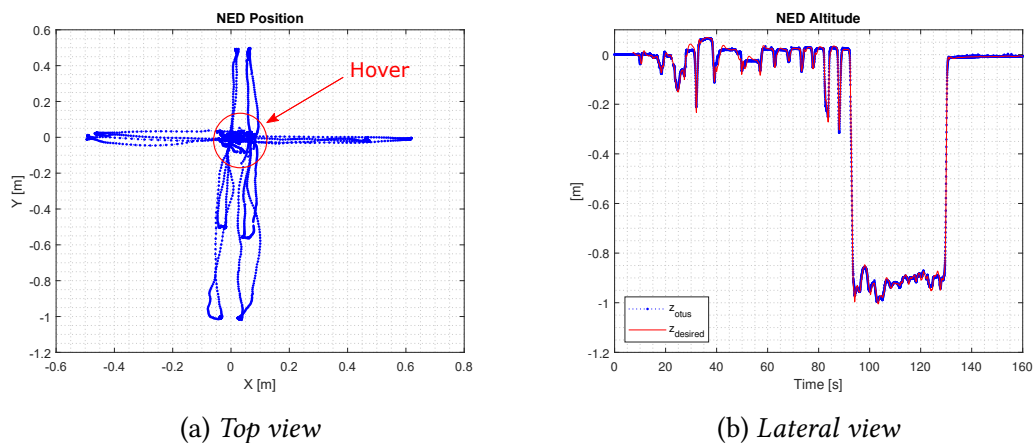Figure D.4: Otus tracker precision test - Standard deviation at different positions

(a) *Top view*

(b) *Lateral view*

Figure D.5: Flight test in Loiter Mode

Ultrasonic Indoor Positioning

Marvelmind Robotics

Marvelmind Robotics provides an indoor navigation system for robotic applications. The ultrasonic sensor kit [97] consists of fixed receivers and a mobile beacon (referred to as hedge-beacon) equipped with an ultrasonic emitter and an Inertial Measurement Unit (IMU). The hedge beacon position is triangulated given the distances to each stationary beacons and their location in a world reference frame. This is done by transmitting an ultrasound signal from the mobile beacon. The distance between the hedge beacon and the each stationary module is evaluated given the time lag between emission and reception. All the time lags are sent to a ground computer to perform the

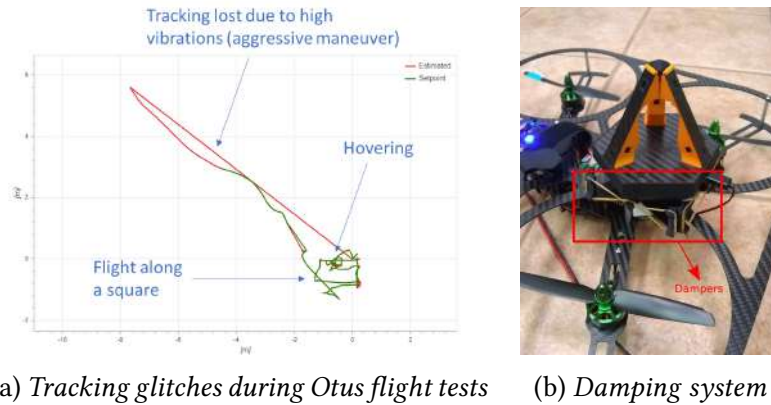(a) *Tracking glitches during Otus flight tests*   (b) *Damping system*

Figure D.6: Otus glitches and mechanical vibration damping system

triangulation algorithms and define the absolute position of the mobile sensor. A dedicated router is in charge to transmit the computed position to the onboard module to provide feedback (position, velocity and attitude) to the autopilot. The communication link between stationary beacons, hedge beacon and the router is based on radio frequency signal with carrier working at 433MHz.

The navigation system was tested with the quadrotor vehicle in Figure 4.8 equipped with a PixHawk Cube autopilot and ArduCopter firmware. Preliminary tests were performed in the UAV Laboratory at the Department of Mechanical and Aerospace Engineering at Politecnico di Torino. The small flight area measures 2.5m x 2m x 3m (L x W x H) and the stationary beacons were installed along the laboratory walls. A North-East-Down (NED) inertial reference frame was established for all the tests and standard GPS NMEA 173 messages were leveraged to manage the communication between the hedge beacon and the autopilot via UART port. To assess the capabilities of Marvelmind system, the vehicle was placed in the test area, connected to a ground control station via telemetry and manually controlled using the RC. The flight mode leveraged was *Loiter Mode.*

Figure D.7 shows pilot commands during the tests: no pilot intervention occurs between 15s and 30s so that the vehicle should maintain its hover position. This is confirmed by the desired positions computed by the autopilot in Figure for both N-S and E-W directions. However, the position estimated by the Extended Kalman Filter (EKF) clearly shows an unstable behaviour with oscillations of increasing amplitudes (Figure D.8). An intensive test campaign was conducted to evaluate the different system configurations but unfortunately any stable and controlled flight was not possible without understanding causes of these behaviours. Moreover, the influence of radio-frequency signals between the telemetry and Marvelmind router (both working at the same frequency) has been considered and it was found that operations without the telemetry result in more stable signals from Marvelmind system, as depicted in Figure D.9.

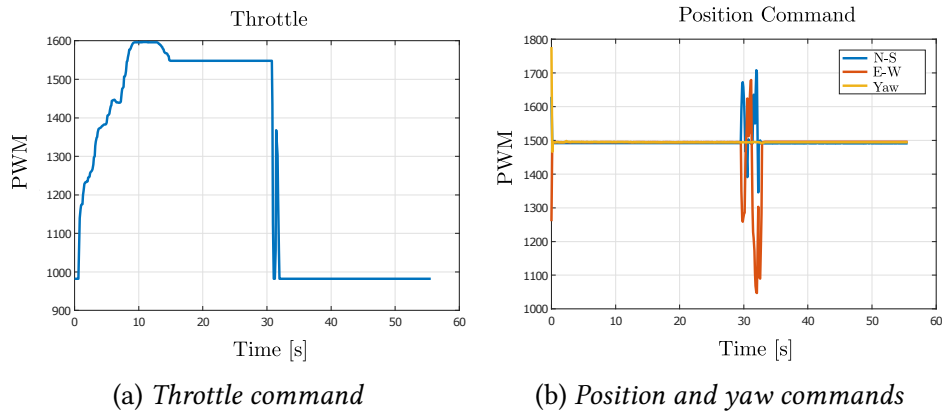Several flight tests were performed in collaboration with the Department of Aerospace

(a) *Throttle command* (b) *Position and yaw commands*

Figure D.7: Pilot commands during Marvelmind indoor test in Loiter Mode

(a) *North - South position* (b) *East - West position*
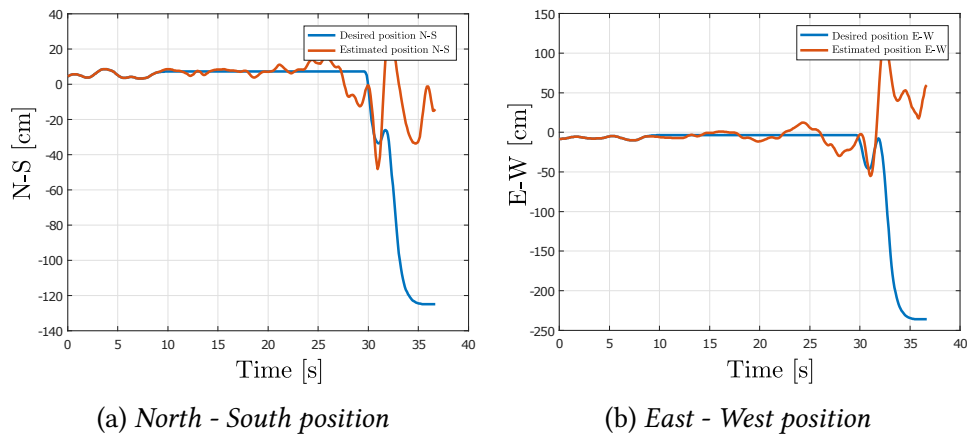
Figure D.8: Desired and actual positions during Marvelmind indoor test in Loiter Mode
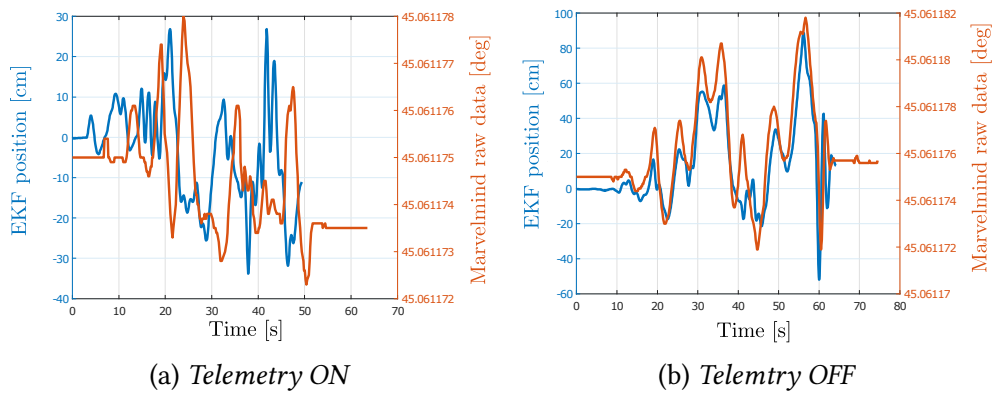

(a) *Telemetry ON* (b) *Telemtry OFF*

Figure D.9: Autopilot EKF position estiamte and Marvelmind raw data

Science and Technology of Politecnico di Milano [56] where an Optitrack Motion Capture system is available for autonomous UAS navigation [37]. This laboratory offers

a wide test area (5x5x5 m) with a cage for UAS flight and eight cameras on the top for tracking purposes. Reflective markers were installed on the quadrotor; at the same time the Marvelmind hedge beacon was placed in the bottom of the airframe (Figure D.10) while the stationary ultrasonic anchors were set on the floor. The raw data of the OptiTrack were processed by a rotation matrix in order to align the position with the reference frame of Marvelmind system. In this way, OptiTrack provided a true reference pose while Marvelmind was used to provide pose feedback to the autopilot board. The copter was flown in Loiter Mode with limited pilot intervention to check the hovering performance.

The altitude offset in Figure D.11b is caused by the relative distance between the two onboard sensors (reflective marker on the top, while the ultrasonic beacon on the bottom). However, an offset reversion is experienced when the UAS is landing. According to the manufacturer, this is caused by the low accuracy of the Marvelmind system when the mobile beacon is in proximity with the anchor plane. In general, when flying the UAS the accuracy of the Marvelmind appears to be lower than the declared static accuracy of 2 cm. As an example, a position error of 33 cm in the North position is highlighted in Figure D.11c; similar trend were found during all the tests. According to the manufacturer, possible causes of this behaviour are related to Marvelmind sensitivities to attitude, noise and disturbance.

Figure D.10: UAS with Marvelmind beacon and optical marker for motion tracking

Visual Interial Odometry

Realsense D435i Depth Camera

Position and attitude of a robotic platform (ground or aerial vehicles) can be estimated leveraging Visual Inerial Odoemtry algorithm which combine image from dedicated

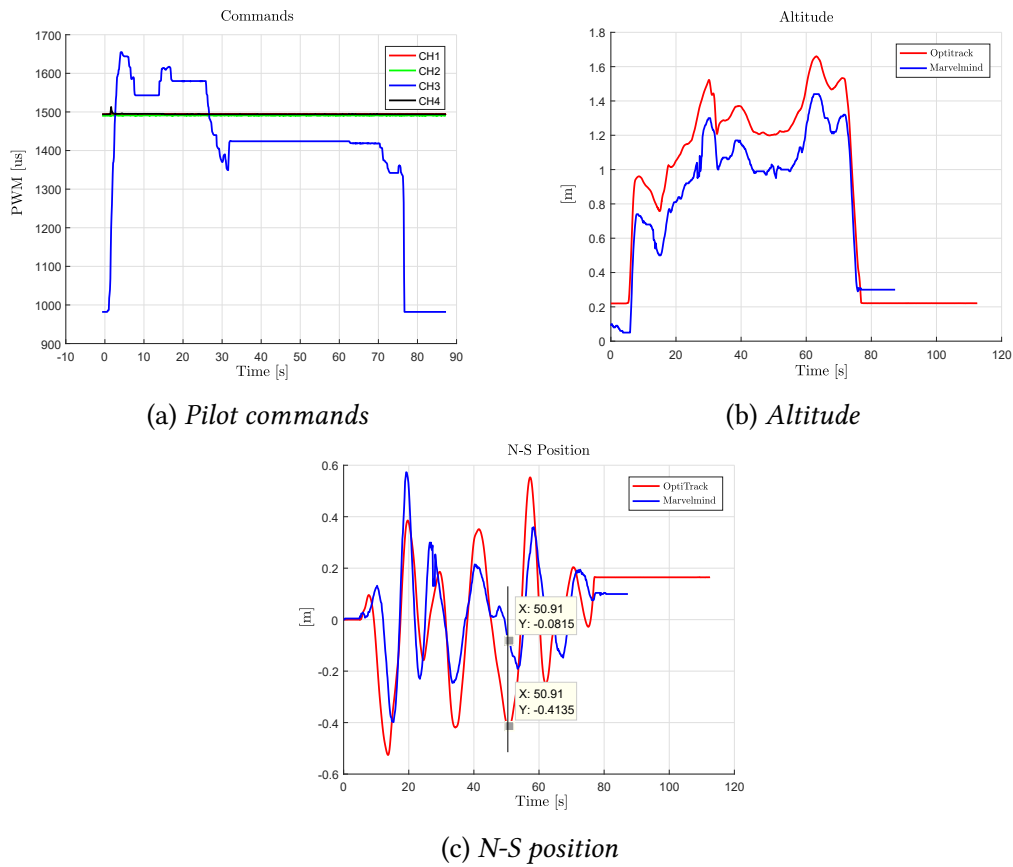(a) *Pilot commands*

(b) *Altitude*

(c) *N-S position*

Figure D.11: Pilot commands and altitude during indoor test in Politecnico di Milano

cameras and IMU data attached to it. Accoring to [102], «VIO is the only viable a viable alternative to GPS and lidar-based odometry to achieve accurate state estimation». Features from input images are extracted in order to evaluate the pose displacement. An onboard IMU is leveraged to increase pose estimate integrating accelerometer and gyroscope readings.

The Realsense D435i Depth Camera combines two depth IR sensors, an RGB camera and an integrated IMU sensor. The output provided by the D435i consist of a point cloud depth image and additionally IMU data as well as coloured camera frames. The tracking capability of the sensor was tested using the ground robot in Figure D.12. As the sensor does not provide pose data on its own, an dedicated companion computer is needed to process sensor data and estimate the position. The *LattePanda Delta* computer was used to this end; the Robot Operating System (ROS) was leveraged to manage the sensor and compute the position based on Real-Time Appearance-Based Mapping (RTAB-Map) [23, 54].

The overall sensor architecture consists of the following ROS node:

- real-sense: this module handle the D435i sensor, including management of camera settings;

- imu-filter: it is responsible for attitude estimate based on Madgwick algorithm [62]. This module is used to fuse raw data from IMU (angular velocities, accelerations and optionally magnetic readings) in order to compute an orientation quaternion;

- rtabmap: the RGB-D stereo SLAM;

- robot-localization: it provides non-linear state estimation (Extended Kalman Filter) through sensor fusion of an arbitrary number of sensors.
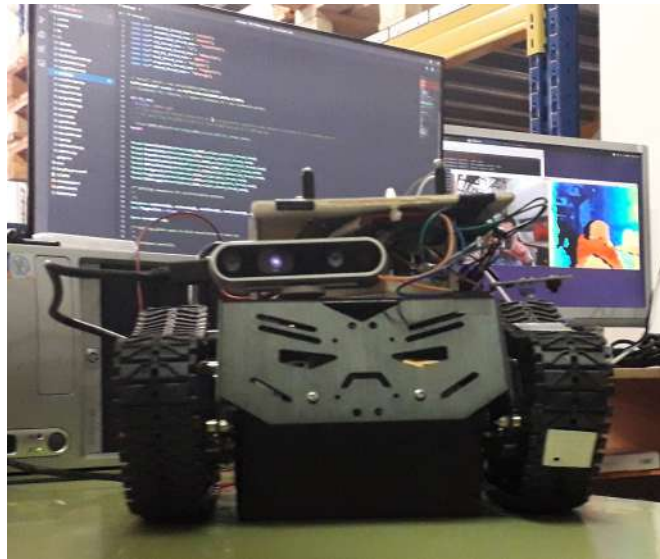

Figure D.12: Realsense D435i onboard a ground robot for testing

Preliminary tests showed the capability of the depth sensor combined to an IMU to track the position and attitude of the robot. While the aforementioned architecture is prominent, important drawbacks were experienced. Firstly, featureless environments resulting from uniform texture scenes (i.e. white walls); unless enough features, the VIO is not able to compute the odometry. Secondly, fast camera motions as a consequence of unreliable attitude estimate from IMU and difficulty to match features between successive frames. High quality robot position estimate required slow movements and enough features to be extracted by the RTAB-Map software; even tough the D435i sensor is designed to for depth point cloud purposes, the integrated IMU allow promising VIO estimates. However, more reliable sensor solutions are possible such as the Intel Realsense T265 tracking camera; as reported in [1] its low weight and pose estimation ability.

Bibliography

[1]   Ankit Agarwal, Jacob R Crouse, and Eric N Johnson. "Evaluation of a Commercially Available Autonomous Visual Inertial Odometry Solution for Indoor Navigation." In: *2020 International Conference on Unmanned Aircraft Systems (ICUAS)*. IEEE. 2020, pp. 372–381.

[2]   John Anderson. *Fundamentals of Aerodynamics*. 6th Edition. New York City: McGraw-Hill Education, 2017.

[3]   Michele Arra. *L'elicottero*. Hoepli Editore, 2001.

[4]   Arrigo Avi. "Development of icing testing tools for large climatic chamber." PhD thesis. Politecnico di Milano, 2020.

[5]   Bob Balaram et al. "Mars helicopter technology demonstrator." In: *2018 AIAA Atmospheric Flight Mechanics Conference*. 2018, p. 23.

[6]   Jacob Baranski et al. "Characterization of Propeller Performance and Engine Mission Matching for Small Remotely Piloted Aircraft." In: *47th AIAA / ASME / SAE / ASEE Joint Propulsion Conference & Exhibit*. 2011, p. 6058.

[7]   Engin Baris, Colin P Britcher, and George Altamirano. "Wind Tunnel Testing of Static and Dynamic Aerodynamic Characteristics of a Quadcopter." In: *AIAA Aviation 2019 Forum*. 2019, p. 2973.

[8]   Jewel B Barlow, William H Rae, and Alan Pope. *Low-speed wind tunnel testing*. John wiley & sons, 1999.

[9]   Tadas P Bartkus, Peter M Struk, and Jen-Ching Tsao. "Comparisons of mixed-phase icing cloud simulations with experiments conducted at the NASA propulsion systems laboratory." In: *9th AIAA Atmospheric and Space Environments Conference*. 2017, p. 4243.

[10]   Anthony Robert Southey Bramwell, David Balmford, and George Done. *Bramwell's helicopter dynamics*. Elsevier, 2001.

[11]   John Brandt and Michael Selig. "Propeller performance data at low reynolds numbers." In: *49th AIAA Aerospace Sciences Meeting including the New Horizons Forum and Aerospace Exposition*. 2011, p. 1255.

[12] John Burton Brandt. "Small-scale propeller performance at low speeds." PhD thesis. University of Illinois at Urbana-Champaign, 2005.

[13] Manuel Carreno Ruiz et al. "Experimental and numerical analysis of multicopter rotor aerodynamics." In: *2021 AIAA Aviation Forum and Exposition.* AIAA. 2021, pp. 1–4.

[14] Raymond Castner. "High altitude small engine test techniques at the NASA glenn propulsion systems LAB." In: *22nd AIAA Aerodynamic Measurement Technology and Ground Testing Conference.* 2002, p. 2922.

[15] Kevin Chang et al. "Motion Capture Control of a Nano Quadrotor." In: *15th LACCEI International Multi-Conference for Engineering, Education, and Technology.* LACCEI. 2017, pp. 1–6.

[16] IC Cheeseman and WE Bennett. "The effect of the ground on a helicopter rotor." In: *R & M* 3021 (1957).

[17] Hugh W Coleman and W Glenn Steele. *Experimentation, validation, and uncertainty analysis for engineers.* John Wiley & Sons, 2018.

[18] Sarah Ann Conley. "Design of the Multirotor Test Bed for Load and Acoustic Measurements." PhD thesis. University of California, Davis, 2019.

[19] Stephen A Conyers, Matthew J Rutherford, and Kimon P Valavanis. "An empirical evaluation of ceiling effect for small-scale rotorcraft." In: *2018 International Conference on Unmanned Aircraft Systems (ICUAS).* IEEE. 2018, pp. 243–249.

[20] Stephen A Conyers, Matthew J Rutherford, and Kimon P Valavanis. "An empirical evaluation of ground effect for small-scale rotorcraft." In: *2018 IEEE International Conference on Robotics and Automation (ICRA).* IEEE. 2018, pp. 1244–1250.

[21] Stephen Austin Conyers. "Empirical Evaluation of Ground, Ceiling, and Wall Effect for Small-Scale Rotorcraft." PhD thesis. University of Denver, 2019.

[22] Reed Danis. "Investigating Forward Flight Multirotor Wind Tunnel Testing in a 3-by 4-foot Wind Tunnel." MA thesis. California Polytechnic State University, 2018.

[23] Sagarnil Das. "Simultaneous Localization And Mapping (SLAM) using RTAB-Map." In: *arXiv preprint arXiv:1809.02989* (2018).

[24] Robert Deters. "Performance and slipstream characteristics of small-scale propellers at low Reynolds numbers." PhD thesis. University of Illinois at Urbana-Champaign, 2014.

[25] Robert Deters and Michael Selig. "Static testing of micro propellers." In: *26th AIAA applied aerodynamics conference.* 2008, p. 6246.

[26]   Robert W Deters, Gavin Kumar Ananda Krishnan, and Michael S Selig. "Reynolds number effects on the performance of small-scale propellers." In: *32nd AIAA applied aerodynamics conference*. 2014, p. 2151.

[27]   Emilio Dicembrini et al. "Modelling and simulation of a tethered UAS." In: *2020 International Conference on Unmanned Aircraft Systems (ICUAS)*. IEEE. 2020, pp. 1801–1808.

[28]   DB Dill et al. "Work capacity in acute exposures to altitude." In: *Journal of applied physiology* 21.4 (1966), pp. 1168–1176.

[29]   Guillaume Ducard and Raffaello D'Andrea. "Autonomous quadrotor flight using a vision system and accommodating frames misalignment." In: *2009 IEEE International Symposium on Industrial Embedded Systems*. IEEE. 2009, pp. 261–264.

[30]   E+E Elektronik. *Specification sheet E211 sensor*. 2019. URL: http://www.epluse-us.com/en/products/humidity-instruments/humidity-transmitters-for-hvac-applications/ee211/ (visited on 05/06/2020).

[31]   John V Foster et al. "Recent NASA Wind Tunnel Free-Flight Testing Of A Multirotor Unmanned Aircraft System." In: *AIAA Scitech 2020 Forum*. 2020, p. 1504.

[32]   FreeflySystem. *Alta 8 Aircraft Fligth Manual*. English. Version 770-00048, Revision B. 2017.

[33]   Joshua S Furtado et al. "Comparative Analysis of OptiTrack Motion Capture Systems." In: *Advances in Motion Sensing and Control for Robotic Applications*. Springer, 2019, pp. 15–31.

[34]   Dustin Gamble and Andrew Arena. "Automated dynamic propeller testing at low Reynolds numbers." In: *48th AIAA Aerospace Sciences Meeting Including the New Horizons Forum and Aerospace Exposition*. 2010, p. 853.

[35]   Giancarlo Genta. *Meccanica dell'autoveicolo, Collana di Progettazione e Costruzione delle Macchine*. 1993.

[36]   R Gigacz et al. "Developing a Stable Small UAS for Operation in Turbulent Urban Environments." In: *International Micro Air Vehicle Conference and Flight Competition (IMAV) 2017*. 2017, pp. 184–189.

[37]   Mattia Giurato. "Design, integration and control of multirotor UAV platforms." PhD thesis. Italy, 2020.

[38]   Andrew Gong, Rens MacNeill, and Dries Verstraete. "Performance testing and modeling of a brushless dc motor, electronic speed controller and propeller for a small uav application." In: *2018 Joint Propulsion Conference*. 2018, p. 4584.

[39]   George Gregory IV et al. *Acoustic Testing of Five Multicopter UAS in the U.S. Army's 7- by 10- Foot Wind Tunnel*. NASA Ames Research Center, Aeromechanics Office, 2018.

[40] Ohad Gur and Aviv Rosen. "Optimizing electric propulsion systems for unmanned aerial vehicles." In: *Journal of aircraft* 46.4 (2009), pp. 1340–1353.

[41] Richard Hann. *UAV Icing: Ice Accretion Experiments and Validation.* Tech. rep. SAE Technical Paper, 2019.

[42] Xiaowei He and David R. Williams. "Unsteady Aerodynamic Loads on a UAS Model during a Pitch Maneuver with Roll." In: *AIAA Scitech 2020 Forum.* 2020, p. 0822.

[43] Martin Hepperle. *JAVAFOIL user's guide.* 2011. URL: www.mh-aerotools.de/airfoils/java/JavaFoil%5C%20Users%5C%%2020Guide.pdf (visited on 05/04/2020).

[44] Harry H. Heyson. *Wind Tunnel Wall Effects at Extreme Force Coefficients.* Tech. rep. NASA Langley Research Center, 1967.

[45] Edward Lewis Houghton and Peter William Carpenter. *Aerodynamics for engineering students.* Elsevier, 2003.

[46] Shubham Jain, Nekkanti Sitaram, and Sriram Krishnaswamy. "Effect of Reynolds number on aerodynamics of airfoil with Gurney flap." In: *International Journal of Rotating Machinery* 2015 (2015).

[47] Han-Yun Jhang et al. "Experimental Studies of Electronics Cooling Capabilities at High Altitude." In: *Journal of Microelectronics and Electronic Packaging* 16.2 (2019), pp. 84–90.

[48] Chung Jindeog et al. "Wind tunnel test of an unmanned aerial vehicle (UAV)." In: *KSME international journal* 17.5 (2003), pp. 776–783.

[49] Eric Johnson and Jamey Jacob. "Development and testing of a gust and shear wind tunnel for NAVs and MAVs." In: *47th AIAA aerospace sciences meeting including the new horizons forum and aerospace exposition.* 2009, p. 64.

[50] Wayne Johnson. *Rotorcraft aeromechanics.* Vol. 36. Cambridge University Press, 2013.

[51] Brian K Jones et al. *NASA Plum Brook Station In-Space Propulsion Facility Test Stand Characterization Hot Fire Test.* Tech. rep. NASA, 2018.

[52] Parimal Kopardekar et al. *Unmanned aircraft system traffic management (UTM) concept of operations.* Tech. rep. NASA, 2016.

[53] F. Quagliotti L.Lorefice B. Pralio. "Fluorescent Oil Flow Visualization Technique Applied to 2D Airfoils At Very Low Reynolds Numbers." In: *11th International Symposium on Flow Visualization.* Springer. 2004.

[54] Mathieu Labbé and François Michaud. "RTAB-Map as an open-source lidar and visual simultaneous localization and mapping library for large-scale and long-term online operation." In: *Journal of Field Robotics* 36.2 (2019), pp. 416–446.

[55] Gordon J Leishman. *Principles of helicopter aerodynamics with CD extra*. Cambridge university press, 2006.

[56] Yuntian Li et al. "A novel distributed architecture for UAV indoor navigation." In: *Transportation research procedia* 35 (2018), pp. 13–22.

[57] Yang Liu et al. "An experimental study of surface wettability effects on dynamic ice accretion process over an UAS propeller model." In: *Aerospace Science and Technology* 73 (2018), pp. 164–172.

[58] Yang Liu et al. "An experimental study on the aerodynamic performance degradation of a UAS propeller model induced by ice accretion process." In: *Experimental Thermal and Fluid Science* 102 (2019), pp. 101–112.

[59] Yang Liu et al. "Experimental investigation on the dynamic icing process over a rotating propeller model." In: *Journal of Propulsion and Power* 34.4 (2018), pp. 933–946.

[60] Emil Ljungskog. "Investigations of Flow Conditions in an Automotive Wind Tunnel." PhD thesis. Chalmers Tekniska Hogskola (Sweden), 2017.

[61] EA Lomonova. "A system look at electromechanical actuation for primary flight control." In: *Series 03: Control and Simulation 02* (1997).

[62] Sebastian Madgwick. "An efficient orientation filter for inertial and inertial/-magnetic sensor arrays." In: *Report x-io and University of Bristol (UK)* 25 (2010), pp. 113–118.

[63] Luca Mainetti, Luigi Patrono, and Ilaria Sergi. "A survey on indoor positioning systems." In: *2014 22nd international conference on software, telecommunications and computer networks (SoftCOM)*. IEEE. 2014, pp. 111–120.

[64] Mojtaba Dehghan Manshadi. "The importance of turbulence in assessment of wind tunnel flow quality." In: *Wind Tunnels and Experimental Fluid Dynamics Research* (2011), pp. 261–278.

[65] Laura Novaro Mascarello. "Analysis and development of harmless sUAS (small Unmanned Aerial Systems)." PhD thesis. Politecnico di Torino, 2018.

[66] Rainer Mautz. "Overview of current indoor positioning systems." In: *Geodezija ir kartografija* 35.1 (2009), pp. 18–22.

[67] Barnes W McCormick. *Aerodynamics, Aeronautics and Flight Mechanics*. John Wiley and Sons Ltd, 2nd edition, 1995.

[68] Matthew McCrink and James W Gregory. "Blade element momentum modeling of low-Re small UAS electric propulsion systems." In: *33rd AIAA Applied Aerodynamics Conference*. 2015, p. 3296.

[69] Daniel Mellinger, Nathan Michael, and Vijay Kumar. "Trajectory generation and control for precise aggressive maneuvers with quadrotors." In: *The International Journal of Robotics Research* 31.5 (2012), pp. 664–674.

[70] Monal Merchant and L Scott Miller. "Propeller performance measurement for low Reynolds number UAV applications." In: *44th AIAA aerospace sciences meeting and exhibit*. 2006, p. 1127.

[71] Pierre Merriaux et al. "A study of vicon system positioning performance." In: *Sensors* 17.7 (2017), p. 1591.

[72] Thomas J Mueller and James D DeLaurier. "Aerodynamics of small vehicles." In: *Annual review of fluid mechanics* 35.1 (2003), pp. 89–111.

[73] NASA. *NASA Altitude Wind Tunnel Historical Documents*. 2019. URL: https://www1.grc.nasa.gov/historic-facilities/altitude-wind-tunnel/historical-documents/ (visited on 04/09/2020).

[74] Thu Jennifer Ngo-Anh and Andrea Rossiter. "Platforms for Stress and Immune Research in Preparation for Long-Duration Space Exploration Missions." In: *Stress Challenges and Immunity in Space*. Springer, 2020, pp. 661–676.

[75] Georg Niedrist et al. "terraXcube: An emerging ecotrone to converge chamber experiments and environmental studies in alpine ecology." In: *EGU General Assembly Conference Abstracts*. Vol. 20. 2018, p. 13616.

[76] Flavio Noca et al. "Wind and Weather Facility for Testing Free-Flying Drones." In: *AIAA Aviation 2019 Forum*. 2019, p. 2861.

[77] MM O'Meara and Thomas J Mueller. "Laminar separation bubble characteristics on an airfoil at low Reynolds numbers." In: *AIAA journal* 25.8 (1987), pp. 1033–1041.

[78] NWTC Project Office. "National Wind Tunnel Complex - Final Report." Nasa Document NASA CR-198491. 1996.

[79] Delta OHM. *Specification sheet HD9408.3B sensor*. 2019. URL: https://www.deltaohm.com/en/wp-content/uploads/document/DeltaOHM-HD9408.3B-precision-barometer-datasheet-en.pdf (visited on 05/06/2020).

[80] Michael J Oliver. *Ice crystal icing engine testing in the NASA Glenn Research Center's propulsion systems laboratory: Altitude investigation*. Tech. rep. NASA, 2014.

[81] F Kevin Owen and Andrew K Owen. "Measurement and assessment of wind tunnel flow quality." In: *Progress in Aerospace Sciences* 44.5 (2008), pp. 315–348.

[82] Iris David Du Mutel de Pierrepont et al. "Model-In-the-Loop Testing of Control Systems and Path Planner Algorithms for QuadRotor UAVs." In: *2020 International Conference on Unmanned Aircraft Systems (ICUAS)*. IEEE. 2020, pp. 1809–1818.

[83] Alan Pope. *Wind-tunnel calibration techniques*. Tech. rep. ADVISORY GROUP FOR AERONAUTICAL RESEARCH and DEVELOPMENT PARIS (FRANCE), 1961.

[84] Murata Power. *50mV and 100mV Base-mounted DC Shunts*. 2019. URL: https://docs.rs-online.com/d2c9/0900766b81362844.pdf (visited on 05/04/2020).

[85] PrecisionHawk. *PrecisionHawk Explores Extreme-Weather Testing of Drones With ACE Research Centre*. 2016. URL: https://www.precisionhawk.com/blog/media/topic/precisionhawk-explores-extreme-weather-testing-of-drones-with-ace-research-centre (visited on 02/24/2016).

[86] *PrecisionHawk Explores Extreme-Weather Testing of Drones With ACE Research Centre*. https://www.precisionhawk.com/blog/media/topic/precisionhawk-explores-extreme-weather-testing-of-drones-with-ace-research-centre. Accessed: 2019-07-26.

[87] Thomas Prevot et al. "UAS traffic management (UTM) concept of operations to safely enable low altitude flight operations." In: *16th AIAA Aviation Technology, Integration, and Operations Conference*. 2016, p. 3292.

[88] Stefano Primatesta et al. "A cloud-based framework for risk-aware intelligent navigation in urban environments." In: *2017 International Conference on Unmanned Aircraft Systems (ICUAS)*. IEEE. 2017, pp. 447–455.

[89] Stefano Primatesta et al. "A Cloud-based Vehicle Collision Avoidance Strategy for Unmanned Aircraft System Traffic Management (UTM) in Urban Areas." In: *2020 IEEE 7th International Workshop on Metrology for AeroSpace (MetroAeroSpace)*. IEEE. 2020, pp. 309–313.

[90] Stefano Primatesta et al. "A Risk-based Path Planning Strategy to Compute Optimum Risk Path for Unmanned Aircraft Systems over Populated Areas." In: *2020 International Conference on Unmanned Aircraft Systems (ICUAS)*. IEEE. 2020, pp. 641–650.

[91] Stephen D Prior. *Optimizing Small Multi-Rotor Unmanned Aircraft: A Practical Design Guide*. CRC Press, 2018.

[92] S Prudden et al. "An investigation into the effects of rotor wake interference on quadrotor UAS forward flight performance." In: *AIAC18: 18th Australian International Aerospace Congress (2019): HUMS-11th Defence Science and Technology (DST) International Conference on Health and Usage Monitoring (HUMS 2019): ISSFD-27th International Symposium on Space Flight Dynamics (ISSFD)*. Engineers Australia, Royal Aeronautical Society. 2019, p. 344.

[93] William H Rae Jr. "Limits on minimum speed V/STOL wind-tunnel tests." In: *Journal of Aircraft* 4.3 (1967), pp. 249–254.

[94] SF Ramdin. "Prandtl tip loss factor assessed." MA thesis. Delft University of Technology, 2017.

131

[95] RCbenchmark. *Otus Tracker - Motion Capture for UAVs and Robots.* 2019. URL: https://www.rcbenchmark.com/pages/otus-tracker (visited on 10/14/2020).

[96] RCbenchmark. *RCbenchmark Series 1580/1585 Thrust Stand and Dynamometer.* 2019. URL: https://www.rcbenchmark.com/pages/series-1580-thrust-stand-dynamometer (visited on 05/04/2020).

[97] Marvelmind Robotics. *Marvelmind Robotics Starter Set Super-NIA-3D.* 2019. URL: https://marvelmind.com/product/starter-set-super-nia-3d/ (visited on 05/11/2020).

[98] Carl R Russell and Martin K Sekula. *Comprehensive Analysis Modeling of Small-Scale UAS Rotors.* AHS Interinational, 2017.

[99] Carl R Russell et al. *Wind tunnel and hover performance test results for multicopter UAS vehicles.* Tech. rep. NASA, 2016.

[100] Carl R Russell et al. *Wind tunnel and hover performance test results for multicopter UAS vehicles.* NASA Ames Research Center, Aeromechanics Office, 2018.

[101] Matteo Scanavino et al. "UAS Testing in Low Pressure and Temperature Conditions." In: *2020 International Conference on Unmanned Aircraft Systems.* 2020, pp. 1748–1756.

[102] Davide Scaramuzza and Zichao Zhang. "Visual-inertial odometry of aerial robots." In: *arXiv preprint arXiv:1906.03289* (2019).

[103] Tomy Sebastian. "Temperature effects on torque production and efficiency of PM motors using NdFeB magnets." In: *IEEE Transactions on Industry Applications* 31.2 (1995), pp. 353–357.

[104] John M Seddon and Simon Newman. *Basic helicopter aerodynamics.* Vol. 40. John Wiley & Sons, 2011.

[105] David A Self et al. "Physiological equivalence of normobaric and hypobaric exposures of humans to 25,000 feet (7620 m)." In: *Aviation, space, and environmental medicine* 82.2 (2011), pp. 97–103.

[106] Robert E Sheldahl and Paul C Klimas. *Aerodynamic characteristics of seven symmetrical airfoil sections through 180-degree angle of attack for use in aerodynamic analysis of vertical axis wind turbines.* Tech. rep. Sandia National Labs., Albuquerque, NM (USA), 1981.

[107] Sick. *Photoelectric sensor WLA16P.* 2019. URL: https://www.sick.com/it/it/sensori-fotoelettrici/sensori-fotoelettrici/w16/wla16p-24162100a00/p/p512654 (visited on 05/04/2020).

[108] Kasey Stevenson. "Hypoxia: An Analysis of Hypobaric Chamber Training." PhD thesis. Arizona State University, 2019.

[109] Prem S Subramanian. *Ophthalmology in Extreme Environments*. Springer, 2017.

[110] JR3 Multi-axis Load Cell Systems. *Specification sheet 30E15 F/T sensor*. 2019. URL: https://www.jr3.com/resources/specification-sheets (visited on 05/04/2020).

[111] T-Motor. *T-Motor Brushless motor MN3508*. 2020. URL: http://store-en.tmotor.com/goods.php?id=354 (visited on 05/05/2020).

[112] terraXcube. *terraXcube - Large cube datasheet*. 2019. URL: https://terraxcube.eurac.edu/about-us/#structure (visited on 04/09/2020).

[113] Bart Theys et al. "Influence of propeller configuration on propulsion system efficiency of multi-rotor Unmanned Aerial Vehicles." In: *2016 international conference on unmanned aircraft systems (ICUAS)*. IEEE. 2016, pp. 195–201.

[114] Glen Throneberry et al. "Multi-rotor wake propagation investigation for atmospheric sampling." In: *AIAA Aviation 2019 Forum*. 2019, p. 3604.

[115] Charles D Valdez. *The FAA Altitude Chamber Training Flight Profile: A Survey of Altitude Reactions 1965-1989*. Tech. rep. FEDERAL AVIATION ADMINISTRATION WASHINGTON DC OFFICE OF AVIATION MEDICINE, 1990.

[116] John Michael Velarde et al. *Experimental Characterization of UAS Flow Fields Through Hotwire Anemometry and PIV*. 2018, p. 4121.

[117] Patricia Ventura Diaz and Steven Yoon. "High-fidelity computational aerodynamics of multi-rotor unmanned aerial vehicles." In: *2018 AIAA Aerospace Sciences Meeting*. 2018, p. 1266.

[118] David Wall. "Optimum propeller design for electric uavs." PhD thesis. 2012.

[119] Xin Wang et al. "Effects of altitude on the thermal efficiency of a heavy-duty diesel engine." In: *Energy* 59 (2013), pp. 543–548.

[120] Maurice Weinberg and John Wyzykowski. *Development and testing of a commercial turbofan engine for high altitude UAV applications*. Tech. rep. SAE Technical Paper, 2001.

[121] Caleb White et al. "The soaring potential of a micro air vehicle in an urban environment." In: *International Journal of Micro Air Vehicles* 4.1 (2012), pp. 1–13.

[122] Graham Wild, John Murray, and Glenn Baxter. "Exploring civil drone accidents and incidents to help prevent potential air disasters." In: *Aerospace* 3.3 (2016), p. 22.

[123] Marius Wilhelm et al. *Test Facility for Research on Advanced Green Propellants under High-Altitude Conditions*. Tech. rep. German Aerospace Center, 2018.

[124] Justin Winslow et al. "Basic Understanding of Airfoil Characteristics at Low Reynolds Numbers (10 4–10 5)." In: *Journal of Aircraft* 55.3 (2018), pp. 1050–1061.

[125] Andrew D Woodrow, James T Webb, and Grady S Wier. "Recollection of hypoxia symptoms between training events." In: *Aviation, space, and environmental medicine* 82.12 (2011), pp. 1143–1147.

[126] Seokkwan Yoon, Henry C Lee, and Thomas H Pulliam. *Computational study of flow interactions in coaxial rotors*. Tech. rep. NASA Ames Research Center, 2016.

[127] Geoff Kibble Zach Barbeau Jordan Feight and Jamey Jacob. *Quadrotor Flow Field Visualization*. URL: https://doi.org/10.1103/APS.DFD.2015.GFM.V0098 (visited on 04/30/2020).

[128] Wenwu Zhou et al. "An experimental investigation on rotor-to-rotor interactions of small UAV propellers." In: *35th AIAA applied aerodynamics conference*. 2017, p. 3744.

[129] CH Zimmerman. *Preliminary Tests in the NACA Free-Spinning Tunnel*. Tech. rep. Langley Technical Report 557, 1936.

This Ph.D. thesis has been typeset by means of the T_EX-system facilities. The typesetting engine was LuaLaT_EX. The document class was `toptesi`, by Claudio Beccari, with option `tipotesi` `=scudo`. This class is available in every up-to-date and complete T_EX-system installation.